University of Cyprus

DEPARTMENT OF MECHANICAL AND MANUFACTURING ENGINEERING

Fabrication and Optimization of n-type half Heusler materials via Mechanical Alloying

DOCTOR OF PHILOSOPHY DISSERTATION

GEORGIOS MESARITIS

2022

University of Cyprus

DEPARTMENT OF MECHANICAL AND MANUFACTURING ENGINEERING

Fabrication and Optimization of n-type half Heusler materials via Mechanical Alloying

GEORGIOS MESARITIS

A Dissertation Submitted to the University of Cyprus in Partial Fulfillment of the Requirements for the Degree of Doctor of Philosophy

December 2022

VALIDATION PAGE

Doctoral Candidate: Georgios Mesaritis

Doctoral Thesis Title: Fabrication and Optimization of n-type half Heusler materials via Mechanical Alloying

The present Doctoral Dissertation was submitted in partial fulfillment of the requirements for the Degree of Doctor of Philosophy at the ***Department of Mechanical and manufacturing engineering*** *and was approved on the [30/9/2022] by the members of the* ***Examination Committee****.*

Examination Committee:

Research Supervisor: Professor Theodora Kyratsi……..

Committee Member: Professor Ioannis Giapintzakis……...

Committee Member: Professor Theodora Krasia…….

Committee Member: Professor Neophytos Neophytou……

Committee Member: Professor Anastasios Tasiopoulos……..

DECLARATION OF DOCTORAL CANDIDATE

The present doctoral dissertation was submitted in partial fulfillment of the requirements for the degree of Doctor of Philosophy of the University of Cyprus. It is a product of original work of my own, unless otherwise mentioned through references, notes, or any other statements.

Georgios Mesaritis

……..

Περίληψη

Η απαίτηση για αυξανόμενες ενεργειακές ανάγκες καθώς επίσης και ο περιορισμός των διαθέσιμων πόρων έχει οδηγήσει την ερευνητική κοινότητα στην αναζήτηση εναλλακτικών τεχνολογιών παραγωγής ενέργειας, με χαρακτηριστικά όπως χρήση ανανεώσιμων πηγών, αυξημένη απόδοση, χαμηλό κόστος. Προκειμένου να αυξηθεί η ενεργειακή απόδοση, η ανάκτηση της αναπόφευκτης διαφεύγουσας ενέργειας ως θερμότητα μέσω θερμοηλεκτρικών γεννητριών τυγχάνει ιδιαίτερης προσοχής τόσο σε ερευνητικό όσο και βιομηχανικό επίπεδο. Οι θερμοηλεκτρικές γεννήτριες δύναται να χρησιμοποιηθούν στη μετατροπή θερμότητας σε ηλεκτρική ενέργεια με εφαρμογές σε εύρος ισχύος όπως ενεργοβόρα βιομηχανία (π.χ. τσιμεντοβιομηχανία, μεταλλοβιομηχανία) ή μέσα μεταφοράς (π.χ. αυτοκίνητα, πλοία) ή ακόμα και στη τροφοδοσία έξυπνων συσκευών μικρής ισχύος αξιοποιώντας τη θερμότητα σώματος.

Μέχρι σήμερα, έχουν αναπτυχθεί διάφοροι τύποι θερμοηλεκτρικών υλικών, όπως οι εμπορικά διαθέσιμες ενώσεις βισμούθιου τελλουρίου για εφαρμογές περί της θερμοκρασίας δωματίου, τα skutterudites, ενώσεις half Heusler, ενώσεις πυριτίου ή μολύβδου-τελλουρίου για μεσαίες θερμοκρασίες και τις ενώσεις γερμανίου-πυριτίου (SiGe) για υψηλές θερμοκρασίες. Οι κατηγορίες που αναφέρθηκαν παρουσιάζουν υψηλή θερμοηλεκτρική απόδοση, όμως, προκειμένου να ικανοποιούνται και άλλες απαιτήσεις τα θερμοηλεκτρικά υλικά θα πρέπει να περιέχουν πρώτες ύλες φιλικές προς το περιβάλλον και τον άνθρωπο και βρίσκονται σε αφθονία στην φύση.

Μεταξύ των διαφόρων κατηγοριών υλικών, τα υλικά που σχηματίζουν ενώσεις Heusler βρίσκονται σε μεγάλη αφθονία στη φύση και αποτελούν ένα σύστημα που έχει ελκύσει ιδιαίτερο ενδιαφέρον. Οι ενώσεις Half Heusler μπορούν να χρησιμοποιηθούν από μεσαίο έως υψηλό θερμοκρασιακό εύρος, ενώ η υψηλή θερμική τους σταθερότητα και μηχανική αξιοπιστία τα καθιστά ισχυρούς υποψήφιους για θερμοηλεκτρικές γεννήτριες (TEGs). Τόσο το n-τύπου υλικό MNiSn όσο και το p-τύπου υλικό MCoSb, (όπου M=Ti, Zr και Hf), έχουν μελετηθεί εκτενώς τα τελευταία χρόνια ενώ έχουν προσδιοριστεί τιμές απόδοσης (ZT) > 1. Η υψηλότερη τιμή απόδοσης για τα n-τύπου half Heusler υλικά μέχρι σήμερα είναι 1.5 στους 700K για το ντοπαρισμένο με Sb- $Hf_{0.25}Zr_{0.25}Ti_{0.5}NiSn$ υλικό, ενώ για τα p-τύπου είναι 1.5 στους 973K. Ωστόσο, η θερμοηλεκτρική τους απόδοση περιορίζεται ουσιαστικά από τη υψηλή θερμική τους αγωγιμότητα. Συνεπώς, η ερευνητική κοινότητα εστιάζει σε διάφορες

προσεγγίσεις για τη μείωσή της θερμικής αγωγιμότητας, όπως για παράδειγμα με κραματοποίηση (alloying) ή δημιουργία νανοδομών (nanostructures) για την ενίσχυση της σκέδασης των φωνονίων.

Στην παρούσα διδακτορική διατριβή, αναπτύχθηκε για πρώτη φορά μεθοδολογία μηχανικής κραμμάτωσης για τη σύνθεση των half Heusler υλικών με διπλό στόχο: (α) τη σύνθεση των υλικών και (β) ταυτόχρονηδημιουργία ιεραρχικών δομικών χαρακτηριστικών (από ατομικό σε μικροσκοπικό επίπεδο) για την ενίσχυση της σκέδασης φωνονίων και, συνεπώς, τη μείωση της θερμικής αγωγιμότητας. Αναπτύσσοντας αυτή τη μεθοδολογία ήταν εφικτό να εφαρμοστούν ταυτόχρονα διαφορετικές στρατηγικές βελτιστοποίησης συμπεριλαμβανομένων την ισοηλεκτρονική αντικατάσταση καθώς επίσης και τη δημιουργία νανο- και μικρο-δομών κατά το στάδιο της σύνθεσης χωρίς να απαιτούνται περαιτέρω διεργασίες.
Πιο συγκεκριμένα, μελετήθηκαν εκτενώς στοιχειομετρίες n-τύπου υλικών $Ti_{1-x}Zr_xNiSn$, $Ti_{1-y}Hf_yNiSn$ και το (Ti,Zr,Hf)NiSn. Διαφορετικές τεχνικές χαρακτηρισμού εφαρμόστηκαν συμπληρωματικά και επιβεβαίωσαν τη δημιουργία ιεραρχικών δομικών χαρακτηριστικών ενώ μη τη μελέτη των θερμοηλεκτρικών ιδιοτήτων προσδιορίστηκε η μέγιστη θερμοηλεκτρική απόδοση (figure of merit) του 0.71 στους 773K για τη στοιχειομετρία $Ti_{0.4}Zr_{0.6}NiSn_{0.985}Sb_{0.015}$. Επιπρόσθετα, μελετήθηκε η επίδραση της ανόπτησης (annealing) στη μικροδομή και στις θερμοηλεκτρικές ιδιότητες για την περαιτέρω κατανόηση της προτεινόμενης διαδικασίας σύνθεσης. Τέλος, μελετήθηκε η επίδραση της ενσωμάτωσης Hf στη σειρά στερεών διαλυμάτων (Ti,Zr,Hf)NiSn. το οποίο επηρέασε σημαντικά τη θερμική αγωγιμότητα λόγω της μεγαλύτερης διακύμανσης μαζών που είναι παρούσα στο κρυσταλλικό πλέγμα.

Abstract

The demand for increasing energy needs as well as the limitation of available resources has led the research community to search for alternative energy production technologies with characteristics such as the use of renewable sources, increased efficiency, low cost. In order to increase energy efficiency, the recovery of the inevitable waste energy (heat) through thermoelectric generators receives special attention at both, research and industrial level. The thermoelectric generators can be used to convert heat into electricity and the applications may include energy-intensive industry (e.g. cement industry, metal industry) or transportation (e.g. cars, ships) or even low-power smart devices utilizing human body heat.

Up to date, several types of thermoelectric materials have been developed, such as (a) commercially available bismuth tellurium compounds for room temperature, (b) skutterudites, half Heusler compounds, silicon or lead-tellurium compounds for medium temperature, and (c) germanium-silicon (SiGe) compounds for high temperature applications. These materials presenthigh thermoelectric efficiency, however, they need to meet also other requirements such as contain environmental and human friendly raw materials that are also abundant in nature.

Among the various categories of thermoelectric materials, Heusler compounds consist of elements that are abundance in nature and has attracted particular interest. The half Heusler materials can be used from a medium to high temperature range, while their high thermal stability and mechanical reliability make them strong candidates for the development of thermoelectric generators (TEGs). Both, n-type MNiSn and p-type MCoSb (where M=Ti, Zr and Hf), have been extensively studied with figure of merit values (ZT)>1. Up to date, the highest figure of merit for n- type half Heusler materials is 1.5 at 700K for the Sb- doped $Hf_{0.25}Zr_{0.25}Ti_{0.5}NiSn$, while for the p-type is 1.5 at 973K. Overall, further increase in the thermoelectric performance is limited by their high thermal conductivity, therefore, research community focuses on applying various approaches such as alloying or creating nanostructures to increase phonon scattering.

In this PhD thesis, the methodology for the synthesis of n-type half Heusler materials via mechanical alloying was developed for first time aiming both: (a) the synthesis of the materials and (b) the in-situ creation of hierarchical structural features (from atomic to microscopic level) to enhance scattering phonons and, therefore, reduce of thermal conductivity. The development

of this methodology led to the application of different optimization strategies including isoelectronic substitution as well as the creation of nano- and micro-structural features right from the synthesis stage.

More specifically, n-type $Ti_{1-x}Zr_xNiSn$, $Ti_{1-y}Hf_yNiSn$ and $(Ti_{0.4}Zr_{0.6})_{1-z}Hf_zNiSn$ stoichiometries were extensively studied. By applying complementary characterization techniques, the developed hierarchical structural characteristics were confirmed while the maximum thermoelectric efficiency (figure of merit) of 0.71 at 773K was achieved for the $Ti_{0.4}Zr_{0.6}NiSn_{0.985}Sb_{0.015}$ member. In addition, the effect of annealing on the microstructure and the thermoelectric properties was studied to better understand this type of synthesis. Finally, the effect of Hf incorporation in the (Ti,Zr,Hf)NiSn solid solution series was studied, and the significant effect on the thermal conductivity due to the larger mass variation in the lattice is discussed.

Acknowledgments

Firstly, I would like to express my sincere gratitude to my advisor Prof.Theodora Kyratsi for the continuous support of my Ph.D study and related research, for her patience, motivation, and immense knowledge. Her guidance helped me in all the time of research and writing of this thesis. I could not have imagined having a better advisor and mentor for my Ph.D study.

Besides my advisor, I would like to thank the rest of my thesis committee: Prof. Ioannis Giapintzakis and Prof. Theodora Krasia, for their insightful comments and encouragement, but also for the hard question which incented me to widen my research from various perspectives. Also, I would like to thank the Prof. Anastasios Tasiopoulos and Prof. Neophytos Neophytou for accepting the invitation.

My sincere thanks also go to Dr. Elli Symeou and Mr. Kypros Stylianou who both trained me and giving to me access to the laboratory and research facilities. Furthermore, I am grateful to Dr. Andreas Delimitis and Prof. Euripidis Hatzikraniotis for their support to my research with TEM and Simulation studies.

Moreover, I would like to express my sincere gratitude to the M-Era.Net project "MarTEnergy", funded by the Cyprus Research Promotion Foundation (P2P/KOINA/MERA.NET/ 0317/04) and the Ministry of Science Technology and Space of Israel for supporting the half-Heusler research.

I thank my fellow labmates in for the stimulating discussions, for the sleepless nights we were working together, and for all the fun we have had in the last four years. Last but not the least, I would like to thank my family: my parents and my brother Andreas for supporting me spiritually throughout writing this thesis and my life in general.

List of Publications

1. G.Mesaritis and Th.Kyratsi "Hf incorporation in (Ti,Zr)NiSn half Heusler solid solutions via Mechanical Alloying" Journal of Energies 15(21),7885(2022)

2. G.Mesaritis, I.Ioannou, A.Delimitis, E.Hatzikraniotis, Y.Gelbstein and Th.Kyratsi "n-type (Zr,Ti)NiSn half Heusler materials via mechanical alloying: Structure, Sb-doping and thermoelectric properties" Journal of Physics and Chemistry of Solids (2022):110735

3. G.Mesaritis,E.Symeou,A.Delimitis,M.Constantinou,G.Constantinides,M.Jeagle,K. Tarantik and Th.Kyratsi "Synthesis, characterization and thermoelectric performance of Mg2(Si,Sn,Ge) materials using Si-kerf waste from photovoltaic technology" Journal of alloys and compounds 826(2020):153933

4. G.Mesaritis,E.Symeou,A.Delimitis,S.Oikonomidis,M.Jaegle,K.Tarantik,Ch.Nicola ou and Th.Kyratsi "Recycling Si-kerf from photovoltaics: A very promising route to thermoelectrics" Journal of alloys and compounds 775 (2019):1035-1043

List of Conferences

1. **Oral Presentation:** title: "Synthesis, Characterization and thermoelectric properties of n-type half Heusler materials via Mechanical Alloying", George Mesaritis and Theodora Kyratsi,18th European Conference on Thermoelectrics (ECT2022) 14-16 September 2022, Barcelona, Spain

2. **Oral Presentation:** title: "Synthesis and Properties of n-type $(Zr,Ti)_{1-x}Hf_xNiSn$ Half Heusler alloys via Mechanical Alloying**",** George Mesaritis, Andreas DelimitisYaniv Gelbstein and Theodora Kyratsi, XXXV Panhellenic Conference on Solid State Physics & Materials Science 26-29 September 2021,Athens,Greece

3. **Oral Presentation:** title: "Novel synthesis of n-type (Zr,Ti)NiSn Half Heusler alloys via Mechanical Alloying", George Mesaritis,Yaniv Gelbstein and Theodora Kyratsi, European Congress and Exhibition on Advanced Materials and Processes (Euromat) 13-17 September 2021, Virtual

4. **Oral Presentation**: title: "Fabrication of (Ti,Zr)NiSn Half Heusler via Mechanical Alloying", George Mesaritis, Yaniv Gelbstein and Theodora Kyratsi, Virtual Conference on Thermoelectricity (VCT) 20-22 July 2021

5. **Oral Presentation:** title: Thermal Analysis of thermoelectric materials Mg2(Si,Sn,Ge) using Laser Flash Analysis, George Mesaritis and Theodora Kyratsi, "Short -cycle Training course on Thermal Analysis in Materials Science" 3-6 September 2019 , Rome, Italy

6. **Poster Presentation**: title: "Fabrication of half Heusler (Ti,Zr,Hf)NiSn via Mechanical Alloying, George Mesaritis, Gill Breuer, Yaniv Gelbstein and Theodora Kyratsi, 17th European Conference on Thermoelectrics (ECT2019) 23-25 September 2019, Limassol, Cyprus

7. **Oral Presentation:** title: Fabrication of TiNiSn and solid solutions by Mechanical Alloying, George Mesaritis, Gill Breuer,Yaniv Gelbstein and Theodora Kyratsi, Course 207: Advances in Thermoelectricity Foundational Issues,Materials and Nanotechnology,15-20 July 2019, Varena, Italy

8. **Poster Presentation**: title: High thermoelectric figure of merit of $Mg_2Si_{0.55}Sn_{0.4}Ge_{0.05}$ materials doped with Bi using Si kerf from photovoltaics as starting material", George Mesaritis, Elli Symeou, Andreas Delimitis, Nikos Vlachos, Christiana Nicolaou and Theodora Kyratsi, Panhellenic Conference on Solid State Physics & Materials Science, 19-23 September 2018, Nicosia, Cyprus

Contents

List of Figures

List of Tables

Chapter 1

1. Introduction

The first chapter introduces thermoelectric devices and phenomena. Particularly, the thermoelectric effects, the desirable thermoelectric properties as well as applications of thermoelectric devices are discussed.

1.1 Thermoelectric devices

The need to reduce global warming and the usage of fossil fuels, as well as the increased worldwide energy demand, led the researchers to discover alternative energy resources. Thermoelectric technology (TE) has been studied for more than two centuries and is based on the energy conversion of waste heat into electricity[1–3]. The good reliability and scalability combined with the fact that no moving parts exist in these devices has inspired the worldwide interest to used them for power generation and cooling applications. The TE devices, consist two parallel pieces of material, one p-type and one n-type (figure 1). Their flat surfaces are electrically connected to a metal conductor to convert the lost heat directly into electricity. The thermoelectric devices, as it mentioned above, can be used for power generation generators or for cooling applications. The p-type materials conduct the heat in the same direction as electric current while the n-type from the opposite direction (see figure 1) as a result the upper part is heated and the lower one is cooled. Considering that no moving parts exist, the advantages of these devices are the reduced maintenance cost and the absent of the noise due to the silent operation. The principles and the thermoelectric phenomena were observed by Seebeck in 1821, while the key parameter called the performance of thermoelectric materials (ZT) was given by AltenKirch in 1911. Nevertheless, it took several decades of research to develop the first functional device in 1950 by Alessandro Volt [1–3]. The efficiency of these devices is described via a dimensionless quantity called ‘figure of merit’ ZT. The figure of merit it has been used as a key parameter to weigh the differences between materials at different temperatures. The discovery of new compounds and the optimization of them in order to find the optimum figure of merit is significant for the community.

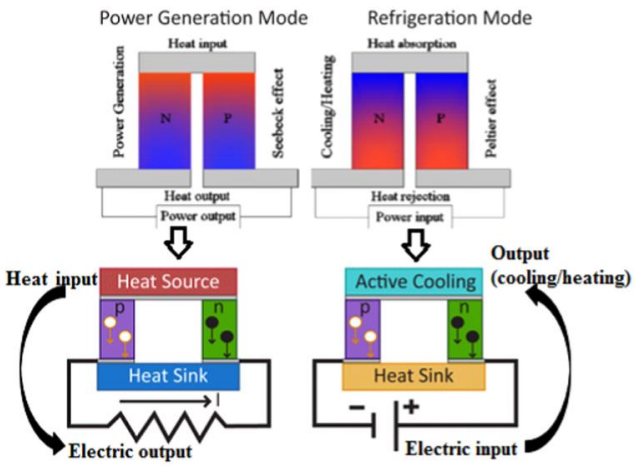

Figure 1: Thermoelectric devices for power generation/refrigeneration. [1]

1.2 Thermoelectric Phenomena

1.2.1 Seebeck Effect

The Seebeck coefficient indicates the ability of the material to create a potential difference when a temperature difference is applied. Figure 2 displays an open circuit where branches a and b are from different conducting materials. A and B are contacts with the different temperatures T1>T2, this can result in a creation of an electric force E_{ab} at the ends Γ and Δ. This phenomenon is called the Seebeck effect while the proportional constant Seebeck coefficient is given by eq.1[4,5]:

$$S_{\alpha\beta} = \frac{dE_{\alpha\beta}}{dT} \quad (1)$$

Where the Seebeck coefficient express the sum of the absolute Seebeck coefficient of the individual materials at low temperatures as given by the linear eq.2

$$S_{\alpha\beta} = S_{\alpha} + S_{\beta} \quad (2)$$

Thus,the electric force can be expressed by eq.3:

$$E_{\alpha\beta} = S_{\alpha\beta}(T_1 - T_2) \quad (3)$$

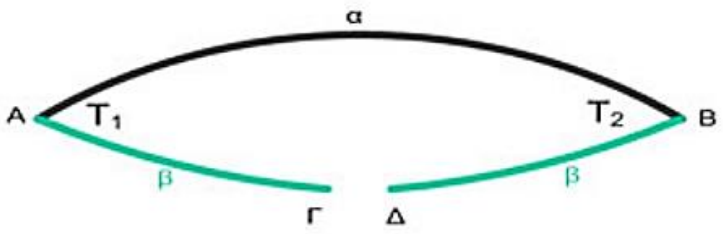

Figure 2: Simple diagram of thermocouple [4,5]

The SI units of the Seebeck coefficient is more often given in μV/K.The Seebeck can be also be given by the Mott Formula from the Boltzman equation using the single parabolic band model:

$$S = \frac{\pi^2 k^2{}_B}{3e} T \left(\frac{d\left[\ln\left(\sigma(E)\right)\right]}{dE} \right)_{E=E_F} \quad (4)$$

where σ(E) is the electrical conductivity that is a function of Energy E at the Fermi level E_F , e the electron charge and k_B the Boltzman constant. The electrical conductivity is given from the equation 5 and it depends to the carrier concentration n and the mobily μ of the carriers.

$$\sigma = ne\mu \quad (5)$$

The incorporation of eq.5 to the eq.4 leads to:

$$S = \frac{\pi^2 k^2{}_B}{3e} T \left(\frac{dn(E)}{ndE} + \frac{dn(E)}{\mu dE} \right)_{E=E_F} \quad (6)$$

The modification of carriers concentration can increase the Seebeck coefficient. Insulators have low electrical conductivity and low carriers but high Seebeck. In contrast metals have high

carriers concentration ($n \geq 10^{22} cm^{-3}$) and ($\sigma \geq 10^{6} S/m$). The semiconductors and especially the degererate or the highly doped semiconductors with high carriers concentration can react like a metal and the Seebeck coefficient can be given by eq.7:

$$S = \frac{8\pi^2 {k^2}_B}{3eh^2} m^* T \left(\frac{\pi}{3n}\right)^{\frac{2}{3}} \quad (7)$$

where n is the carrier concentration, m^* the effective mass and h the Planck constant. Seebeck coefficient for doped semiconductors has negative sign for n-type materials and positive for p-type the intrinsic semiconductors have both carriers and as a result small values of Seebeck.

1.2.2 Peltier Effect

The Peltier effect is similar to Seebeck. Essentially is the reverse phenomenon with the difference that in the ends of C and D a source of electro-exciting force is inserted (see Fig 3). Then a current I, is created and leads to dissipate heat Q from contact A while contact B is absorbs heat. The contact A heats up and B cools down this phenomenon is called the Peltier effect. The Peltier Coefficient is given[4]:

$$\Pi_{\alpha\beta} = \frac{Q}{I} \quad (8)$$

where Παβ:

$$\Pi_{\alpha\beta} = \Pi_{\alpha} + \Pi_{\beta} \quad (9)$$

The SI units for Peltier is V or W/A.

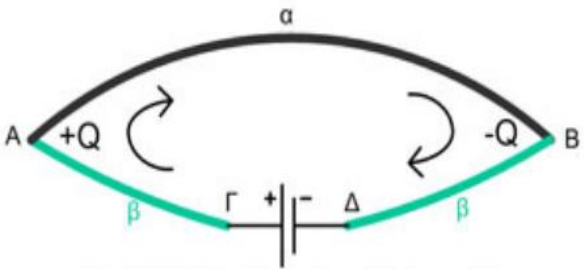

Figure 3: Peltier Diagram [4,5]

1.2.3 Thomson effect

Finally, another thermoelectric phenomenon is the Thomson effect. This phenomenon is describing the absorption or the production of heat when an electric current passes through a homogeneous conductive material with a constant temperature gradient. Thomson effect can be expressed as[4]:

$$Q = \frac{\beta}{\Delta T} \quad (10)$$

where β is the Thompson coefficient with units V/K.
Thomson effect is mainly used for accurate calculations since it has minor impact in the thermoelectric devices.

1.3 Thermoelectric materials and Figure of merit

1.3.1 Figure of merit

The efficiency of thermoelectric devices is described via a dimensionless quantity called 'figure of merit' ZT. The figure of merit it has been used as a key parameter to weigh the differences between materials at different temperatures. It depends on three physical properties, thermal conductivity (κ), electrical conductivity (σ) and Seebeck Coefficient (S). Their relationship is expressed by eq. 11. Furthermore, κ can be defined by the lattice (κ_{lat}) and electronic contributions(κ_{el}) as eq. 12 shows[6].

$$zT = \frac{S^2\sigma}{\kappa}T \quad (11)$$

$$\kappa = \kappa_{lat} + \kappa_{el} \ (12)$$

where, the quantity $\mathbf{S^2\sigma}$ is clarified as the power factor (PF) and T is the temperature. The interdependence of the above properties is the main problem to achieve high ZT values. In order to obtain high ZT values PF must be large while the thermal conductivity κ must be minimized. Hence, that inspires the community to develop strategies to enhance the materials average ZT[6].

According to A.F.Ioffe studies on semiconductors, the most encouraging materials for thermoelectric conversion is the heavily doped semiconductors[6]. Figure 4 presents the Carrier concentration diagram vs Power factor for heavily doped TE materials. As shown by Fig. 4 when the carrier's concentrations (n) increases then the power factor is maximized. Also, it shows that Heavily doped semiconductors seem to be the most promising TE materials.

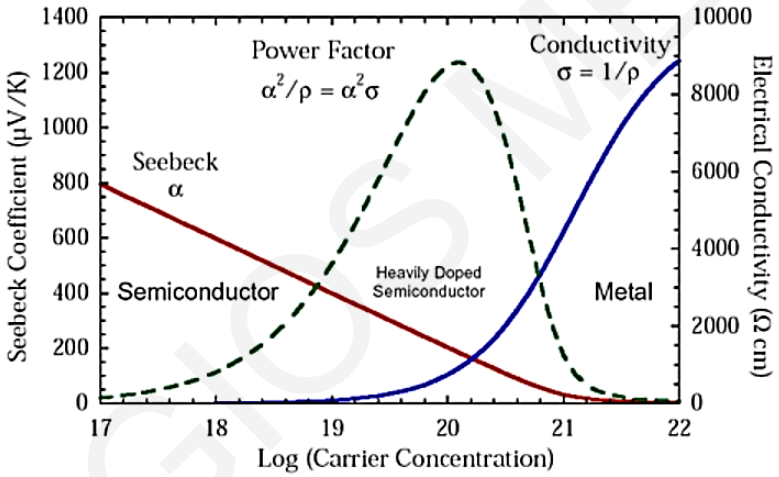

Figure 4: Carriers concentration diagram vs Power factor [6]

1.3.2 Electrical conductivity

Electrical conductivity (σ) is a measurement of how easily a material allows electric current to flow through it. The SI units of electrical conductivity is siemens per meter (S/m). Electrical conductivity is depends on the carrier concentration (n) and the carrier mobility (μ) (see eq.5) when the carrier concentration and mobility increases the electrical conductivity is increased as well. Although the increase of effective mass m^* can decrease the mobility eq.13.

$$\frac{1}{\mu} = \frac{e\tau}{m^*} \quad (13)$$

where e is the electric charge, τ is the mean scattering time between collisions for the carriers. The electrical conductivity for semiconductors materials includes contributions from electrons and holes.

$$\sigma = ne\mu_e + pe\mu_p \quad (14)$$

where μ_e and μ_p mobilities of the electrons and holes respectively.

1.3.3 Thermal conductivity

Electrical carriers (electrons or holes), phonons, electromagnetic waves and other excitations are carrying heat energy in solids. Most of the heat in metals is transported by electrical carries while in insulators phonons are the main heat transporter. Thermal conductivity is a quantity which is related to heat transport through a material and for semiconductors can be given by eq.12 [7]:

$$\kappa = \kappa_e + \kappa_{lat} \quad (12)$$

From eq 12 is obvious that both electrons and phonons contribute to the heat transport. Thermal conductivity is mainly depended on the materials properties. The lattice defects and dislocations, carrier concentration, the grain size as well as the interaction of carries with phonons are some parameters which affect the thermal conductivity.

The electronic thermal conductivity κ_e is given from the Wiedemann Frantz law[7]:

$$\kappa_e = L\sigma T \quad (15)$$

where L: Lorentz number: Temperature and σ: electrical conductivity.

For metals the Lorentz number is taken constant and equal to 2.44 x10^{-8}W/mK (degenerate limit). However, the thermoelectrics which are heavily doped semiconductors have an L near to degenerate limit [8]. The optimized materials have charge carriers concentrations between the two regions (non-degenerate and degenerate) as a consequence errors up to 40%.The single parabolic band model gives a correction on the measured thermopower [8].
Both, Lorentz and Seebeck are functions of the reduced chemical potential (n) and the carrier scattering factor [8]:

$$S = \pm\frac{k_B}{e}\left[\frac{2F_1(n)}{F_0(n)} - n\right] \quad (16)$$

$$L = \left(\frac{k_B}{e}\right)^2\left[\frac{3F_0(n)F_2(n) - 4{F_1}^2(n)}{{F^2}_0(n)}\right] \quad (17)$$

$$F_i(n) = \int_0^\infty \frac{x^i dx}{1+\exp(x-n)} \quad (18)$$

The $F_i(n)$ represents the Fermi Dirac integral and the reduced Fermi Energy E_F/k_BT. The equations 16-18 are solved numerically.

The lattice thermal conductivity κ_{lat} is affected from phonons. Phonons are categorized in two types acoustic phonons (low frequencies and atoms moving in the same phase) and optical phonons (with high frequencies and the atoms moving to opposite phases)[7]. Additionally, optical phonons have low group velocity and for that reason they do not have a significant impact to lattice thermal conductivity[7]. The interactions among optical and acoustic branches influence the thermal transport. The lattice thermal conductivity is expressed from the equation 19:

$$\kappa_{lat} = \frac{1}{3}C_v v_s \lambda_{ph} \quad (19)$$

Where, C_v is the heat capacity at constant volume, v_s is the sound velocity λ_{ph} is the phonons mean free path[7].

As is clarified from the eq.19 the mean free path of phonons has a crucial role to the lattice thermal conductivity. This is due to the dependence of the mean free path on the crystal structure, the incite defects and the grain boundaries[7].

1.4 TEG Efficiency and Applications

The TE efficiency of a device is evaluated from the thermoelectric figure of merit ZT of the individual materials. The thermoelectric efficiency of η_{max} of a TEG is given from eq.20 [5]:

$$\eta_{max} = \frac{T_H - T_C}{T_H} \frac{\sqrt{1 + ZT_{ave}}}{\sqrt{1 + ZT_{ave}} + \frac{T_C}{T_H}} \frac{-1}{} \quad (20)$$

where T_H and T_C are the temperature at hot and cold side respectively and ZT_{ave} is the average ZT.

In figure 5 is illustrated the necessary figure of merit at T_C=300K to achieve high efficiencies in TEG [5]. The fabrication of materials with superior figure of merits at reasonable cost and compositions that are non-toxic and environmentally friendly will revolutionize the power generation industry in the near future.

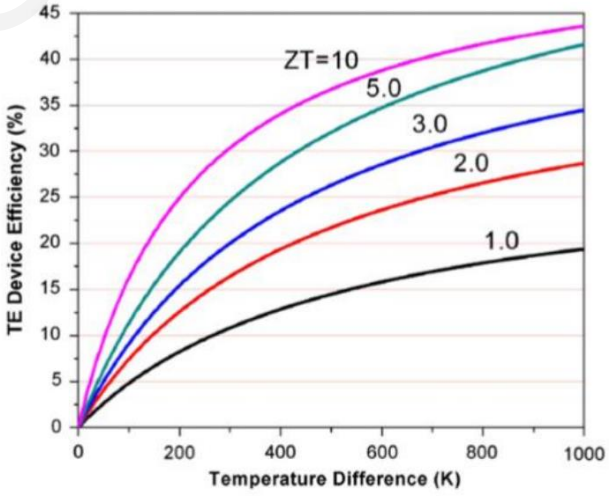

Figure 5: Figure of merit and TE efficiency at T_c=300K.[5]

TEGs are divided into stationary and mobile ones. In stationary TEGs the hot-side Temperature is expected to be stable and some parameters that may affect the performance such as the overall weight and the sensitive to vibrations are typically relaxed. On the other hand, in applications such as the harvesting exhaust waste heat in vehicles include extra challenges which are the temperature fluctuations of the hot source and mechanical vibrations who affect the stability and the integrity of the device[2,3]. Several economic factors such as the long-term uncertainty of fossil fuels hold back the development of TE devices in commercial scale. For instance, the recovery of waste heat in automobiles can be used to as electrical power to extend the vehicle mileage. This energy saving must exceed the TEG cost. The stationary TEGs which involved large units are installed in industrial facilities. Until now the number of available commercial TEGs is very small and they use first-generation materials such as alloys of bismuth and lead telluride. The articulated lorries which run over 100 000 miles per year at a fuel economy of approximately 6 miles per gallon, are candidates to involve them in TEG applications. In case of 5% minimum energy saving from TEG can approximately save \$6000 yr^{-1} and \$90000 in vehicle lifetime 10-15 years[2,3].

The field of TEs has remarkable advances in new materials but there is a main obstacle to the development of devices only very few researchers have the facilities and the expertise to fabricate TE power-generating devices.

Some applications of TEGs in industry are presented in figure 6. The radioisotope thermoelectric generator (RTG) introduced in 1961 was one of the first applications of TEGs. Radioactive atoms were releasing heat and some amount was converted to electricity. In the medical sector, many companies have manufactured nuclear powered pacemakers in 2004 but after the lithium batteries the market of nuclear batteries stopped. In our time, thermoelectric generators are designed to supply energy in autonomous sensors installed in remote locations for example in difficult access locations which solar and wind energy are not available and the heat is supplied via catalytic burners[2,3].

Furthermore, TEGs can also find an application in human body which the heat is stable and natural, thermoelectric watches are available in market. To conclude as it was previously described, TE generators can be used in transport like vehicles industry. Maritime industry is widening and is contribute further to greenhouse gas emissions which leads to the climate change. Kristiansen et al, state that the development of TE system in marine time aiming to recover the waste heat is can be feasible. Bearing in mind, the ships engines are releasing heat

in order to heat the heavy fuel oil ,cabin areas and to generate fresh water. These activities reduced the temperature of waste heat to an optimum level to use the TEG[2,3].

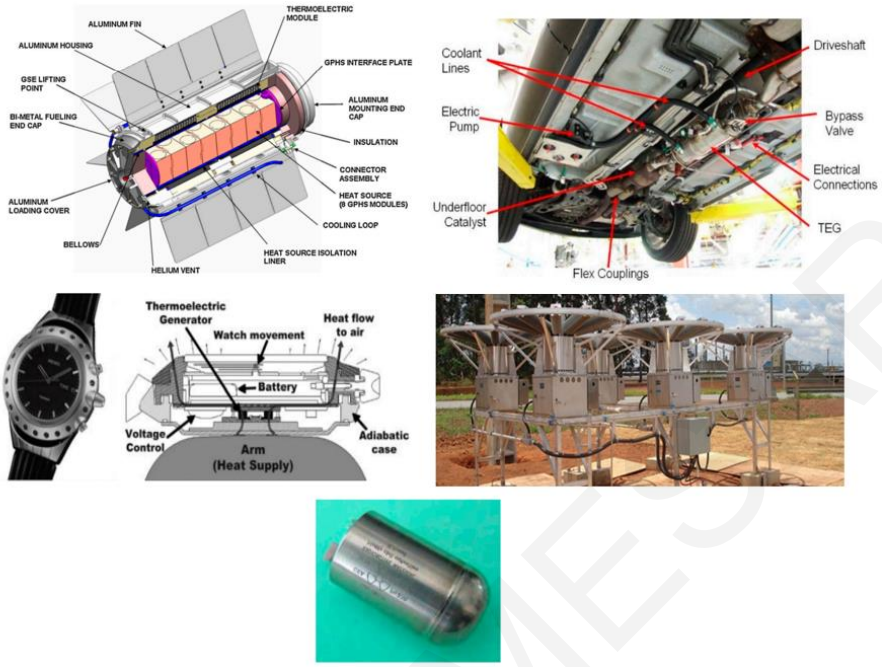

Figure 6: TEGs applications in industry.[2,3]

Chapter 2

2.Thermoelectric materials

In Chapter two the summary of the relevant literature is presented. The physical properties and structure of full and half Heusler materials as well as the synthesis method of HH are presented. Moreover, the literature review includes the summary of previews studies.

2.1 TE Generations

The dimensionless figure of merit can be expressed as a function of years research progress and Temperature as shown in Fig 7. Based on the years, ZT can be separated in three generations of TE materials. The first generation of TE materials exhibit ZT below 1, after several years of experimental research the figure of merit was doubled, and it is in the range of 1.3-1.7 and the materials which display these values are called second generation[9–12]. This is mainly to the uses of nanoscale precipitates and compositional inhomogeneities which supress the lattice thermal conductivity.

Moreover,if enhancing approaches such as: (a) the enhancement of Seebeck coefficient via band convergence, (b) the retention of the carrier mobility via band energy offset minimization between matrix and precipitate as well as the (c) reduction of lattice thermal conductivity through all length-scale phonon scattering can combined together in a single material then we can describe the third generation of thermoelectric materials with figure of merit ranging from 1.8-2.2[5,9].

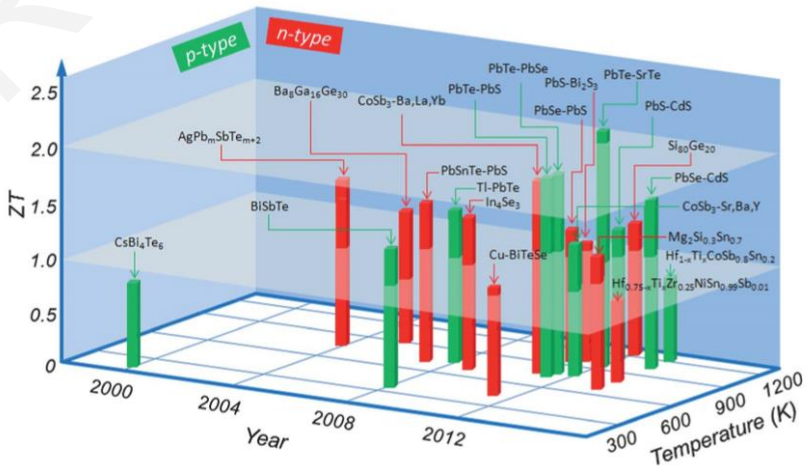

Figure 7: Figure of merit based on years, temperature and category of materials.[5,9]

2.2 Optimization Strategies

For what is discussed above impressive thermoelectric performances have been achieved due to the enhancing approaches. In this section the optimization strategies for the bulk thermoelectrics are discussed. The major strategies are nanostructuring, all-scale hierarchical architecturing, matrix/precipitate band alignment and intra-matrix electronic structure engineering.

2.2.1 Reduction of Thermal conductivity

2.2.1.1 Alloying/Formation of Solid Solutions

The typical approach to reduce the lattice thermal conductivity for the improvement of the various thermoelectric materials is through the alloying substitution. The isoelectronic alloying by creating point defects can reduced the lattice thermal conductivity. The large mass and radius contrast between the host atoms and impurity atoms is usually preferred aiming to disrupt the phonon path and minimize the phonon contribution to the total thermal conductivity. The experimental investigations, as well as, theoretical calculations of the disorder scattering parameter Γ and the theoretical lattice thermal conductivity have shown that isoelectronic alloying on different sublattices greatly decreases the lattice thermal conductivities of half-Heusler alloys due to enhanced mass and strain field fluctuation scattering caused by the difference of masses and radii between the impurity atoms and substituted atoms[13–17]. In addition, experimental and theoretical calculations of the electronic structures and thermoelectric performance of half-Heusler MNiSn (with M=Ti, Zr, Hf) materials mention that substituting Ti with Hf or Zr does not severely change the band structures of these systems[13–17].Recently, Zhang et al, in order to overcome the intrinsic the high thermal conductivity of ZrNiSn was performed experiments by substituted at the Sn-site with Si[17]. Based on the differences of the mass and radius between the Si-atom and Sn-atom the phonon was strongly scattered and the lattice thermal conductivity was reduced.[17] Surprisingly, the lattice thermal conductivity was reduced from the pristine ZrNiSn from 9.8 W/mK to 5.7 W/mK for the $ZrNiSn_{0.98}Si_{0.02}$ and reaches a figure of merit 0.78 at 873K which is 45% higher than the pure ZrNiSn.[17]

2.2.1.2 Nanostructuring

There are two types of nanostructured thermoelectric materials.

- Man-made nanostructured materials. This type is mainly single-phase materials and is defined as an assembly of nanosized particles or grains. This type of nanostructured materials is usually developed based on mechanical methods, such as mechanical alloying or even ball milling process. Such techniques can be also applied in mixture of different materials and form 2- or more-phase nanostructured materials.
- Self-made nanostructured materials. This second type is a system comprising a main solid phase (matrix) containing a secondary phase which is integrated into the matrix. In this case, the formation of nanophase comes from a typical precipitation process in a 2-phase region (see figure 9) of a well-chosen phase diagram[9,18,19] through nucleation and growth of the second phase. The second phase shall have low or no solubility in the solid state and in liquid state must be complete solute. When the corresponding melting diminishes by rapid cooling the second phase will precipitate as it reaches or exceeds the solubility limit in the solid state[9,20,21].

- In the case of nanostructured thermoelectric materials, the observed reduction of the lattice thermal conductivity significantly contributes to the enhancement of thermoelectric performance. This decrease in lattice thermal conductivity results from the enhanced scattering of phonons that carry heat from interfaces, and related effects result from nanostructures in a nano-scale system[9,22,23].

Nanostructured materials via mechanical techniques

Nanostructuring can be achieved by powder techniques (eg ball milling, mechanical alloying) as advantageous in industrial scale, because they provide the possibility of mass production, easy development in various shapes and above all the low cost compared to the usual techniques of developing nano-structures. Several examples on thermoelectric materials, such as PbTe[24], Bi_2Te_3 [25], Mg_2Si[26–29] and skutterudites[30] have proven that these techniques is an effective way to form bulk nanostructured materials with reduced lattice thermal conductivity.

Nanostructured materials via precipitation

The phenomenon of nanostructures via precipitation in highly efficient thermoelectrics was obtained first in lead-antimony-silver-tellurion system called 'LAST' AgPbmSbTe2+m. The low lattice thermal conductivity was achieved from precipitation of the secondary phase on a nano-scale inside the PbTe Matrix. Nanostructures were also obtained in the LAST-T($Ag(Pb_{1-x}Sn_x)mSbTe_2$+M and SALT($NaPbmSbTe_2$+m) system. The nanocrystals in figure 8 were endotaxially arranged in the matrix with good lattice coupling across the surface. The endotaxis is an important and favourable characteristic of the material for easy transport of carriers through the sample[9,31–33].

Today, it is well known that the nanostructures scatter more phonons at appropriate wavelengths than the solid solutions. The material 'LAST' exceptionally showed low lattice thermal conductivity and the actual value depended on the mass. According to the literature, the thermal conductivity of the PbTe was decreased from 2-2.5 W/m·K to 0.5-0.8 W/m·K and high ZT values e.g 1.7 at 700K[33] for the n-type 18%LAST were achieved.

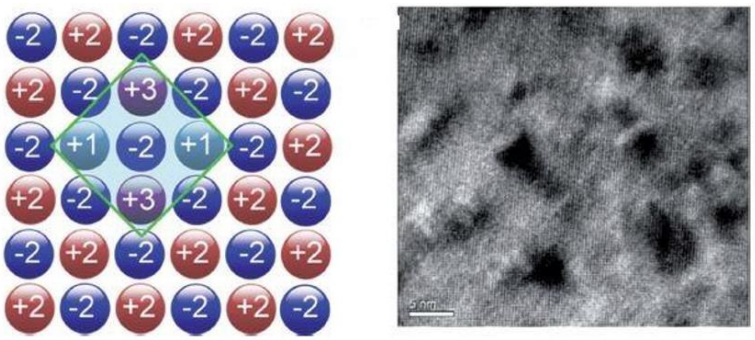

Figure 8: Endotaxial arrangement of nanocrystals in the lattice (left) the pairs +3 and +1 (alloying) occupied the+2 sites surrounding one -2 atom which is chemical and energy stable. On the right TEM image illustrate the mass and size fluctuations of nanodots (coherent or semicoherent) interfaces in the matrix.[9,31-33]

This approach was applied to various chalcogenides and successful examples are mainly PbTe-MTe (m=Ca,Sr,Ba and Cd)[34–36], PbSe-MSe (M=Ca,Sr,Ba,Zn and Cd)[37,38], and PbS-MS (M=Bi,Sb,Ca,Sr,Zn and Cd)[21,39].

Regarding to the PbTe system,the thermal conductivity was decreased from 2-2.5 W/m·K to 1W/m·K with the addition of 5%CaTe and the thermoelectric performance reached the value of ZT=1.5 at 765K.Moreover, with 3%BaTe the κ dropped down to 1.2 and figure of merit obtained the value of 1.3 at 760K also with 2% SrTe the ZT gained the highest value of 1.7 at 800K[34,36]. Another example is the PbTe-PbS system where the number density of precipitation increases with an increase in the PbS fraction and the lattice thermal conductivity at room temperature decreases from 0.9 W/mK to 0.45 W/mK[23,40,41]. On the other hand, PbSe-PbS systems with nanostructures do not greatly reduce thermal conductivity due to the fact that these nanostructures are insufficient to create strong phonon scattering in the matrix[41].

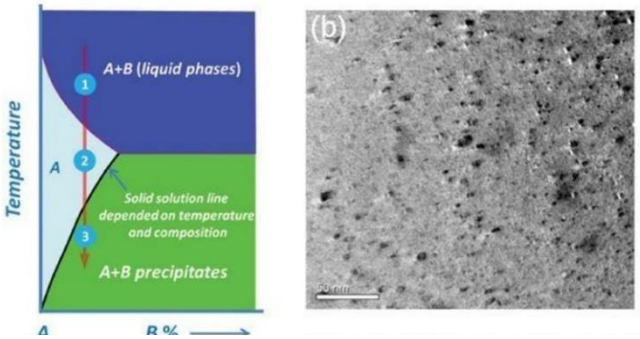

Figure 9: (Pseudo)-binary diagram for the formation of nanostructures A is the matrix and B the second phase the solubility of B in A(matrix) is dependent on the temperature. The TEM image on the right illustrate the nanostructure precipitates.[23,40-41]

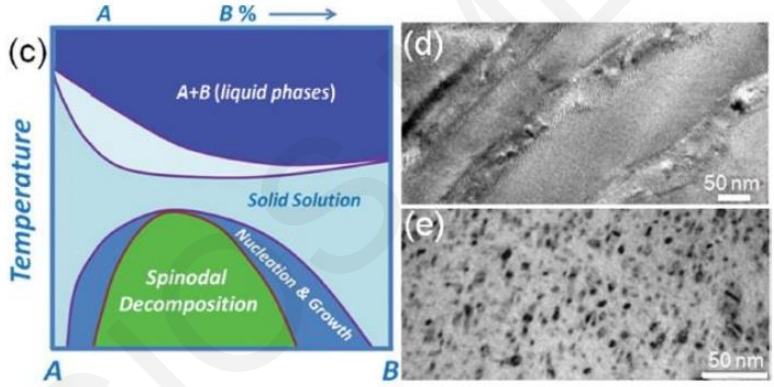

Figure 10: Schematic diagram for complete solid solution between the two phases A and B.The TEM images (d) illustrates the nanostructures due to spinodal decomposition and (e) it presents the nucleation and growth of nanostructures.[41]

2.2.1.2 All-Scale hierarchical architecturing

All-scale hierarchical architecture strategy involves the development of materials that their structural features cover a wider range of disorder scale from atomic level to meso- and micro-level.

N general, phonons with short and medium wavelengths are strongly scattered by point defects. The introduction of dopants causes mass difference or local bond strain to the lattice and can scatter the phonons with short wavelengths. In addition, the scattering of phonons with medium wavelength occur at the interfaces of the nanostructures between the precipitates and the matrix and also from the mass difference of the two phases. However, the acoustic phonons with long wavelength are unaffected and a new mechanism was required for several decades in the research of thermoelectric materials [5,42,43].Further scattering phonons requires breaking the crystals into mesoscopic particles (100nm-5μm) in order for the meso –scale grain boundaries to scatter longer long-wavelength phonons. Therefore, scattering across the range of MFPs from nano to micro size requires the all scale hierarchical architectures e.g. the integration of point defects of solid solutions, nanostructures and grain boundary interfaces (see fig.11)[9,44–46]

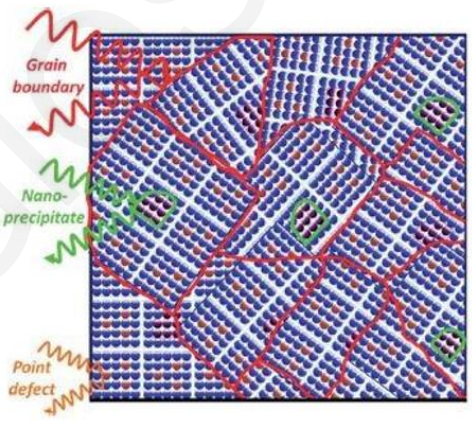

Figure 11: All scale hierarchical architecturing. Phonons can be scatter from point defects, nanoprecipitates and grain boundaries.[9,42-46]

Figure 12 illustrates the contribution scattering classification by the MFP range which calculated for Si and PbTe. The 25% of the κ_{lat} in silicon is due to atomic-scale point defects of solid solutions MFP<5nm, the 55% is evaluated by precipitations in nano-scale MFP (5-100 nm) and the rest by polycrystalline grain boundaries with MFP (0.1-1μm)[43]. Consequently, all scale sizes panoscopic structures in a material affect the scattering of phonons and should be the main design principle for future thermoelectric materials. All scale hierarchical architectures are successfully applied in chalcogenides system PbQ (Q=Te, Se and S)[39,47,48],half Heusler materials[49–51] and silicides[52].

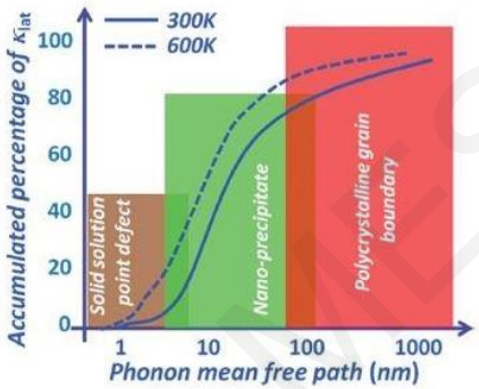

Figure 12: Schematic distribution of the reduction of κ_{lat} in a relation with phonons MFPs.[43]

2.2.2 Power Factor Optimization

2.2.2.1 Matrix Precipitate band alignment

The above-mentioned strategies mainly focus on reducing lattice thermal conductivity through a wide range of scattering of phonons over a multiple scale length. In all cases the power factor decreases with the single-phase matrix due to the nanoinclusions which increase carriers scattering resulting to their mobility reduction.

It is obvious that in order to achieve higher ZT values and to continue the development studies of such materials, a reduction in carriers mobility must be avoided. One strategy is to control and minimize the band offsets between the two phases. If the conduction bands of the matrix are energetically closed with these second phase then the electronic transmission through the

system is easier. This is more conducive to the transfer of holes if the two upper bands are energetically closed or aligned.[9]

The matrix and the secondary phase show large differences in band gaps. Nevertheless, the carriers can be easily transferred if there is a small difference in energy (ΔE) in the relevant valence or conduction band edges. The energy difference ΔE must be proportional to K_BT at elevated temperatures[39]. Figure 13 is illustrates a general idea for achieving this purpose. This strategy is applied except from Chalcogenides and to the SiGe systems and the Half Heusler materials[53,54]. A study shows an improvement in electrical conductivity by 54% for the $Si_{86.25}Ge_{13.75}P_{1.05}$ sample using the modulation/doping approach at $(Si_{95}Ge_5)_{0.65}(Si_{70}Ge_{30}P_3)_{0.35}$. The carriers flow inside the matrix can improve the Seebeck coefficient and the electrical conductivity as a result the enhancement of figure of merit ZT=1.3 at 1173K for the $(Si_{95}Ge_5)_{0.65}$ $(Si_{70}Ge_{30}P_3)_{0.35}$.[53]

Furthermore, a first study using the modulation doping approach was carried out for the ternary system TiNiSn. The modulation doping $(MnNiSb)_x$ with x = 0.05 at the $(TiNiSn)_{1-x}$ reduced the κ and they achieved 70% increase to the figure of merit and reached the value of 0.63[54].

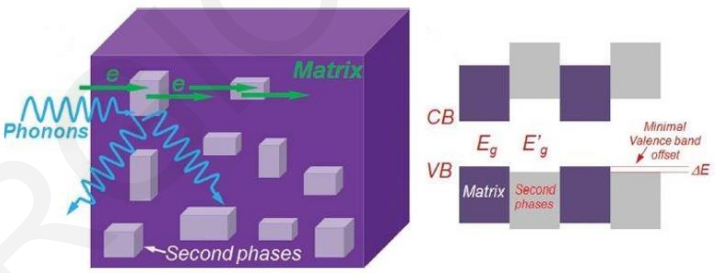

Figure 13: The second phases in the matrix scatter phonons at the matrix/nanostructure interfaces. The energy band diagrams of matrix and second phases exhibit that the energy difference in valence bands can lead to carriers transferred besides the large differences in semiconducting gaps E'g>Eg.[53,54]

2.2.2.2 Intra-matrix electronic structure engineering

This mechanism aims to increase the power factor and the ZT via the intra-matrix band engineering. The mechanism will be described from a calculation study which performed the Dr. G.H Fecher[55].

The system MNiSn (M=Ti,Zr,Hf) as it presented in figure 14 is a semiconductor with an indirect gap. The valence band is at Γ point and at the X point is the conduction band. The band gap ΔE_{gap} is 0.45ev. Many studies detected "in gap" states close to the Fermi edge which were created by chemical disorder and suggested that these states could be the key to control the thermoelectric properties.

These materials can be doped by electrons or holes and change the transport properties. The chemical potential changes its position owing to the doping. Thus, the heavily doped semiconductors will shift into the valence band (hole doping) or to the conduction band (electron doping). The fig.14 showed that the addition of 10%Nb as n-type donor in the Ti-site shift the Fermi Energy to the conduction band and the substitution of 10% Sc can shift the Fermi Energy to the valence band as a result the improvement of power factor and the overall figure of merit[55].

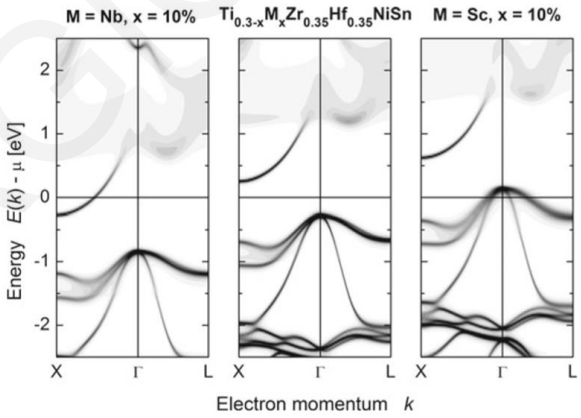

Figure 14: ab initio calculations of the electronic structure of n-type $Ti_{0.3}Zr_{0.35}Hf_{0.35}NiSn$ performed by Dr.G.H Fecher at Max- Planck-Institute. The Fermi Energy is shifted into the conduction band with Nb(n-type dopant) or to valence band with Sc(p-type dopant).[55]

Finally closing this section, the integration of all the mechanisms mentioned in a single system expect to give high thermoelectric performance. The figure 15 present how the different concepts synergistic together[9,37].

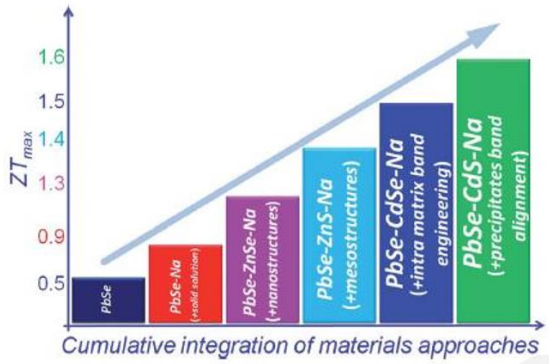

Figure 15: Combination of synergstic approaches can be enhanced the ZT a simple paradigm the PbSe system. [9,37]

2.3 Half Heusler materials

For all the aforementioned optimize strategies above lead the community to discovery new compounds and optimize them in order to find the optimum figure of merit. Fritz Heusler in 1903 discovered new compounds that have narrow band gaps and are suitable for thermoelectric applications Currently, only few Half Heusler (HH) compounds have been studied for their thermoelectric properties and in the next section will discussed the recent progress of these materials.

2.3.1 Physical Structure of Full and half Heusler

The Heusler compounds with elemental formula X_2YZ can be applied in the field of spintronics due to their magnetic properties. The Half Heusler are an alternative form of the Heusler compounds. They have chemical composition XYZ where X can be a transition metal, noble metal or a rare-earth element, Y is a transition metal, or a noble metal and Z is a main group element. The elements forms MgAgAs type of structure (Space group F43m), where the X, Y,

Z are arranged to form three interpenetrating Face Centered Cubic (FCC) Sublattices (see Fig16)[6,56].

This configuration of the elements causes a band gap in Half Heusler with range between 0.1ev to 3. 7ev. The most suitable are the compositions with 18 valence electron count (VEC) which are stable and have band gap 0-1.1ev. Thus, this group of materials expose excellent electrical properties, brilliant mechanical robustness and high thermal stability. Nevertheless, the high thermal conductivity from 6.7 up to 20W/mK is the major problem for thermoelectric applications[6,56].

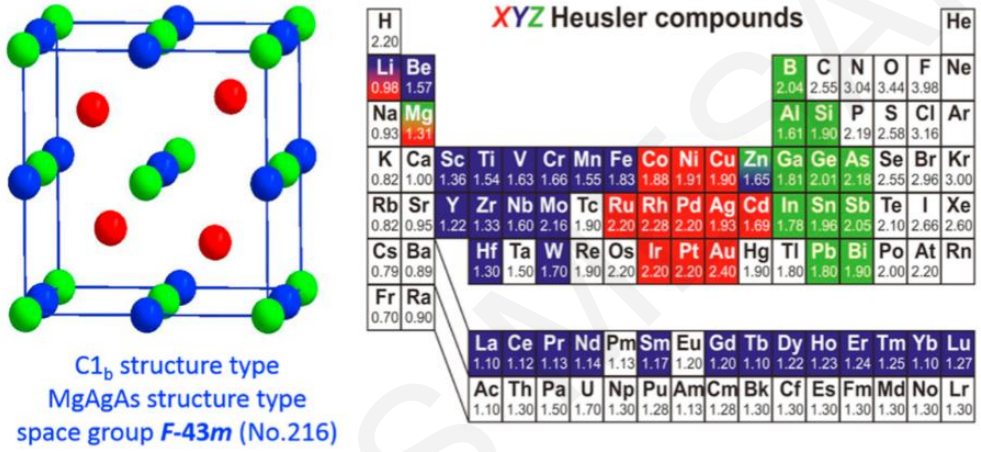

Figure 16: Crystal Structure of Half Heusler materials and Periodic table of elements with red colour are transition metal or noble metal or rare-earth element, with blue transition metals and green main group elements.[6,56]

2.3.2 Synthesis methods of half Heusler

Several methods have been applied to synthesize the HH materials. The combination of elements with high and low melting points in these compounds requires a high temperature alloying method.

From the first studies the Arc Melting (AM) method is increasingly used for synthesizing this type of materials. The method can be achieved by weighting the stoichiometric amounts of the elements and subsequently melting them in an Argon atmosphere. In order to ensure homogeneity, the ingot is crushed and re-melted 3 to 5 times[57–60].

Furthermore, induction melting[61,62], levitation melting (without crucible)[63,64], optical floating zone melting[65,66], are additional and similar methods to arc melting and are used to synthesize also the HH materials. The main difficulties from the above methods is the evaporation of the elements which have high vapor pressures such as Tin (Sn) and Antimony (Sb). To compensate the losses, the addition of an extra 5% of these materials is appropriate[61].

In relation with that, the solid-state reactions can reduce the material loss. The solid-state reactions methods require the starting materials be in form of powders, then, must mixed well and encapsulated in quartz tube in order to heat up at 850-900°C[67,68]. Although reducing the materials loss through this method, must kept in mind that it will take from few days to two weeks to complete the alloying.

Mechanical alloying (MA) is another solid-state technique which involves mix of reactive components at nanoscale and induce chemical reactions in powder mixtures at room temperature. Through MA method, energy is transferred to particles owing to frequent collisions that cause plastic deformation. The reactive surface increases with the reduction of breakage and particle size, thus the diffusion is enhanced and formed composite materials (See fig.17)[69,70]. Zou et al (2009) performed experiments to synthesize the ternary TiNiSn compound via Mechanical Alloying and stated that is not successful to synthesize due to limited energy input[71]. However, Monique et al., from first principle calculations showed that there is an optimum window to synthesize the TiNiSn compound via Mechanical alloying[70]. Additionally, the MA method is complex because the provided energy depends from various parameters such as: type of mill, milling containers and balls, rotational speed, ball to material ratio, hardness of the grinding bowls etc[69,70].

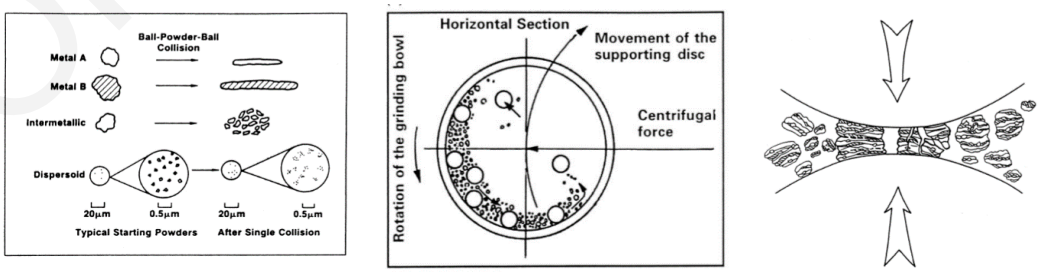

Figure 17: Mechanical alloying method- Metal A and Metal B are mix at ball milling vial and plastic deformation occur due to collisions.[69,70]

2.3.3 Research studies of n-type MNiSn (M=Ti,Hf,Zr)

The most well studied HH compounds are the n-type MNiSn and p-type MCoSb (M=Ti,Zr,Hf). The community emphasize to improve them due to their high potentials, both compounds have electrical resistivity 10^{-1}-10^{-3} Ω.cm at room temperature, consequently, with improvement of carrier mobility and carrier concentration will lead to higher values of electrical conductivity[56]. In this section the recent research for these compounds and especially for the n-type MNiSn (M=Ti, Zr, Hf) are discussed in detail.

Aliev et al. conducted resistivity experiments and showed that MNiSn (M=Ti,Zr,Hf) are semiconductors with band gaps of 0.12ev,0.18ev and 0.22ev respectively. Presently found that these compounds exhibit large Seebeck coefficients and are appropriate for thermoelectric applications[6,72,73]. Hohl et al. explored the TiNiSn, ZrNiSn and HfNiSn alloys and establish $Zr_{1-x}Hf_xNiSn$ alloys form solid solutions with reduced thermal conductivity. In a relation with that the power factors were not affected upon alloying[74].

Uher et al. revealed that the annealing treatments can suppressed the lattice thermal conductivity. Furthermore, they announced that Sb is an efficient dopant for the Sn sites of the $Zr_{1-x}Hf_xNiSn$ alloy[75]. That is also confirmed from other reports which show that 0.5-2.5% replacement of Sn by Sb is the optimized doping level[56,76,77]. The rise of carrier concentration enhances the power factor. This can be accomplished with alloying dopants in the lattice.

Many studies showed that intermixing of Hf, Zr and Ti is not improving the electrical conductivity too much[78,79]. A study unveiled that the $Hf_{0.5}Ti_{0.5}NiSn$ has lower carrier concentration than the ternary systems TiNiSn and HfNiSn[80]. The Hf-Zr intermixing in the MNiSn affect most the carrier mobility and increase the electrical conductivity. The interchanging of Hf,Zr and Ti does not modify the valence electron count thus elements with different valence electrons are most efficient dopants[81].
The n-type MNiSn system can be doped from the M-site via (Ce, La, Nb, Ta and V), at the Ni site (Cr, Cu and Fe) and at the Sn site (Bi,Ge,Pb,Te and Sb[61,78,82].

Another way to increase the carrier concentrations, except from the formation of metallic nanoprecipitates through doping, is to use the grain boundary engineering approach. Makongo et al displayed that the creation of Full Heusler phase in the grain boundaries between the Half Heusler phase enhanced the Seebeck coefficient without reduction of the electrical conductivity. The creation of Full Heusler nanoinclusions can filter out low energy carriers and keep the high mobility of the remaining charge carriers that is explained in Fig 18[56,67].

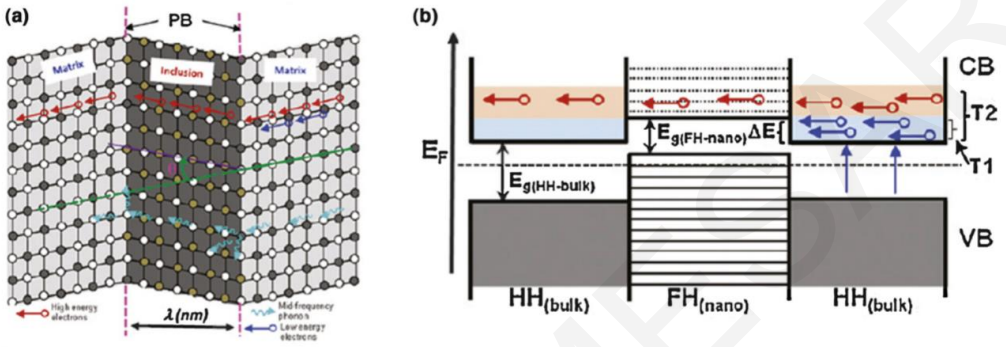

Figure 18: a: Is a schematic illustration of boundaries it displays the Half Heusler (matrix) with Full Heusler nanoinclusions and b: is illustrated the band diagram between them the ΔE is the energy barrier and at T1 and T2 is the temperatures that carriers excited.[56,57]

As prior mentioned, isoelectronic doping does not affect the electrical conductivity and the electronic part of the thermal conductivity. The binary combination of Hf, Zr, Ti or ternary alloying can reduce the thermal conductivity[83,84]. A simple paradigm is illustrated in Fig 19 in which the addition of titanium reduces the thermal conductivity from 4.7W/mK to 3.2W/mK[56,57]. Supplementary reduction in the thermal conductivity is achieved with the increasing phonon scattering in the grain boundaries. This is carried out via high energy ball milling and sintering in order to gain small grain sizes. The thermal conductivity of $TiNiSn_{1-x}Sb_x$ with average grain size 50 nm drops from 10.6W/mK to 3.7W/mK[56,77,85]. Katayama et al, stated that is feasible a reduction 17.9% and 36.3% in the thermal conductivity via Zr and Hf doping respectively compared to undoped TiNiSn[86].Hohl et al,obtained a κ=5.4W/mK in Ta-doped $Zr_{0.5}Hf_{0.5}NiSn$ at 700K and earned a figure of merit 0.5 [78]. Joshi et al, achieved a minimum thermal conductivity κ_{min}=3.15W/m·K at room temperature for the $Ti_{0.25}Zr_{0.25}Hf_{0.5}NiSn_{0.99}Sb_{0.01}$.[59] Furthermore, if the Ni atom is partially substituted by the Pd atom the ZT is enriched the value of 0.7 for the $Zr_{0.5}Hf_{0.5}Ni_{0.8}Pd_{0.2}Sn_{0.99}Sb_{0.01}$.[87] Zhang et al,

maximized the figure of merit of undoped TiNiSn to 0.84 using different sieves mesh sizes, however, the time-consuming additional processes remains the main barrier of this method.[88]

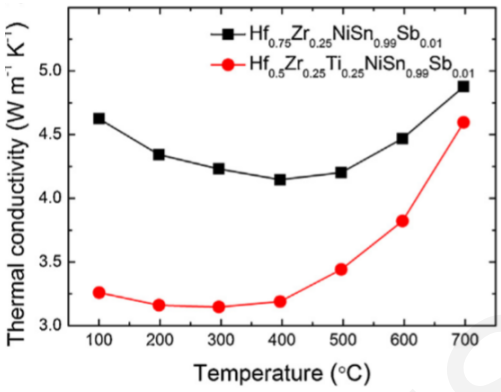

Figure 19: Addition of 25% Titanium suppress the thermal conductivity from 4.7-3.2W/m*K.[56,57]

The MNiSn compounds were widely studied in terms of properties but to fabricate devices with high performance is necessary to investigate the material stability at high temperatures. First studies showed that annealing of the undoped MNiSn at 800°C for two to ten days[75], at 900°C for 14h and at 800°C for one to seven days enhanced the structural ordering and increase the electrical conductivity[89,90].

Other studies showed that for the samples with metallic and impurity phases the most suitable annealing temperature is at 890°C resulting to the elevation of Seebeck Coefficient and electrical conductivity. Moreover, for doped samples the annealing times accelerate the uniform distribution of the dopant and improve the electrical conductivity[89,91,92].

However, the stability studies until now show the improvement of the electrical conductivity. The improvement of Seebeck coefficient and electrical conductivity are expected in high annealing temperatures. Thus, further studies in thermal stability are necessary.

The current state-of -the-art for the n-type MNiSn and p-type MCoSb is summarised in Fig.20.The synergy of all approaches results in high ZT values. The optimum ZT is 1.3 for the composition $(Hf_{0.6}Zr_{0.4})_{0.99}V_{0.01}NiSn_{0.995}Sb_{0.005}$ which is synthesized via Arc Melting and SPS[93].The composition $Ti_{0.5}(Zr_{0.5},Hf_{0.5})_{0.5}NiSn_{0.998}$ is not taken into consideration due the over-estimated values ZT=1.5 and it never reproduced by any other group[60].However, different compositions of half Heusler can exposed values higher than 1 for the compositions of LaPtSb which the overall figure of merit is 1.8.

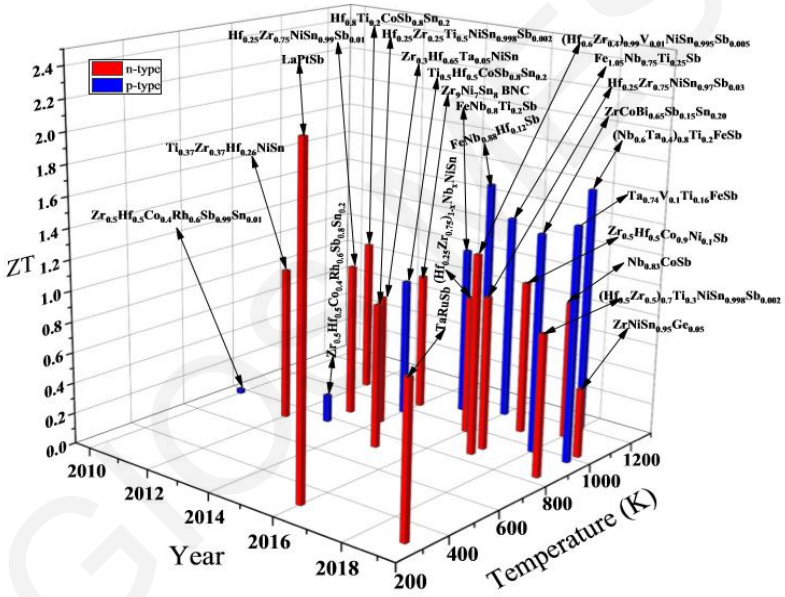

Figure 20: Current state-of-the-art for n and p-type Half Heusler materials.[94]

The table 1 summarizes all the interesting compositions until now and leads us to explore compositions with less Hf or Hf-free in order to comply the regulation of decrease the world market price of raw elements.[94]

Compositions	Methods	ZT	Comments
$Ti_X(Zr_{0.5}Hf_{0.5})_{1-x}NiSn$	Arc Melting+HP		over-estimated values MMR Tech
$Ti_{0.5}(Zr_{0.5}\ Hf_{0.5})_{0.5}NiSn_{0.998}$ [60]		1.3	
$Ti_{0.5}(Zr_{0.5}\ Hf_{0.5})_{0.5}NiSn_{0.998}Sb_{0.002}$		1.5	
$(Hf_{0.6}Zr_{0.4})_{1-x}M_xNiSn_{0.995}\ Sb_{0.005}$ (M=V, Nb, and Ta) [93]	Arc Melting+SPS		
$(Hf_{0.6}Zr_{0.4})_{0.99}V_{0.01}NiSn_{0.995}Sb_{0.005}$		1.3	V is a resonant dopant
$(Hf_{0.6}Zr_{0.4})_{0.99}Nb_{0.01}\ NiSn_{0.995}Sb_{0.005}$		1.2	Nb normal dopant
$(Hf_{0.6}Zr_{0.4})_{0.99}Ta_{0.01}NiSn_{0.995}\ Sb_{0.005}$			Ta normal dopant
$Ti_{0.37}Zr_{0.37}Hf_{0.26}NiSn$ [95]	Arc Melting+SPS	1	Phase separation
$Hf_xZr_{1-x}NiSn_{0.99}Sb_{0.01}$ [81]			
$Hf_{0.25}Zr_{0.75}NiSn_{0.99}\ Sb_{0.01}$	Arc Melting+Ball Milling+HP	1	smaller grain sizes reduction of κlat
$Hf_{0.6}Zr_{0.4}NiSn_{0.98}Sb_{0.02}$	Suspension melting	1	
$Hf_{0.25}Zr_{0.25}Ti_{0.5}NiSn_{0.998}Sb_{0.002}$ [63]	Induction Melting+Annealing+Ball Milling+SPS	0.94	
$(Hf_{0.5}Zr_{0.5})_{0.7}Ti_{0.3}NiSn_{0.998}Sb_{0.002}$ [96]	Induction Melting+Annealing+Ball Milling+SPS	0.92	
$TiNi_{1+x}Sn$	Arc Melting +SPS		
$TiNi_{1.1}Sn$ [97]		0.5	Ni excess degreased the κ, phase separatio FH
$Zr_xTi_{1-x}NiSn$	Microwave heating		
$Zr_{0.3}Ti_{0.7}NiSn$ [98]		0.60	grain size 10μm
TiNiSn	Arc Melting/Sieving	0.84	grain size

Table 1: Summarize all the interesting compositions with optimum figure of merit up today.

2.3.4 Motivation and Objectives

As previously discussed, among the different families of half Heusler materials the MNiSn and MCoSb (M=Ti,Zr,Hf) compounds are strong candidates for thermoelectric applications. Up to date, the best figure of merit for the n-type half Heusler is 1.5 at 700K for Sb-doped $Hf_{0.25}Zr_{0.25}Ti_{0.5}NiSn$[60], while for the p-type is 1.5 at 973K for the $ZrCoBi_{0.65}Sb_{0.15}Sn_{0.2}$[99,100]. Moreover, besides the high figure of merit, these materials seem to be applicable due to their thermal stability as well as mechanical behavior; critical parameters for the development of thermoelectric modules for medium range temperatures.

Aiming to further improve this system and push it closer to the application, the development of half-Heusler materials with *high thermoelectric performance* via a *scalable synthesis method* was our main objective. Mechanical alloying method was selected as (a) the "scalable synthesis method" where (b) the in-situ development of hierarchical structural features for the reduction of the thermal conductivity, thus, the fabrication of half-Heusler materials with "high thermoelectric performance" was possible in the synthesis step. Moreover, scalability and simplicity are also important practical advantages for mechanical alloying method compare to commonly applied arc melting method where additional treatments (i.e. long annealing and ball milling) to improve the thermoelectric properties are also required necessary.
n-type half-Heusler (Ti,Zr,Hf)NiSn materials were selected for the application of this approach and the investigation of the developed structural features aiming to introduce/form:

- disorder at atomic level via Ti/Zr/Hf substitution
- nano-crystalline particles during mechanical alloying synthesis method
- micro-grains during mechanical alloying synthesis and, mainly, sintering process

More specifically, (Ti,Zr,Hf)NiSn solid solutions series were selected and compositions on the edges as well as inside the triangular phase diagram starting from TiNiSn.

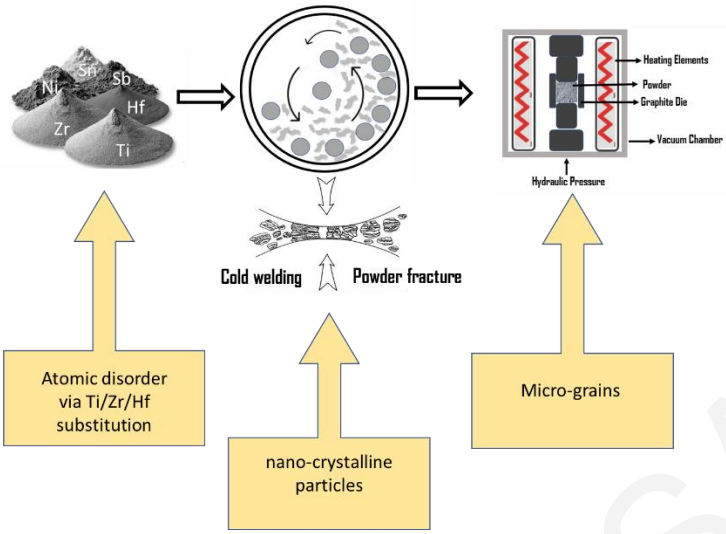

Figure 21: The different approaches which included in Mechanical alloying synthesis

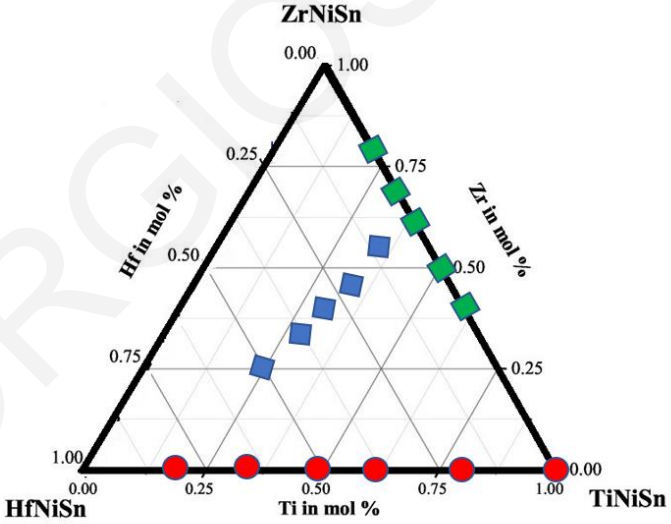

Figure 22: The triangle of the studied compositions.

Chapter 3

3.Synthesis and Characterization Methods

In this chapter, the composition techniques and the experimental equipment used to produce these materials as well as the characterization techniques and the evaluation of thermoelectric properties will be discussed.

3.1 Synthesis of half Heusler

3.1.1 Mechanical Alloying vs Arc Melting

The technology of powder metallurgy is the most commonly used method to fabricate half Heusler materials. For example, in the arc melting processing the ingots are pulverized to small particles and then compacted via spark plasma sintering or hot pressing leading to the formation of sample with multiple phases or impurity phases such as: $(Hf,Zr)_5Sn_3$, $TiNi_2Sn$, Ti_6Sn_5 and unalloyed Sn[91,92]. To eliminate the impurity phases, annealing at temperatures 900-1050°C for 3 to 7 days must be carried out[91,92]. Thus, additional treatments must carry out in order to obtain nanocrystalline HH materials with sizes~50nm[57].

Mechanical alloying (MA) can be used as alternative technique to synthesize direct this type of materials avoiding the additional steps. In MA repeated welding, fracturing and rewelding of powder particles occur for the formation of various compounds via solid state diffusion[69]. The methodology of the two different techniques (MA vs arc melting) is compared in Figure 23. The fewer multiple processing steps, the possibility of scalling up as well as the formation of materials with nanostructures with low values of lattice thermal conductivity are some advantages of this method[101].

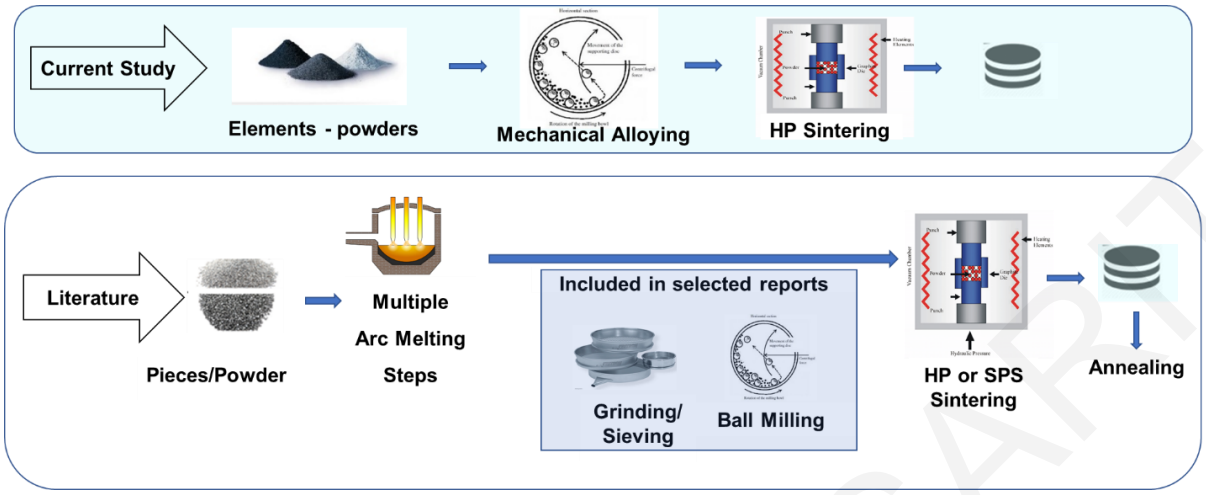

Figure 23: Comparison of two methodologies Mechanical alloying above and Arc melting.[101]

3.1.2 Mechanical alloying synthesis

Figure 24 is presents the methodology of the MA technique. Clearly seems to be simpler compared to other techniques. The starting materials are weighted to the tungsten carbide vial and milled under high speed in planetary ball mill and then sintered in a hot press or spark plasma sintering furnace. The crucial parameters that affect the synthesis method are the number of balls, time of milling/pause, as well as the speed and the type of mill. The most significant parameters are the time and the speed of milling[70]. Based on literature, the half Heusler can synthesized in an energy window between 500-700 rpm[70]. Based on this finding as well as our preliminary experiments the speed of 600rpm was selected for the current studies. The experiments in lower speeds exposed impurity phases and mainly create the Ni_3Sn_4 phase which is metallic and is affect significant the thermoelectric properties. More information about the chemical composition ball to material ratio and the synthesis is included at Chapter 4 and 5 for the current studies. The MA method is attractive method because includes only two processing steps compared to other techniques which used multiple steps. This has as a result also the reduction of materials loss through evaporation.

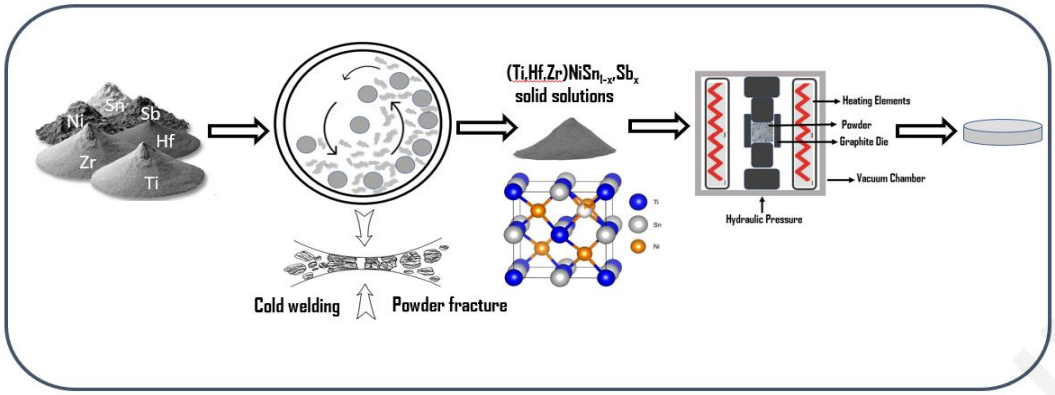

Figure 24: Methodology of Mechanical alloying.

3.1.3 Hot Pressing (HP)

In order to take the final pellet, which will undergo characterization and measurement of the properties, a sintering stage of the milled powders is needed. The sintering process is carried out through the high temperature press system (see figure 25). The pellet can be developed by simultaneous application of pressure and heating. The process is done under a flow of inert gas or under vacuum. The maximum force that can be applied is 200kN and a maximum temperature of 2000ºC. The chamber before conducting the experiments, is placed under a vacuum<20mtorr and purged with inert gas in order to maintain inert atmosphere[102]. Taking into consideration the theoretical density of the different stoichiometries the sintering experiments was carried out in a temperature range of 1100-1150K based on literature. The density of the polished samples (see figure 26) evaluated based on Archimedes method and was 99% of the theoretical then the thermoelectric characterization was carried out.

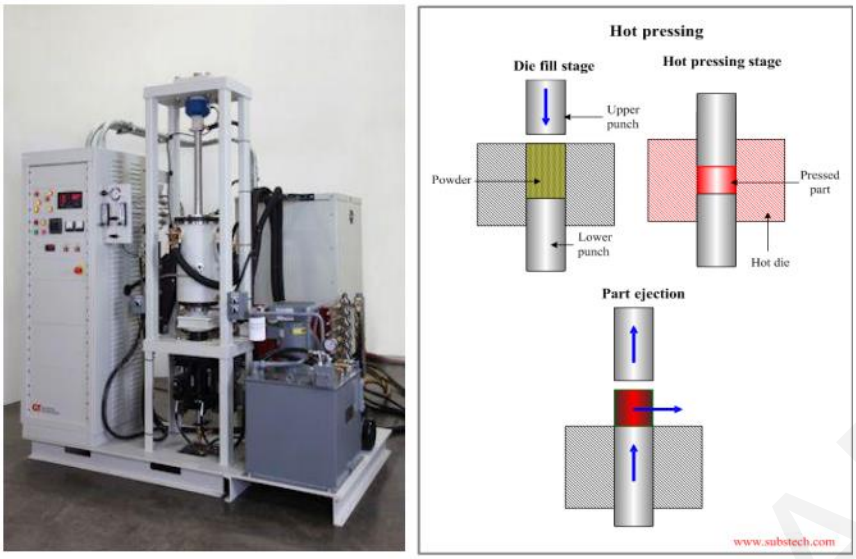

Figure 25: Hot Press system for sintering.[102]

Figure 26: Polished pellet after sintering**.**

3.1.3 Structural Characterization

3.1.3.1 P-XRD Diffraction

After the different stages of synthesis and after the sintering process it is necessary to characterize the fine powders using X-ray diffraction to show how the powders react between them up to the final pellet. The aim is mainly to distinguish the structures of the materials if they are crystalline or amorphous, to make a quantitative and qualitative analysis of the dopant material which enters to the lattice, i.e. shift of the peaks to smaller angles of 2θ which is translate to large unit cell. Additionally, the crystallite size can be estimated from the range of peaks. To characterize the materials of this project, the Rigaku Miniflex has been used (figure 25)[103]

The principle of X-ray diffraction pattern is presented in (figure 27). When an X-rays beam incident on a polycrystalline sample with a specified wavelength (λ), in our case CuKa λ=1.54, and by changing the angle of the incident ray with respect to the sample, the diffracted rays will be sequentially detected by the detector at angles 2θ.That angles represents the lattice planes satisfying it Bragg's condition[103]:

$$2dSin\theta = \lambda \quad (21)$$

The lattice constant can easily be estimated from the measurement of Bragg the angle θ. The identification of the diffraction patterns is identified by ICDD (International Center for Diffraction Data) standard data (see figure 28) theoretical xrd of TiNiSn[103].Scanning the sample through a wide range of 2θ angles, all possible diffraction directions of the lattice are attained.

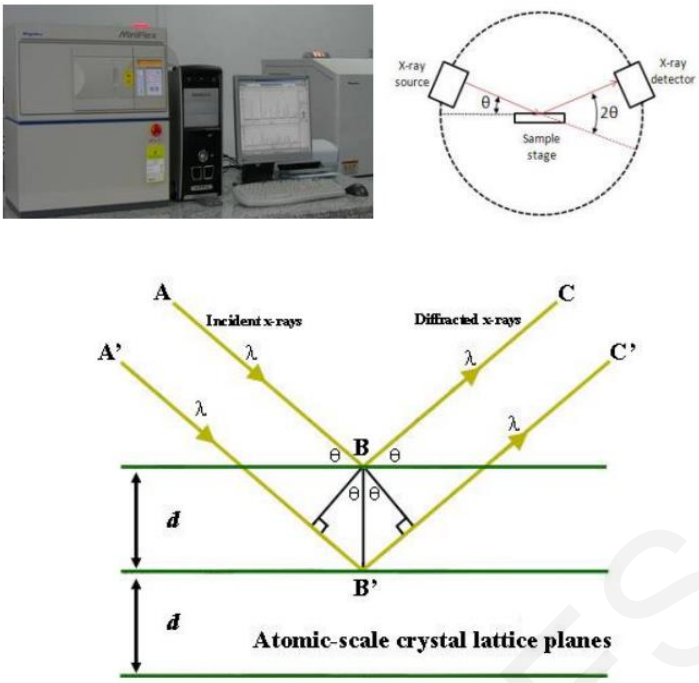

Figure 27: Braggs Law and principle of x-ray diffraction.[103]

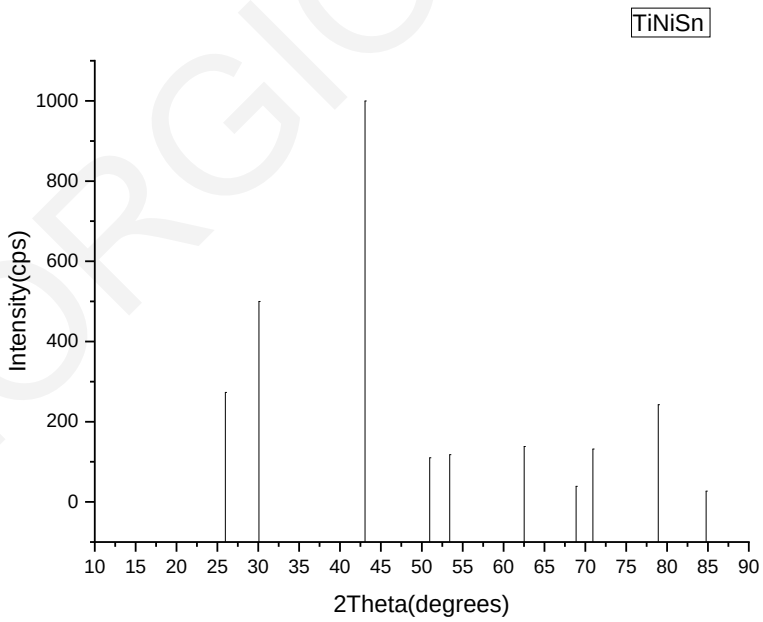

Figure 28: Theoretical xrd of TiNiSn

3.1.3.2 Scanning electron microscopy (SEM)

A technique for studying samples through the use of an electron beam is the scanning electron microscope (SEM) (figure 29). The scanning microscope is using a focused beam of high energy electrons 1-50kev.The beam passes through a sequence of two or three focusing lenses, which are combined with suitable diaphragms with the help of a coil, and systematically scans the surface of the sample[104].

When the beam interacts with the sample various types of signals are obtained (figure 27), such as secondary electrons which give high resolution images on specimen morphology and information on the size and shape of the particles. Furthermore, the backscattered electrons can give information for the chemical composition of the elements, especially for solids solutions we can distinguish the different phases by contrast to brightness[104]. In figure 30 is presented a backscattered image of a HH sample prepared via Arc melting. It is obvious the phase separation and impurity phases such as Ti_5Sn_3 .[105]

Auger electrons can be detected and give information about the composition of the materials as well. Using an EDX sensor the X-rays fluorescence can be recorded in order to perform elemental analysis mapping on multiphase samples.[104]
The phenomena that will be observed are affected by the amount of interaction of the beam with the sample as well as with the penetration depth of the beam (figure 27 right). Thus, the angle of the incidence beam, the current, the acceleration tendency and the average atomic number Z of the sample plays a decisive role. Maximum magnification for average SEM imaging is up to 500,000X[104].

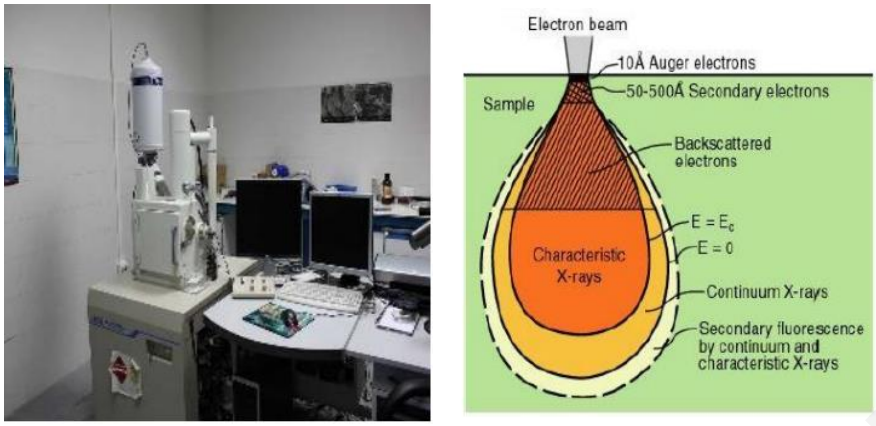

Figure 29: Scanning electron microscope and interaction of incident beam.[104]

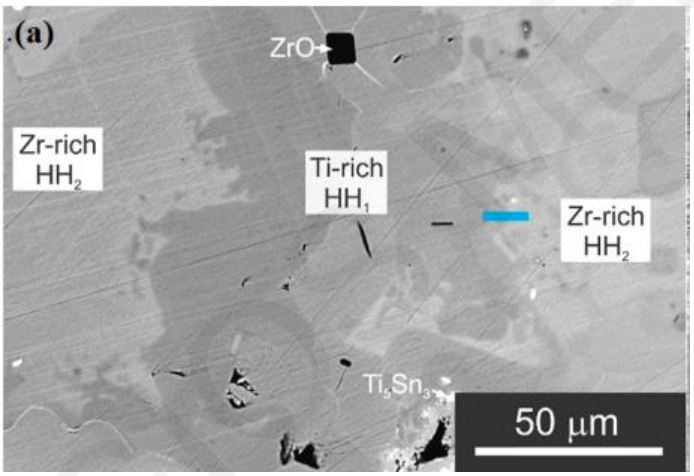

Figure 30: Backscattered image of HH sample prepared by arc melting.[105]

3.1.3.3 Transmission electron microscopy (TEM)

The Transmission electron microscope uses an electron gun at the top of the instrument and emits electrons through a vacuum tube. Then, the electrons are focused into a fine beam due to the electromagnetic lenses. The focused beam passes through a very thin specimen, and the electrons either scatter or hit a fluorescent screen at the bottom of the microscope. An image of the specimen with its assorted parts is shown on the screen in different shades according to its density. Figure 31 shows an example of bright field (BF) image of a TiNiSn HH sample[105].The image revealed the microstructure of the HH matrix along with SAD patterns.In that sample are also observed platelets and spherical precipitate[105]. In this project, a JEOL 2011 microscope, operating at an accelerating voltage of 200 kV with a point resolution of 0.25 nm and equipped with an EDS detector (EDAX Apollo XLT TEMSDD) was employed for transmission electron microscopy (TEM, HRTEM) experiments. Samples suitable for TEM-HRTEM were prepared by dispersing crushed material on ultrathin lacey C-films supported on 3.05 mm copper grids.

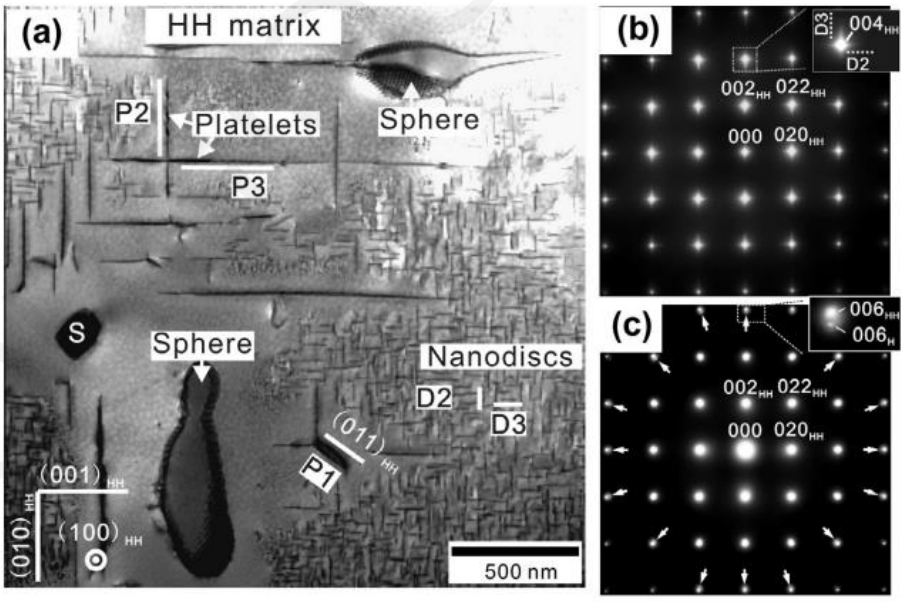

Figure 31: Bright field image of TiNiSn sample along with SAD patterns.[105]

3.1.4 Thermoelectric Characterization

3.1.4.1 Laser flash Analysis

The laser flash analysis technique is a fast, absolute method, without any contact on the sample. This method is giving the ability to calculate the thermophysical properties which include thermal diffusivity, specific heat capacity and thermal conductivity. The data which obtained by this method can be used to optimize TE materials with low lattice thermal conductivity and high figure of merit (ZT).

The LFA method is illustrated in figure 32 where the front surface of a parallel sample is heated by a laser pulse and on the back surface the rise in temperature with respect to time is measured using an IR detector. The thermal diffusivity (a), and in most cases the specific heat capacity at constant pressure (Cp) can be determined from the measured signal[106].

The estimation of the thermal diffusivity can be achieved from the half time $t_{1/2}$ (time corresponding to half the step height). The specific heat can be determined from the total temperature increase (step height). It is indirectly proportional to the heat capacity of the sample (figure 32 right). The Cp of an unknown material can be calculated by comparing the signal heights between sample and reference as follows[106]:

$$C_p(T) = \frac{{T_\infty}^{ref} . Q^{sample} . V^{sample} . \rho^{ref} . t^{ref} . {d_{sample}}^2}{{T_\infty}^{sample} . Q^{ref} . V^{ref} . \rho^{sample} . t^{sample} . {d_{ref}}^2} . {C^{ref}}_p(T) \quad (22)$$

Where, T the height of the detector signals (Temperature), Q the laser energy, V the amplification factor, ρ the density, t the thickness of the sample or reference and d the opening diameter of the sample holder.

If the density (ρ) of the sample is known then the thermal conductivity (K) can be calculated from the relationship[106]:

$$\kappa = \alpha . \rho . C_p \quad (23)$$

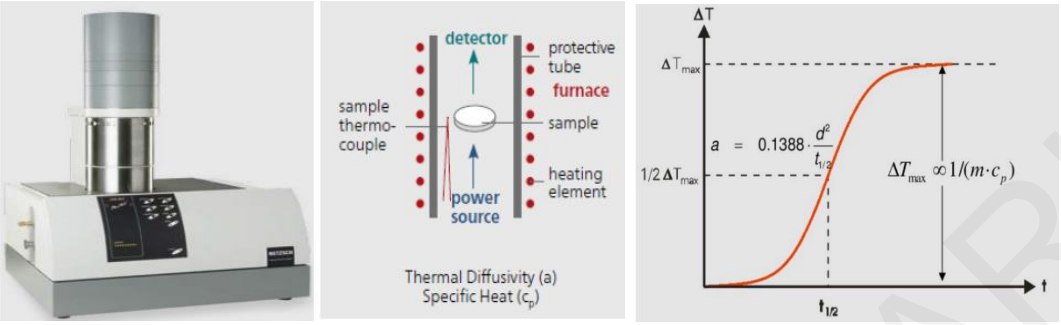

Figure 32: Principle of LFA and signal of IR detector.[106]

3.1.4.2 Four-Probe method Ulvac Zem-3

To estimate the electrical conductivity (σ) and Seebeck coefficient (S) the ULVAC ZEM-3 instrument was used (figure 33). A rectangular sample is placed in a vertical position between the upper and lower parts of the heating chamber. While the sample is heated and held at a specified temperature then is heated by the heater in the lower part to give a temperature gradient[107].

The Seebeck coefficient (S) is measured from the top and bottom measurements temperatures T1 and T2, from the thermocouples that press the sample on one side and from the subsequent measurement of the thermal electromotive force dE between the same wires on the thermocouple side[107].

The electric resistance (R) is measured by the four-probe method, in which it is applied a constant current I, so that at both ends of the sample it is measured and determine the voltage V between the same wires of the thermocouple but subtracting the thermal electromotive force dE between the conductors. Moreover, if the thickness (D), width (W) and distance between the probes (h) are known the electrical resistivity(d) can be calculated[107].
The instrument has the ability through the automatic system to examine whether the contact is ohmic or not and considers the best value of electric current to determine the resistance of the

sample without the presence of convection effects heat, in addition it can accept a sample length of 6 to 22mm.[107]

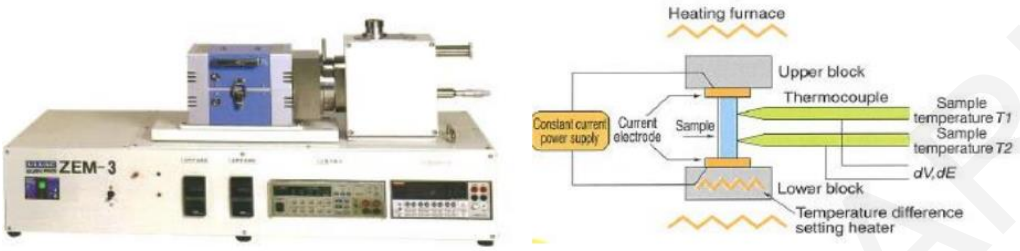

Figure 33: Ulvac ZEM-3 instrument and the principle.[107]

Chapter 4

4.n-type half Heusler Ti-Zr system

In this chapter, the synthesis of n-type TiNiSn and (Zr,Ti)NiSn solid solutions via MA followed by hot press sintering is explored for the first time, in order to evaluate the potential of this method for the development of highly efficient TE materials. Additionally, the effect of the processing conditions on the structure as well as the thermoelectric properties are discussed.

4.1 Synthesis of half Heusler materials

Previous work on the synthesis of TiNiSn via MA showed that there is an energy window to directly obtain pure material[70].This window corresponds to the mill rotation speeds between 500 to 700 rpm. Based on this finding as well as our preliminary experiments, the speed of 600 rpm was selected for this work and the MA duration was further investigated. The high purity elemental powders of Ti (99.99% Alfa Johnson Matthey GmbH, Germany), Zr (99% US Research Nanomaterials Inc, USA), Ni (99.99% Sigma Aldrich Merck, Germany), Sn (99.85% Alfa Johnson Matthey GmbH, Germany) and Sb (99.9% Alfa Johnson Matthey GmbH, Germany) were weighed according to the selected compositions ($Ti_{1-x}Zr_xNiSn$ with x=0, 0.40, 0.50, 0.60, 0.70 and 0.80 and $Ti_{0.4}Zr_{0.6}NiSn_{1-y}Sb_y$ with y=0.01, 0.015 and 0.02) in a tungsten carbide ball milling vial with ball-to-material ratio 10:1. The raw materials were milled under Ar at speeds of 600rpm using a planetary ball mill (Pulverisette 7 Fritsch) followed by sintering via hot pressing (HP) at 1100-1150K for 1 hr and 50MPa. The density of the sintered pellets was >99% of the theoretical density for each composition.

4.2 Structure of Ti-Zr system

4.2.1 TiNiSn-end member

Ti, Ni and Sn were milled for several hours and the powder XRD patterns for 3, 6 and 9 hrs are illustrated in Figure 34. After 3 hours of milling, a half Heusler phase was identified, however, secondary phases such as Ni_3Sn_4 and free Sn were also present. Further milling for 6 hours and 9 hours resulted in the elimination of the secondary phases and the TiNiSn phase XRD peaks were only present. However, the presence of the full Heusler $TiNi_2Sn$ phase cannot be excluded at this stage due to the peak broadening. After hot press sintering at 1100K, the peaks became sharper, as expected, and a small amount of $TiNi_2Sn$ was now clearly observed.

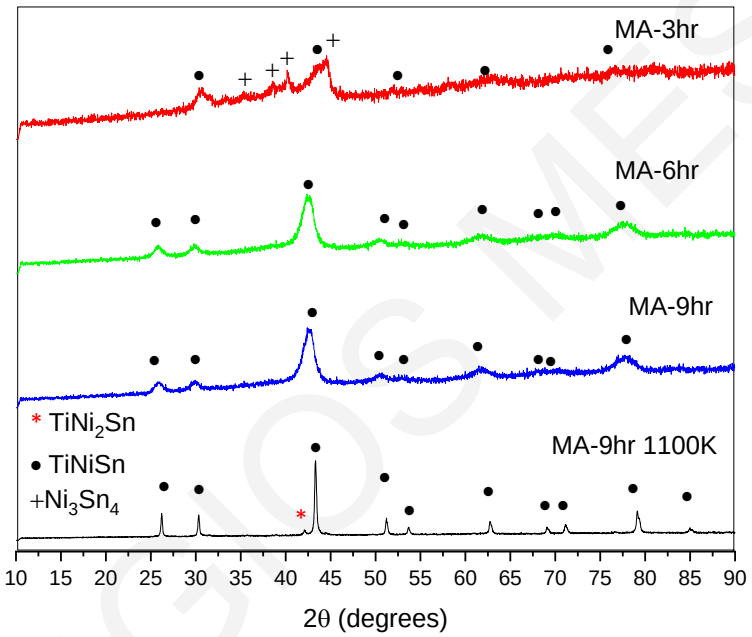

Figure 34: PXRD pattern of TiNiSn after MA of 3, 6 and 9hrs as well as after 9 hr MA and HP sintering.[101]

Typical SEM images from the TiNiSn sample are shown in Figure 35, where the Backscattered images (BSE) showed phase separation (i.e. darker and lighter areas). Based on the Energy Dispersive X-Ray Spectra (EDS results), see Table II, the darker areas have some Sn deficiency suggesting that further homogenization is required.

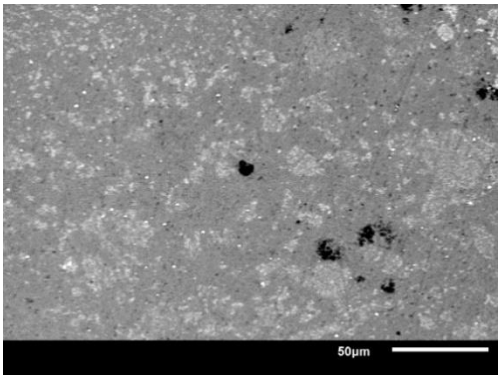

Figure 35: SEM image of TiNiSn prepared by MA.[101]

Table 2: EDS results for the TiNiSn prepared by MA and HP sintering

	Ti	Ni	Sn
Nominal Composition	1.00	1.00	1.00
Light Area	0.80	1.05	1.15
Dark Area	1.08	1.00	0.92

4.2.2 $Ti_{1-x}Zr_xNiSn$ and Sb-doped Solid Solutions

4.2.2.1 Powder x-ray diffraction

Ti, Zr, Ni and Sn elements were milled for several hours for the synthesis of the solid solutions of different compositions. The rotation speed was set again at 600 rpm based on aforementioned results and literature [70].

Effect of MA duration

Figure 36 shows the powder XRD patterns of the material with nominal compositions x=0.4 mechanically alloyed for 7, 8 and 9 hrs. It is clear that the formation of half Heusler is feasible and a minimum required milling time to synthesize single phase HH powders was observed. Below this minimum duration, secondary phases (i.e. Ni_3Sn_4) existed for all compositions in the solid solution series in agreement with the literature for the end-member TiNiSn[70]. At higher milling times, the structure of the alloyed powders remained the same for all compositions. Interestingly, the minimum required milling time shows an overall increasing

trend with Zr concentration, except for the member x=0.6 whose milling time of only 7 hrs was enough to reproducibly get the desired phase.

In order to further study the properties, the materials prepared with minimum required MA time (Table III) were sintered via HP and powder XRD measurements have been conducted, see Figure 36a. The sintering process was carried out at a temperature range between 1100-1150K, resulting in sharp powder XRD peaks that correspond exclusively to the (Zr,Ti)NiSn Half Heusler structure. The patterns were identical for all $Ti_{1-x}Zr_xNiSn$ series with x=0.40, 0.50, 0.60, 0.70 and 0.80, see Figure 37a. Moreover, Figure 37b shows the shifted peaks (inset) and the increase in the unit cell with Zr concentration following Vegard's law. Furthermore, lattice parameters were in good agreement with literature[108].

Effect of Sb-doping

In our efforts to modify the properties of the half Heusler compounds synthesized by MA followed by HP sintering, member x=0.6 was selected for further studies due to its promising thermoelectric properties (see part 4.3.1). Sb was selected as a dopant according to $Ti_{0.4}Zr_{0.6}NiSn_{1-y}Sb_y$ formula for y values up to 0.02. Powder XRD patterns of MA Sb-doped powders showed single (Zr,Ti)NiSn Half Heusler structure. However, these Sb-doped compositions were more sensitive to the formation of Ni_3Sn_4 phase after HP sintering. The powder XRD patterns clearly show that a small amount of binary Ni_3Sn_4 phase was formed in all series, see Figure 37a for y=0.015. Further milling and/or different sintering temperature had no effect, as Ni_3Sn_4 has been always present.

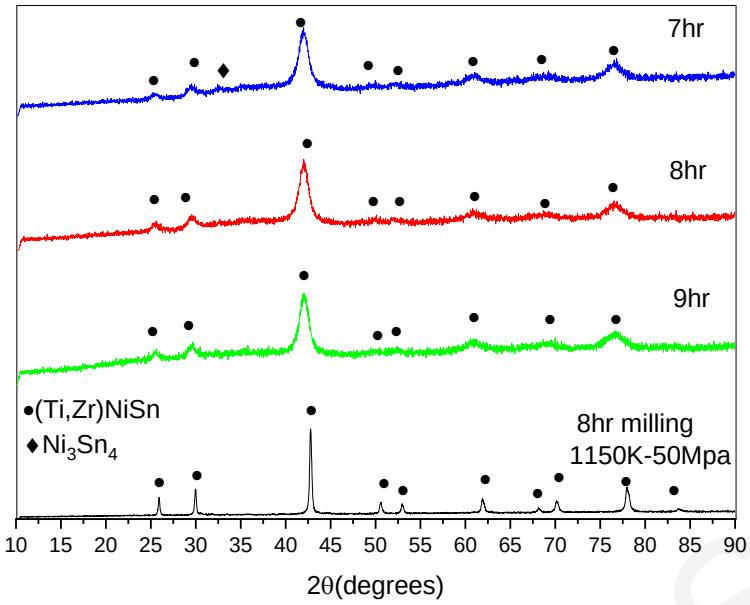

Figure 36: PXRD graph of milling time and sintering for the x=0.4.[101]

Table 3: Nominal composition, milling duration, minimum required milling time and sintering temperature.

Nominal Composition	Milling Duration(hrs)	Minimum required milling time (hrs)	Sintering Temperature(K)
$Ti_{0.6}Zr_{0.4}NiSn$	6-10	8	1150
$Ti_{0.5}Zr_{0.5}NiSn$	6-10	10	1100-1150
$Ti_{0.4}Zr_{0.6}NiSn$	6-10	7	1100-1150
$Ti_{0.3}Zr_{0.7}NiSn$	8-12	12	1100-1150
$Ti_{0.2}Zr_{0.8}NiSn$	8-12	9	1100-1150

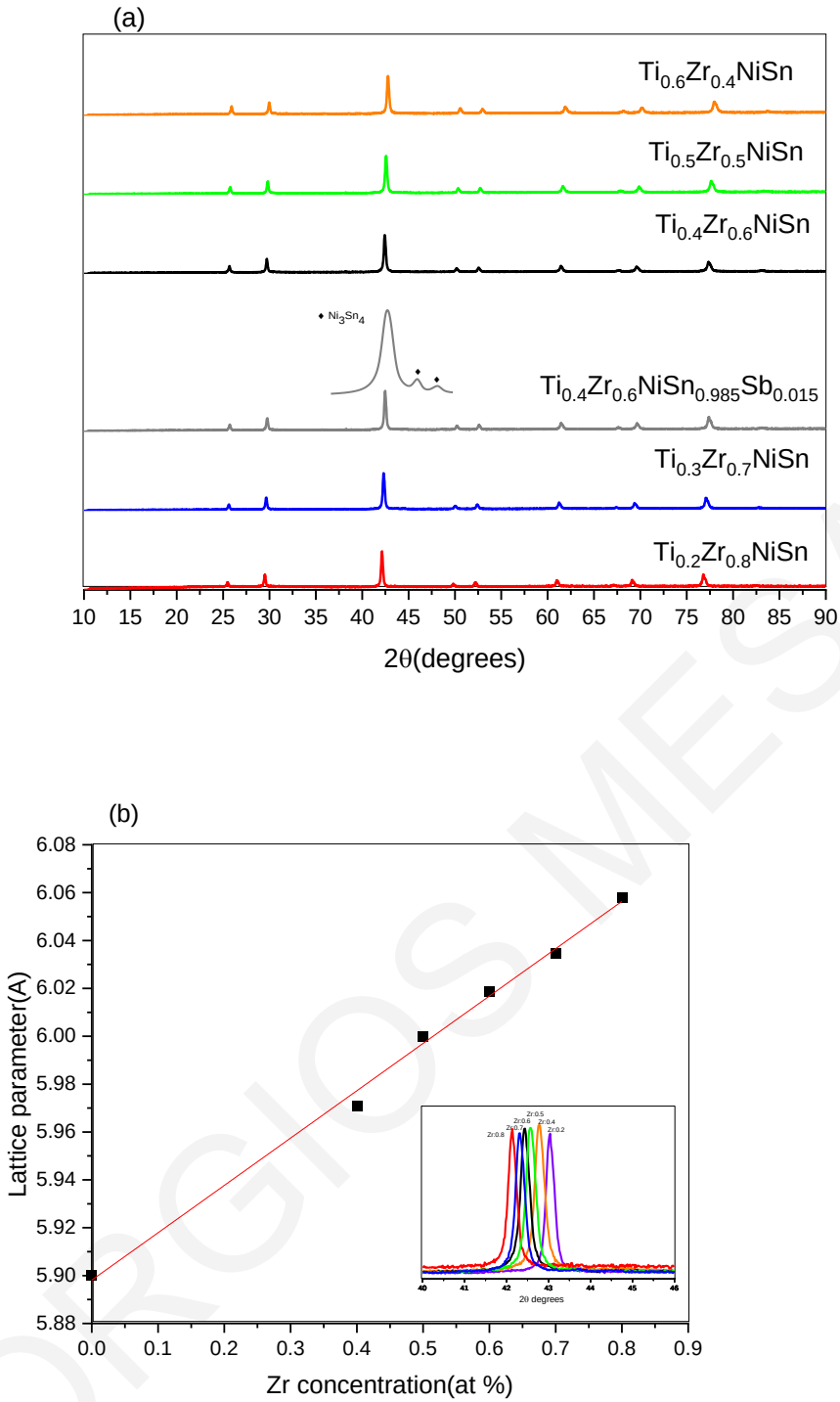

Figure 37: (a) PXRD graphs for the samples with Zr concentrations 0.4, 0.5, 0.6, 0.7 and 0.8 including doped y=0.015 for x=0.6; (b) Increase of the unit cell as percentage of Zr increases. [101]

4.2.2.2 Electron microscopy and elemental analysis

All samples exhibited a uniformity without any phase separation as observed in SEM images of the HP sintered pellets, in contrary to the end member TiNiSn (see, figure 38). A homogeneous morphology was observed, regardless the Zr concentration. This is in contrary to the arc melting synthesis, where similar compositions included Ti_6Sn_5, $ZrSn_2$ and Ni_3Sn_4 impurity phases in several cases.[108]

EDS results also support the single-phase microstructure of the products of MA synthesis, see Table IV. Clearly, all solid solution compositions were in good agreement with the nominals. Nevertheless, the dopant concentration (1-2%Sb) cannot be correctly detected, due to the overlap with Sn.

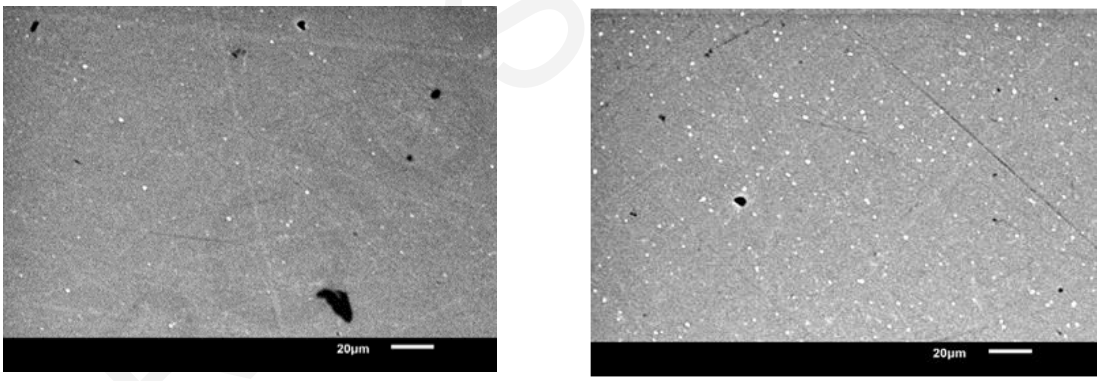

Figure 38: SEM images of $Ti_{0.4}Zr_{0.6}NiSn$ (left) and $Ti_{0.4}Zr_{0.6}NiSn_{1-y}Sb_y$ (y=0.015) [101]

Table 4: EDS results for undoped and doped $Ti_{0.4}Zr_{0.6}NiSn_{1-y}Sb_y$

Samples	Ti	Zr	Ni	Sn+Sb
Nominal composition	0.4	0.6	1	1
$Ti_{0.4}Zr_{0.6}NiSn$	0.44	0.63	0.95	0.99
$Ti_{0.4}Zr_{0.6}NiSn_{0.99}Sb_{0.01}$	0.43	0.64	0.92	1.01
$Ti_{0.4}Zr_{0.6}NiSn_{0.985}Sb_{0.015}$	0.43	0.63	0.92	1.02
$Ti_{0.4}Zr_{0.6}NiSn_{0.98}Sb_{0.02}$	0.43	0.62	0.93	1.02

The $Ti_{0.4}Zr_{0.6}NiSn_{1-y}Sb_y$ *(y=0.015)* composition was selected for further structural investigation as the best performing member of the series in terms of thermoelectric properties (see part 3.4.2). The detailed structural features were elucidated by transmission electron microscopy experiments (TEM/HRTEM), coupled with EDS analysis. Figure 39a shows a typical conventional TEM image of the $Ti_{0.4}Zr_{0.6}NiSn_{1-y}Sb_y$ *(y=0.015)* particles. These are typically small in size, about 100-150 nm on average, and single crystalline as revealed by the Selected Area Diffraction (SAD) pattern inset in Fig.39(a), the latter along [-113]. Measurements of the d spacings at the pattern resulted in a lattice constant of a_{SAD}=0.601 nm on average, being in very good agreement with the theoretical lattice parameter of $Ti_{0.4}Zr_{0.6}NiSn_{1-y}Sb_y$ *(y=0.015)*. The latter has been estimated using Vegard's law and the values of the two distinct members (i.e. TiNiSn (a=0.593 nm) and ZrNiSn (a=0.612 nm)) where $a_{theor.}$=0.604 nm was deducted. This is considered as a minimum value, as there would be an enlargement of the unit cell due to Sb incorporation.

In addition, the sample contains a substantial number of nanoparticles, as denoted by arrows in Figure 39a. The nanoparticles have a size range of up to 15 nm and are single crystalline, as well. In comparison with literature, our samples exhibit smaller particle sizes with average size between 100-150 nm and nanoparticles up to 15 nm. A typical one is shown at the HRTEM image of Figure 39a, slightly inclined from the [011] crystallographic direction of $Ti_{0.4}Zr_{0.6}NiSn_{1-y}Sb_y$ *(y=0.015)*, so that mainly {111} lattice fringes are dominant and some areas with (200) ones. Experimental measurements of their distance provided d_{200}=0.303 nm and d_{111}=0.35 nm, respectively; this results in a lattice constant of a=0.606 nm on average, which is in good agreement with both, the XRD results (a=0.601 nm) and the theoretical value $a_{theor.}$=0.604 nm. The slightly higher lattice constant found at Figure 39b could merely be a consequence of the Sb incorporation in the lattice.

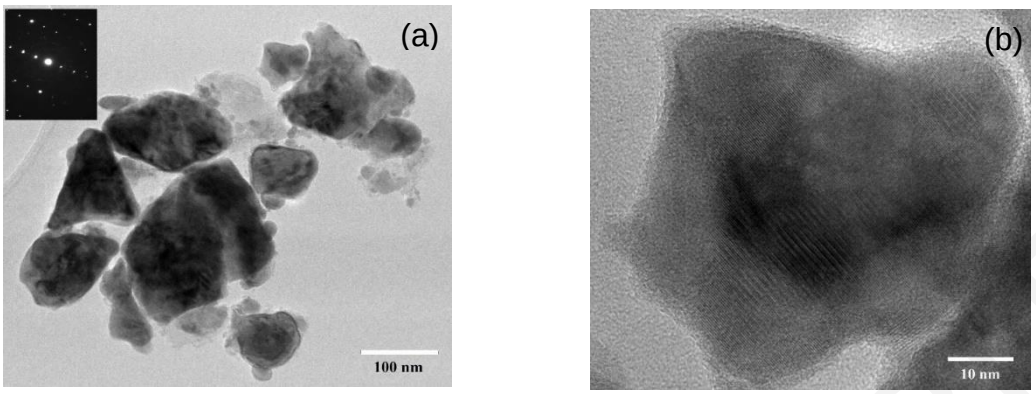

Figure 39: (a): Representative TEM image of the particles' morphology at the $Ti_{0.4}Zr_{0.6}NiSn_{1-y}Sb_y$ (y=0.015) sample, along with a SAD pattern inset, along [$\bar{1}$13]; (b) HRTEM image of a representative nanocrystalline particle, viewed a few degrees off its [011] crystallographic direction [101]

4.3 TE Properties of Ti-Zr system

4.3.1 Thermoelectric Properties of $Ti_{1-x}Zr_xNiSn$ series

The temperature dependence of thermoelectric properties of the samples with nominal stoichiometry of $Ti_{1-x}Zr_xNiSn$ (x=0,0.4, 0.5, 0.6, 0.7 and 0.8) are shown in Figure 40. The Seebeck coefficient was negative, confirming n-type semiconductors and, overall, increased in absolute values with the Zr concentration, see Figure 41. On the other hand, electrical conductivity decreased with the Zr concentration with majority of the samples ranging between 120-150 S/cm. The end member TiNiSn has the highest electrical conductivity and this can be attributed to the presence of the metallic full Heusler phase, as confirmed in part (4.2.1). The power factor ($S^2\sigma$) reaches to values >20 $\mu W/cm\cdot K^2$ and composition x= 0.6 seems very promising, considering it is an undoped member.

The room temperature thermal conductivity values of the end member TiNiSn is 4.26 W/m·K and significantly dropped with the Zr incorporation to the range of 2.5-3.5 W/m·K, see Table V. In order to evaluate the effect of Ti/Zr substitution to the phonon scattering, the lattice thermal conductivity (κ_{lat}) was estimated by subtracting the electronic contribution from the total ($\kappa_{lat}= \kappa- \kappa_{ele}$). The electronic thermal conductivity (κ_{ele}) was calculated using the Wiedemann -Frantz law ($\kappa_{ele} =L\cdot\sigma\cdot T$ where L is the Lorenz factor). The Lorenz factor was estimated from the measurements of the Seebeck coefficient assuming scattering from acoustic phonons.[109]

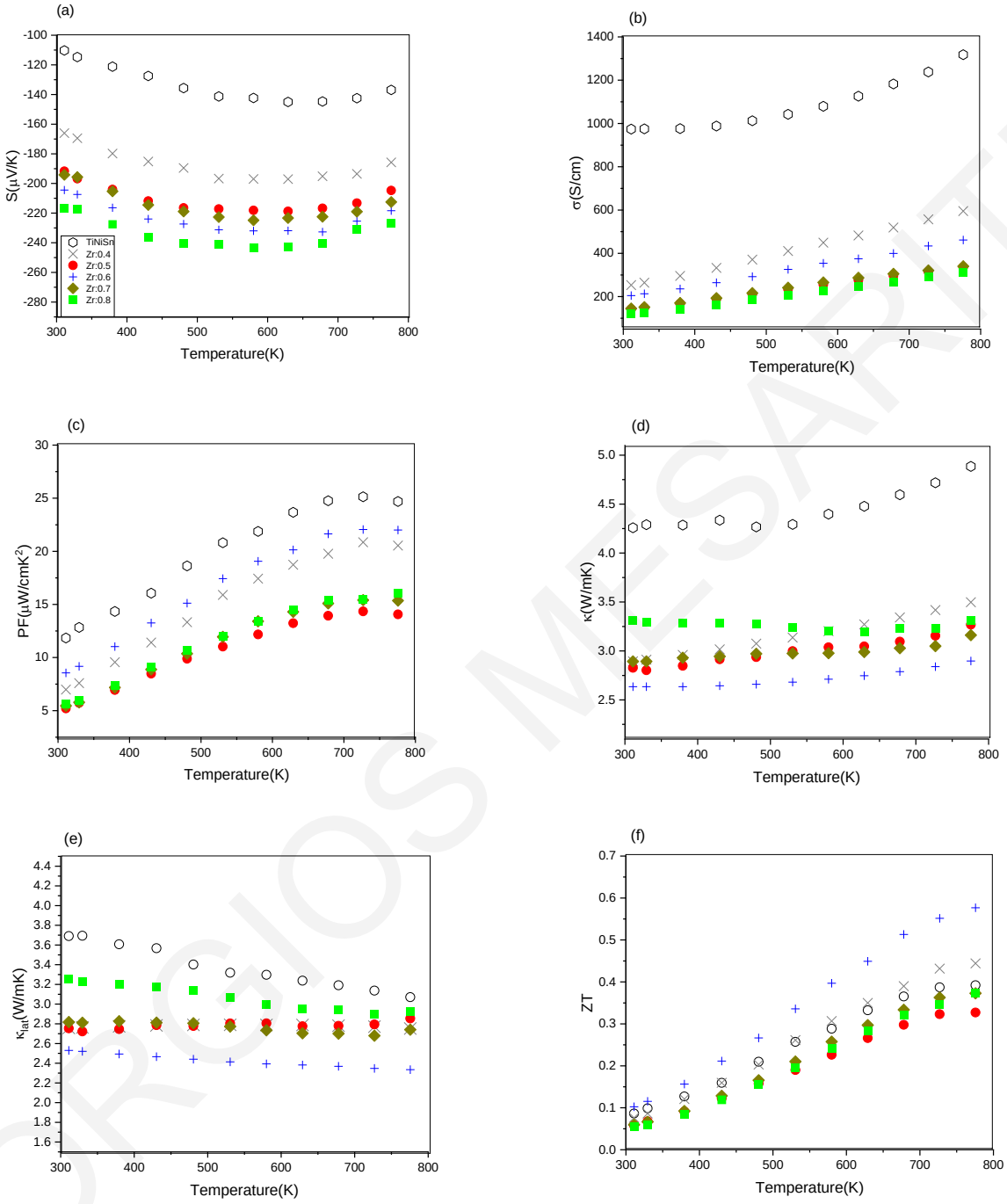

Figure 40: Thermoelectric properties of the $Ti_{1-x}Zr_xNiSn$ materials for x=0-0.80.[101]

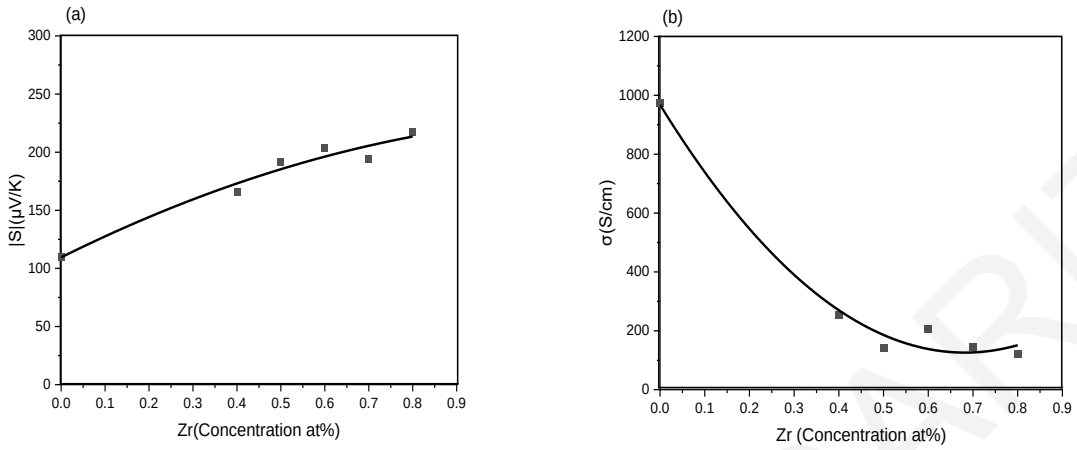

Figure 41: (a) Seebeck coefficient and (b) electrical conductivity of the $Ti_{1-x}Zr_xNiSn$ materials for x=0-0.80 vs Zr concentration.[101]

Table 5: Thermoelectric properties of the $Ti_{1-x}Zr_xNiSn$ samples at room temperature.

x	Method	σ (S/cm)	S (μV/K)	PF_{max} (μW/cmK^2)	κ (W/m·K)	κ_{lat} (W/m·K)	ZT max
0	MA+HP	974	-110	25	4.26	3.69	0.39
0.4	MA+HP	253	-166	21	2.89	2.76	0.44
0.5	MA+HP	142	-192	14	2.83	2.75	0.33
0.6	MA+HP	205	-204	22	2.63	2.53	0.58
0.7	MA+HP	145	-194	15	2.89	2.82	0.37
0.8	MA+HP	121	-217	16	3.31	3.25	0.37

Figure 42 presents the comparison between room temperature lattice thermal conductivity of our MA to the arc melted samples[108]. Samples prepared by arc-melting technique overall exhibit higher values of lattice thermal conductivity than those prepared with MA. According to the literature, several groups have tried to reduce the thermal conductivity of the arc-melted samples by subsequent ball-milling. Tritt et al. investigated the effect of the grain size on Sb-doped TiNiSn and reported that the lattice thermal conductivity generally decreases with decreasing average grain size, reaching the value of 3.7 W/m·K at room temperature for sizes of ~0.4μm[110]. Bahrami et. al reported a 40% reduction of lattice thermal conductivity for ZrNiSn obtained by extensive cryomilling (i.e. κ_{lat}~3W/m·K)[111]. The reduction in κ_{lat} was ascribed to the reduced grain size as well as the increased atomic disorder. Germond et al. reported a reduction of thermal conductivity from 11 W/m·K to 7 W/m·K for samples synthesized by mechanical alloying instead of arc melting[112]. In all cases, it is evident that the reduction in lattice conductivity is a result of the smaller grain size and increased number of grain boundaries per unit volume, causing increased phonon scattering.

Furthermore, all solid solutions present lower lattice thermal conductivity than end members regardless the preparation method due to the Ti/Zr mass fluctuation (Γm) and the induced strain (Γs). In order to examine the effect of alloying, we employed the Klemens model, adopting the algorithmic approach described in[113]. The Klemens model considers Umklapp and point-defect phonon scattering processes, and predicts the ratio of κ_{lat} for a solid solution to that of a hypothetical solid solution without mass or strain fluctuation (κ_0), as a function of a disorder parameter u:

$$\frac{\kappa_{lat}}{\kappa_0} = \frac{\tan^{-1} u}{u} \quad (24) \quad , \quad u^2 = \frac{(6\pi^5\Omega^2)^{\frac{1}{3}}}{2k_B Vs}\kappa_0 \cdot \Gamma \quad (25) \quad , \quad \Gamma = \frac{\langle \overline{\Delta M}^2 \rangle}{\langle \bar{M} \rangle^2} + \varepsilon \frac{\langle \overline{\Delta R}^2 \rangle}{\langle \bar{R} \rangle^2} \quad (26)$$

where, k_B is the Boltzmann constant, Ω is the average volume per atom, Vs is the average speed of sound, and the scattering parameter ($\Gamma=\Gamma m+\Gamma s$) is related to the average variance in atomic mass (Δm) and atomic radius (ΔR), with ε an adjustable parameter related to the Gruneisen parameter. For a given composition, the value of κ_0, Ω, and Vs are calculated as linear interpolation between the values for the end-members[113]. The results as well as the smooth variation of Γ_M and Γs are shown as lines and inset in Figure 42, respectively. It is clear that the mass fluctuation is a major mechanism to describe the composition dependence of the lattice thermal conductivity in $Ti_{1-x}Zr_xNiSn$. Moreover, strain (or force constant variance) is also required to model the lattice thermal conductivity at room temperature as shown in Figure 42. Interestingly, the lattice thermal conductivity for member x=0.6 is lower than expected based on this analysis, suggesting some additional phonon scattering, possibly via enhanced nanostructuring. Moreover, its lowest thermal conductivity lead to the significantly highest ZT (see Figure 40f), therefore, this member was selected for further doping studies.

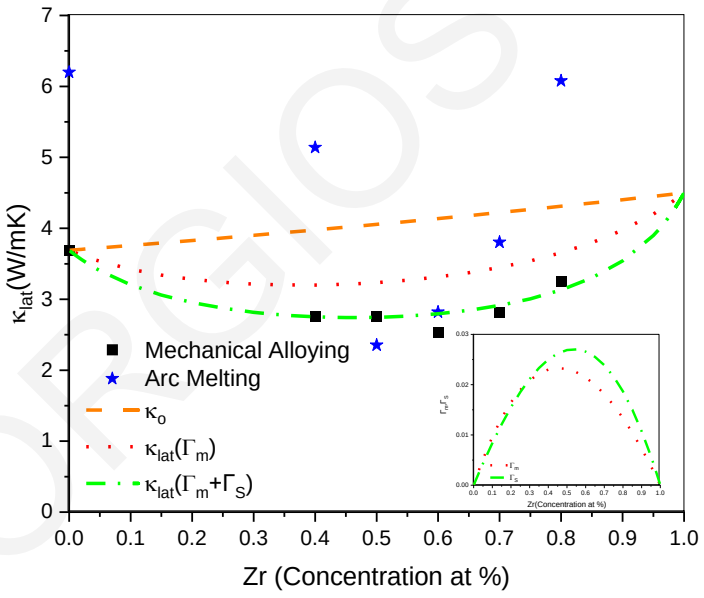

Figure 42: Lattice thermal conductivity of MA samples and arc melting (lattice thermal conductivity for samples prepared by arc melting was estimated using reported Seebeck coefficient and electrical conductivity in) vs Zr concentration. The lines correspond to the calculated values considering the Ti/Zr mass fluctuation (Γm) and the induced strain (Γs) (inset: Γm and Γs ve stoichiometry [101]

4.3.2 Thermoelectric Properties of Sb-doped $Ti_{0.4}Zr_{0.6}NiSn$

Member $Ti_{0.4}Zr_{0.6}NiSn$ exhibited the lowest lattice thermal conductivity of the series and highest ZT, therefore, it was selected for further doping investigation. Sb was selected as dopant and the series $Ti_{0.4}Zr_{0.6}NiSn_{1-y}Sb_y$ (y=0, 0.01, 0.015 and 0.02) was prepared and studied.

The room temperature Seebeck coefficient decreased (in absolute values) from - 240 μV/K (undoped sample) to -75 μV/K for the sample with y=0.02, indicating the increase of carrier concentration due to Sn/Sb substitution see Table VI. On the other hand, the electrical conductivity increased with Sb incorporation, as expected, due to the higher carrier concentration. The higher carrier concentration also affected the temperature dependence of the Seebeck coefficient and electrical conductivity, as expected, showing a degenerate semiconductor behaviour[114], see Figure 43. The maximum power factor was 32 $\mu W/cmK^2$ for y=0.015 and dropped to 25 $\mu W/cmK^2$ for y=0.02, suggesting that Sb concentration of y>0.015 exceeded the optimum carrier concentration for this series. The thermal conductivity increased with dopant concentration mainly due to the higher electrical conductivity. Overall, a maximum figure of merit up to 0.71 at 800K was achieved.

The Seebeck coefficient and electrical conductivity of the best stoichiometry of this work, named $Ti_{0.4}Zr_{0.6}NiSn_{0.985}Sb_{0.015}$, were further measured upon heating/cooling to evaluate their stability, see Figure 44. It is clear that the properties remained the same for all cycles and these results particularly encourage further investigations of MA, as a promising synthesis method.

Table 6: Thermoelectric Properties of doped samples $Ti_{0.4}Zr_{0.6}NiSn_{1-y}Sb_y$ at 300K**.**

y	σ (S/cm)	S (μV/K)	PF_{max} ($\mu W/cm\cdot K^2$)	κ (W/m·K)	κ_{lat} (W/m·K)	ZT max
0.00	205	-204	22	2.63	2.53	0.58
0.01	1062	-106	18	3.03	2.40	0.41
0.015	1681	-112	32	3.42	2.43	0,71
0.02	2458	-75	25	4.02	2.42	0.42

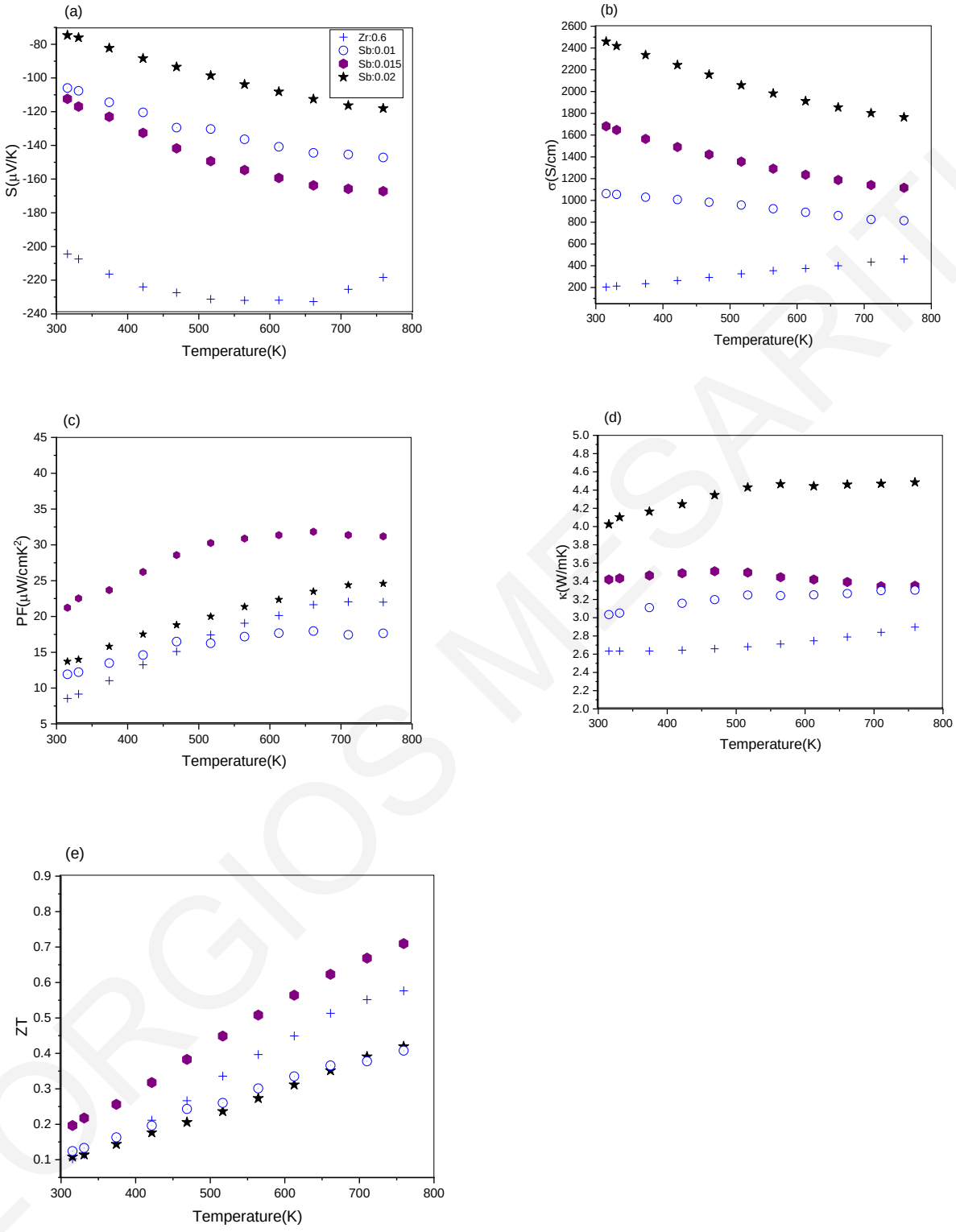

Figure 43: Thermoelectric Properties of doped $Ti_{0.4}Zr_{0.6}NiSn_{1-y}Sb_y$ samples.[101]

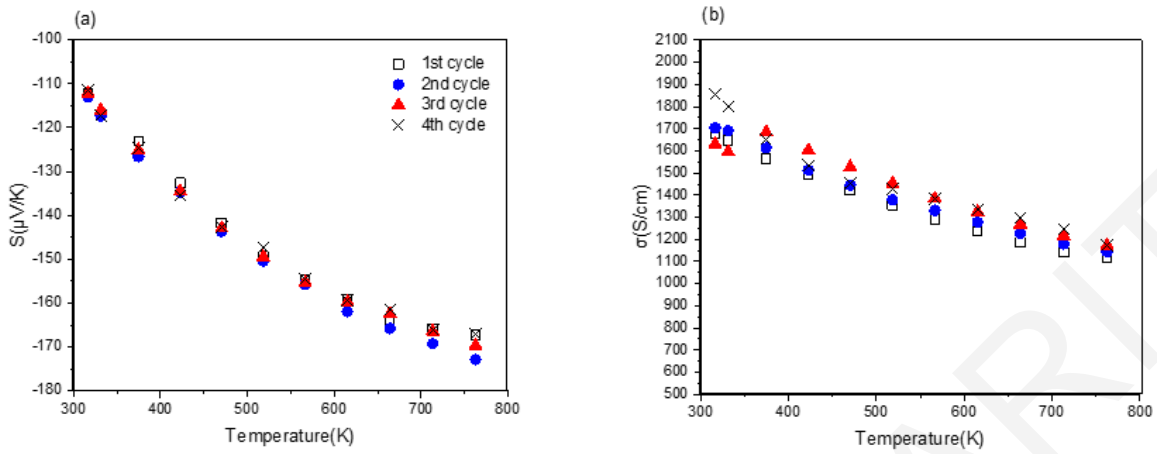

Figure 44: (a) Seebeck coefficient and (b) electrical conductivity for the $Ti_{0.4}Zr_{0.6}NiSn_{0.985}Sb_{0.015}$ sample measured upon heating/cooling.[101]

4.4 Thermal Annealing and Stability

The practical applications of TEGs involve prolonged and large temperature gradients. For that reason, it is significantly important to investigate the thermal stability of the individual materials in order to find use in practical devices. The annealing process is commonly used in both n- and p-type arc-melted ingots before and after sintering to promote the crystalline order and to eliminate impurity phases such as $(Hf,Zr)_5Sn_3$, $TiNi_2Sn$, Ti_6Sn_5, and unalloyed Sn. The annealing process can be prolonged up to 7 days at temperatures around 1073K for the arc melting samples. Krez et al, studied the long-term stability of the n-type $Ti_{0.3}Zr_{0.35}Hf_{0.35}NiSn$ (ZT=0.6)[115]. The properties remained unaffected after 500 cycles of repeated heating and cooling from 373K to 873K while the phase-separation was stable under long-term cycling.

This additional treatment is not necessary for the mechanically alloyed solid solutions because it is quite simple to prepare single-phase HH material via a single step of milling. However, the effect of heating on the MA materials can give information for

(a) the stability of the thermoelectric properties in temperatures of modules operation (via annealing at 773K).

The ternary phase diagram of the n-type (Hf/Ti/Zr)NiSn is presented in figure 45 in order to get better knowledge regarding the phase stability and solid solution formation of HH materials[116]. A. Page et al., predict a miscibility gap at low temperatures between a Ti-rich and a Ti-poor half-Heusler phase. The miscibility gap eliminated at temperatures above 850 K[116].

(b) the phase evaluation of MA materials (via annealing at 1073K)

Thus, at high annealing temperatures (e.g 1073K) the equilibrium phase could be a solid solution and the interdiffusion among the elements Ti/Zr/Hf will be insignificant. Therefore, the commonly observed dendritic features in n-type HH materials synthesized by arc-melting are developed during the rapid solidification process and should remain unaffected after annealing[116]. It is obvious that the observed microstructures and solubility limits of the HH phases are highly dependent on synthesis techniques.

(a) Annealing at 773K.

A sample annealed in 773K was investigated for stability and it is presented with annealing sample at 1073K for comparison. At 773K the sample seems to be stable.

(b)Annealing at 1073K

Based on that, the effect of thermal annealing under different durations times (1 day,3 days,6 days and 10 days at 1073K) upon thermoelectric performance of a n-type HH solid solution prepared via MA was investigated and correlated with the impact on the structural

properties. Our best composition $Ti_{0.4}Zr_{0.6}NiSn_{0.985}Sb_{0.015}$ with figure of merit 0.71 was selected in order to eliminate the metallic phase Ni_3Sn_4 and to examine if could be exist a phase-separation for further reduction in the lattice thermal conductivity and enhancement of the TE performance. The samples were synthesized and sintered as described in chapters 3 and 4. The sintered pellets were loaded into quartz-sealed tubes and annealed under vacuum.

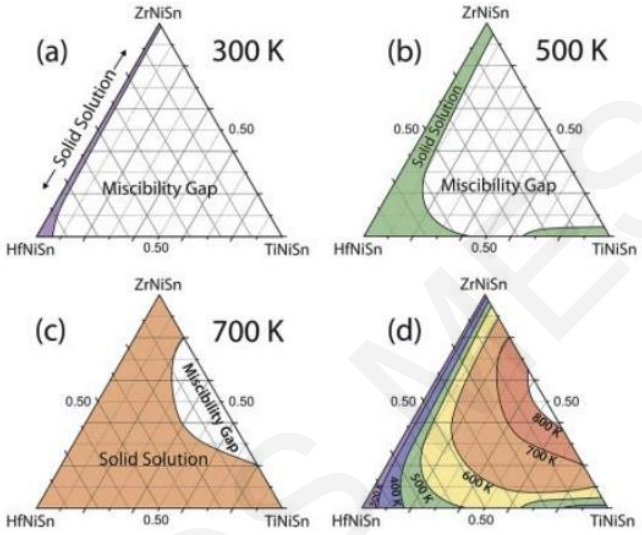

Figure 45: Ternary phase diagram of (Hf,Zr,Ti)NiSn.[116]

Figure 46 illustrates the powder x-ray diffraction patterns of the best $Ti_{0.4}Zr_{0.6}NiSn_{0.985}Sb_{0.015}$ samples and the annealing time at 1073K. It is obvious at 1 and 2 days of annealing the formation of a single-phase material and the decrease of the Ni_3Sn_4 phase as expected. After 3 days of annealing the materials are sensitive to the formation of full Heusler phase and decomposition occur with secondary phases such as Ni_3Sn_4.

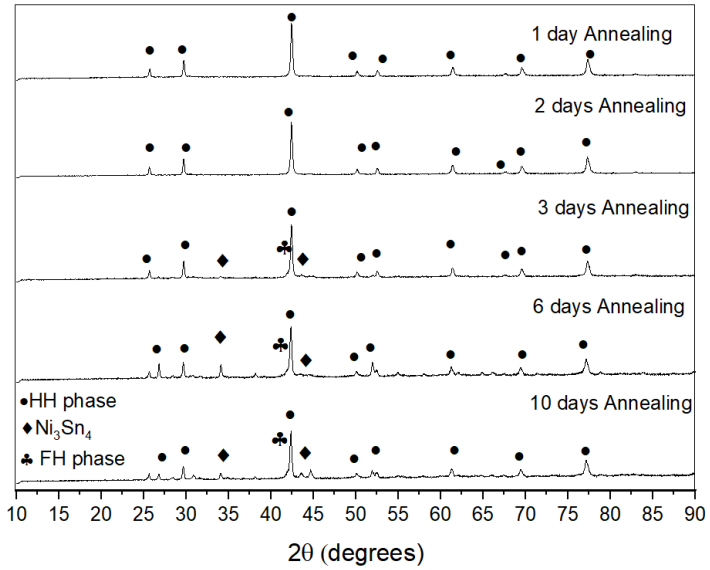

Figure 46: PXRD patterns of the annealed samples at 1073K.

SEM images and EDX results are presented in figure 47 and table VII respectively. For the samples with 1, 2 days at 1073K and 5 days of annealing at 773K is exhibited a uniformity without any phase separation as observed in SEM images, in contrary to the samples for 3 days,6 days and 10 days of annealing.

Annealing 1 day

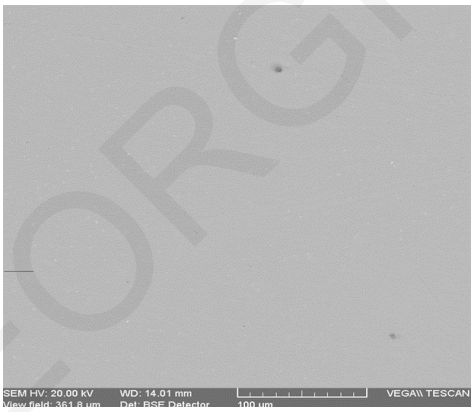

Annealing 2 days

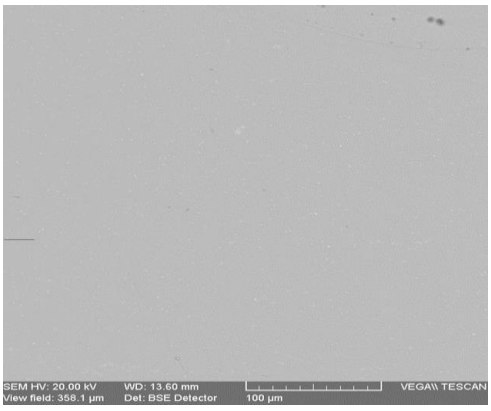

Annealing 3 days

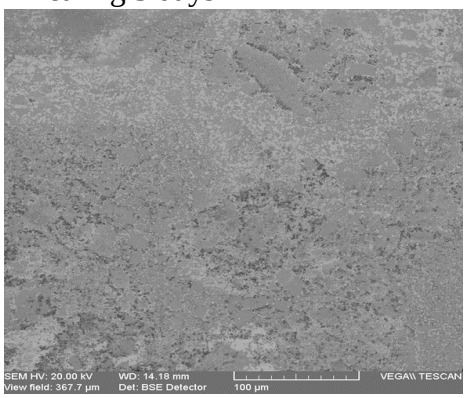

Annealing 6 days

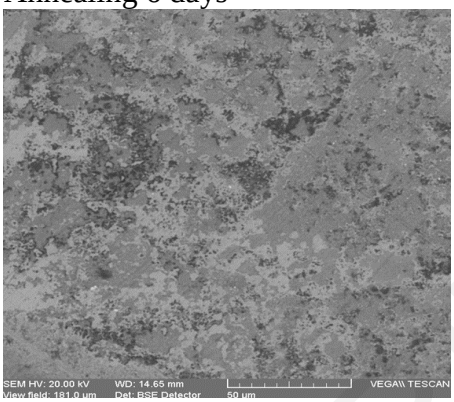

Annealing 10 days

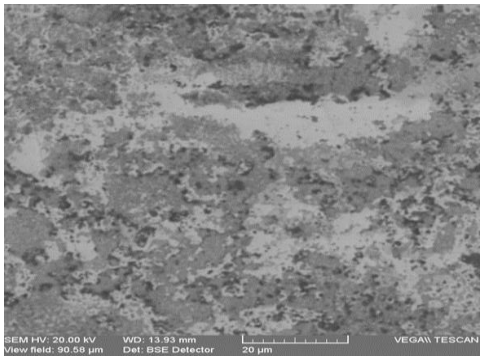

Annealing 5 days at 773K

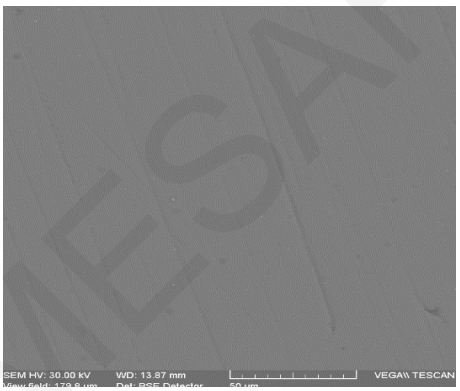

Figure 47: SEM images of annealed samples

Table 7: EDS results of the annealed samples

Sample	Ti	Zr	Ni	Sn	Sb
Annealed 1 day	0.39	0.62	1.04	0.91	0.04
Annealed 2 day	0.4	0.62	1.04	0.91	0.025
Annealed 3 day (Matrix)	0.41	0.87	0.91	0.80	0.011
Black area	0.24	0.38	0.42	1.92	0.04
Dark Gray area	0.79	1.19	0.55	0.45	0.007
Gray area	0.34	0.36	1.31	0.97	0.025
Annealed 6 day (Matrix)	0.53	0.92	0.79	0.75	0.01
Black area	0.42	0.95	0.52	1.09	0.01
Dark Gray area	0.26	0.32	0.20	2.21	0.016
Gray area	0.20	0.46	1.35	0.98	0.02
Annealed 10 day (Matrix)	0.56	0.99	0.76	0.68	0.012
Black area	0.21	0.38	0.36	2.02	0.03
Dark Gray area	0.43	1.18	0.33	1.03	0.023
Gray area	0.09	0.27	1.62	1.01	0.001
Annealed 5 days at 500°C	0.402	0.578	1.058	0.945	0.016

The thermoelectric properties of the annealed samples are presented in Figure 48. For the samples which are annealed for 3 ,6 and 10 days are failed and crack this is due to the phase separation. The samples which are annealed for 1 and 2 days at 1073K as well as the sample of annealing at 773K are exhibit higher electrical conductivity compared to the unannealed sample and this is owing from the growth of grains inside the material. The Seebeck coefficient remains the same for all samples. The increase to the electrical conductivity results to the enhancement of the power factor and the total thermal conductivity. The figure of merit is enhanced for 1 day of annealing and reached the value of 0.83.

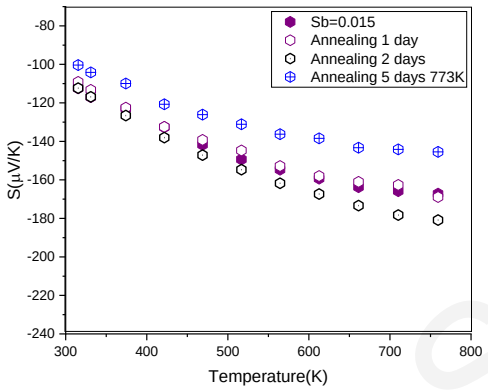

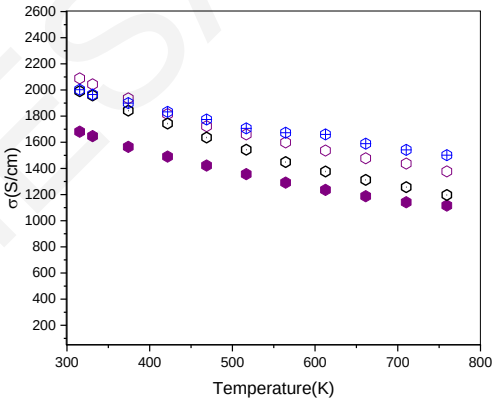

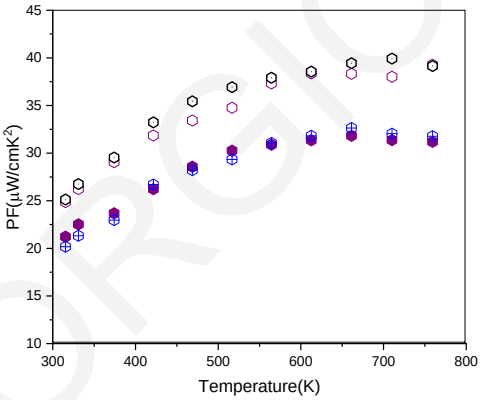

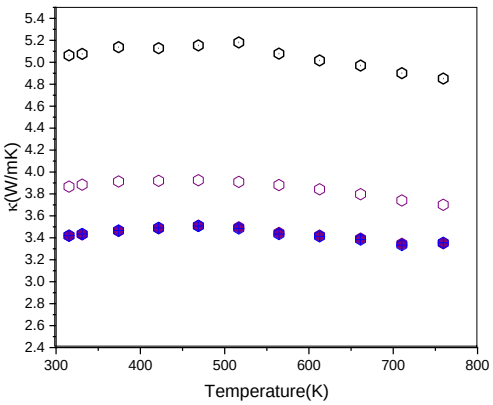

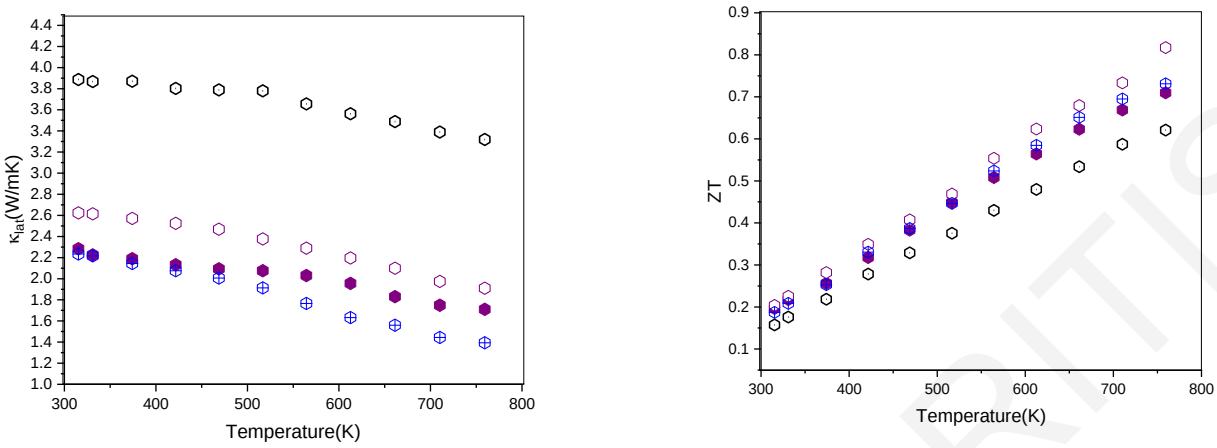

Figure 48: Thermoelectric Properties of annealed samples.

4.5 Modification of the best stoichiometry with Ni excess $Ti_{0.4}Zr_{0.6}Ni_{1+x}Sn$

The grain boundary engineering approach is another useful strategy to increase the carrier concentrations, except from optimization through doping, is to use the grain boundary. Makongo et al, argues in his work that the creation of Full Heusler phase in the grain boundaries between the Half Heusler phase enhanced the Seebeck coefficient without reduction of the electrical conductivity[67]. The creation of Full Heusler nanoinclusions can filter out low energy carriers and keep the high mobility of the remaining charge carriers.In this part we modify our best undoped composition $Ti_{0.4}Zr_{0.6}NiSn$ in order to create full Heusler in nanoscale through MA. The synthesis procedure was the same with previous and interestingly with extra Ni the milling time was increased from 7 hrs to 10 hrs to gain a single HH phase.

Figure 49 shows the powder x-ray diffraction patterns of the Ni excess $Ti_{0.4}Zr_{0.6}Ni_{1+x}Sn$ samples. Although the formation of FH was the aim of this series, it is obvious that additional nickel leads to the formation of the Ni_3Sn_4 metallic phase. SEM images and EDX results are presented in figure 50 and table VIII respectively. For the samples is exhibited a uniformity without any phase separation as observed in SEM images.

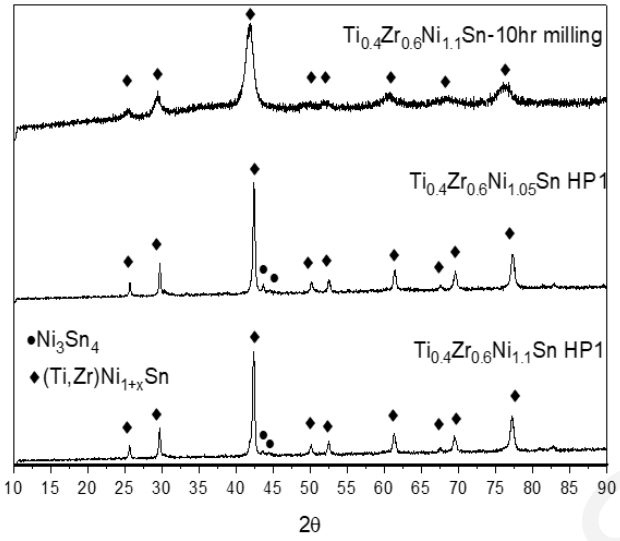

Figure 49: PXRD pattern of the Ni excess samples.

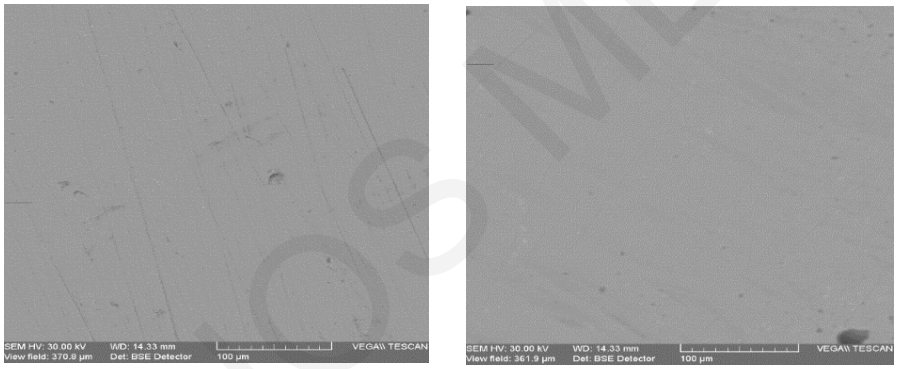

Figure 50: SEM images of the $Ti_{0.4}Zr_{0.6}Ni_{1.05}Sn$(right) and $Ti_{0.4}Zr_{0.6}Ni_{1.1}Sn$.

Table 8: EDS results of the Ni excess samples.

Samples	Ti	Zr	Ni	Sn
$Ti_{0.4}Zr_{0.6}NiSn$	0.44	0.63	0.95	0.99
$Ti_{0.4}Zr_{0.6}Ni_{1.05}Sn$	0.38	0.63	1.08	0.91
$Ti_{0.4}Zr_{0.6}Ni_{1.1}Sn$	0.38	0.61	1.11	0.90

Member $Ti_{0.4}Zr_{0.6}NiSn$ exhibited the lowest lattice thermal conductivity of the series and highest ZT, therefore, it was selected for further investigation see figure 51. Ni excess was selected as dopant and the series $Ti_{0.4}Zr_{0.6}Ni_{1+x}Sn$ (x = 0,0.05 and 0.1 was prepared and studied. The room temperature Seebeck coefficient decreased (in absolute values) from − 240 μV / K to − 76 μ V / K for the sample with x = 0.1, indicating the increase of carrier concentration. On the other hand, the electrical conductivity increased with Ni incorporation, as expected, due to the existence of the metallic phase. The maximum power factor was 22 μW /cm K^2 for x = 0 and dropped to 9 μW /cm K^2 for x = 0.1, due to the increase of the thermal conductivity. The thermal conductivity increased with Ni concentration mainly due to the higher electrical conductivity. Overall, the maximum figure of merit up to 0.58 at 800 K was achieved for the sample without Ni excess.

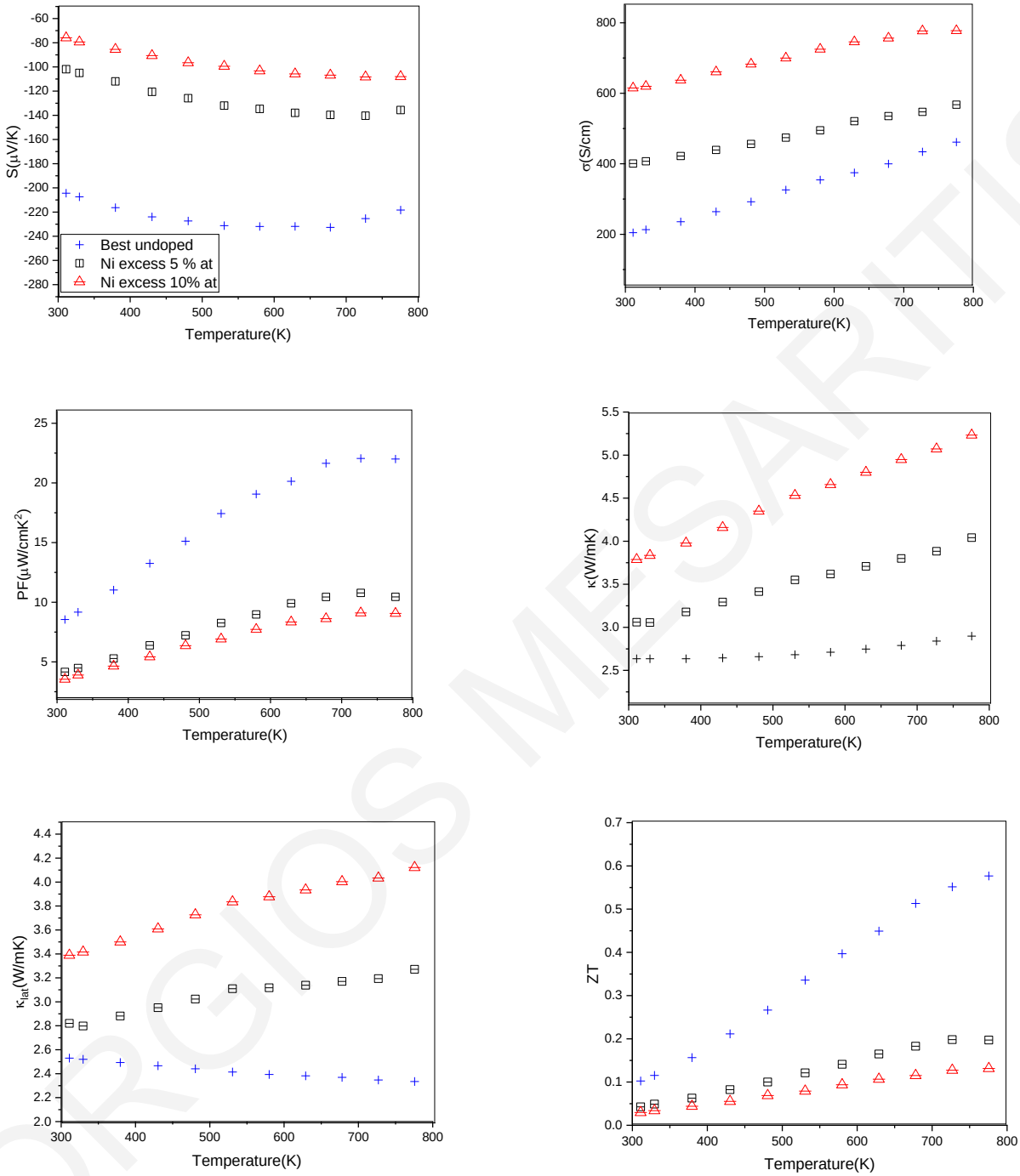

Figure 51: Thermoelectric Properties of the Ni excess samples.

4.6 Conclusions

The synthesis of n-type (Zr,Ti)NiSn materials via mechanical alloying and sintering was successfully attempted for the first time. The undoped solid solutions exhibited single half Heusler phase, however, the incorporation of Sb as dopant resulted in small amount of the Ni_3Sn_4 binary phase. The thermoelectric properties of the solid solution series were affected by the Ti/Zr substitution with emphasis on the lattice thermal conductivity where the mass fluctuation had the main effect. Moreover, nanostructuring, grain size reduction and strain caused by the mechanical alloying also contributed to the phonon scattering as additional mechanism. The best figure of merit for the series was 0.71 at 773 K for the member $Ti_{0.4}Zr_{0.6}NiSn_{0.985}Sb_{0.015}$, being promising for further studies in this method. The addition of extra Nickel in our best composition $Ti_{0.4}Zr_{0.6}Ni_{1+x}Sn$ in order to optimize the TE properties seems to create metallic phase Ni_3Sn_4 as a result the reduction of the figure of merit. First results show that the materials are stable for the temperature of potential operation of a device. Furthermore, annealing at higher temperature show that short heating could be beneficial for the properties of the materials, however, longer heating time result in phase separation and should be avoided. Overall, the synthesis of n-type Ti/Zr half Heusler via MA is feasible and seems very promising as a simple preparation method where one MA step substitutes several re-melting, annealing, and milling steps.

Chapter 5

5.n-type HH Ti-Hf and Ti-Zr-Hf

In this chapter, we continued our efforts on the synthesis of n-type half Heusler solid solutions via MA and studied the effect of Hf incorporation in the $Ti_{1-x}Hf_xNiSn$ and $(Ti_{0.4}, Zr_{0.6})_{1-x}Hf_xNiSn$ lattices. Based on the previous encouraging results of MA, $Ti_{1-x}Hf_xNiSn$ (with x=0.2,0.4,0.5,0.6,0.7 and 0.8) and $(Ti_{0.4},Zr_{0.6})_{1-y}Hf_yNiSn$ with (y=0, 0.1, 0.25, 0.3, 0.4, 0.5) samples were prepared to investigate the effect of isoelectronic Hf substitution as well as doping with Sb.

5.1 Synthesis of HH materials

Starting synthesis conditions were selected based on our previous work[101] where n-type half Heuslers were synthesized for the first time via MA to investigate the thermoelectric properties. The starting materials were high-purity elemental powders of Ti (99.99% Alfa Johnson Matthey Gmbh, Kandel, Germany), Hf (99.6% Alfa Johnson Matthey Gmbh, Kandel, Germany), Zr (99% US Research Nanomaterials Inc., Houston, TX, USA), Ni (99.99% Sigma Aldrich Merck, Darmstadt, Germany), Sn (99.85% Alfa Johnson Matthey GmbH, Kandel, Germany) and Sb (99.9% Alfa Johnson Matthey GmbH, Kandel, Germany). The powders were weighed according to the nominal compositions $Ti_{1-x}Hf_xNiSn$ (with x=0.2, 0.4, 0.5, 0.6, 0.7 and 0.8), Sb-doped $Ti_{0.4}Hf_{0.6}NiSn$ (with y:0, 0.1, 0.25, 0.3, 0.4, 0.5), and Sb-doped $(Ti_{0.4}Zr_{0.6})_{0.7}Hf_{0.3}NiSn$ with 1%, 1.5%, 2% and 2.5% Sb substitution in Sn site) in a tungsten carbide ball milling vial with a ball-to- material ratio of 10:1. The elemental powders were milled under Ar at speeds of 600rpm using a planetary ball mill (Pulverisette 7 Fritsch,Idar Oberstein,Germany). In our previous work [101], the duration of MA to synthesize $Ti_{1-x}Zr_xNiSn$ series was 7 to 12 hours and sintering at 1150K under 50MPa. In this work, MA duration between 6-12 hours was applied for $Ti_{1-x}Hf_xNiSn$ and $(Ti_{0.4}Zr_{0.6})_{1-y}Hf_yNiSn$ series and the products were studied by PXRD and SEM/EDS analysis. The same synthesis route was applied in all members and the selected compositions are also presented in Figure 52.

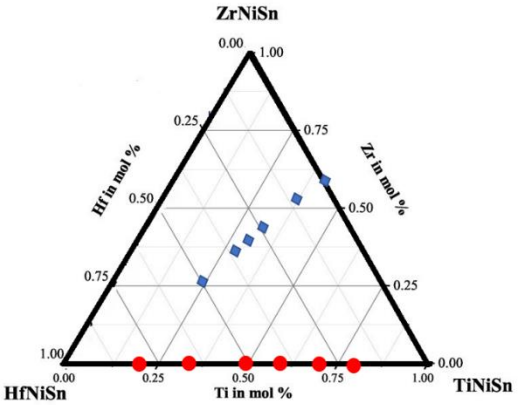

Figure 52: Concentration diagram of selected compositions.

5.2 Structure of Ti-Hf and Ti-Zr-Hf

5.2.1 Powder x-ray Diffraction

Figure 53a and 53b presents the patterns for members x=0.6 and y=0.3, respectively. In the case of the $Ti_{1-x}Hf_xNiSn$ series it is clear that all peaks could be well indexed to the cubic MgAgAs-type crystal structure at MA of 6 hours without any residual starting elements or other secondary phases. Furthermore, the incorporation of Hf in the $(Ti_{0.4}Zr_{0.6})_{1-y}Hf_yNiSn$ lattice increased the required MA duration from 7 hrs [101] to 9hrs for all compositions to avoid the existence of secondary Ni_3Sn_4 phase. Therefore, powders after MA of 6 hours and 9 hours for $Ti_{1-x}Hf_xNiSn$ and $(Ti_{0.4}Zr_{0.6})_{1-y}Hf_yNiSn$ series, respectively, were hot pressed and further investigated.

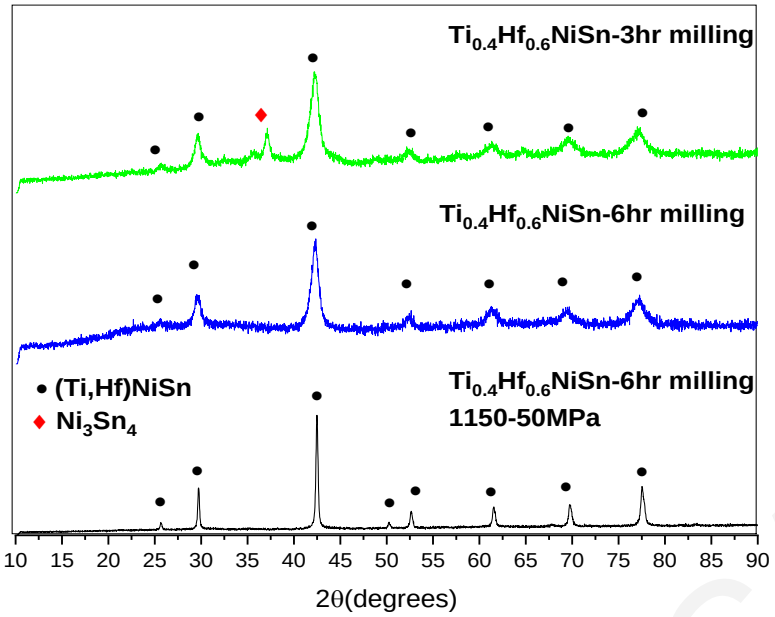

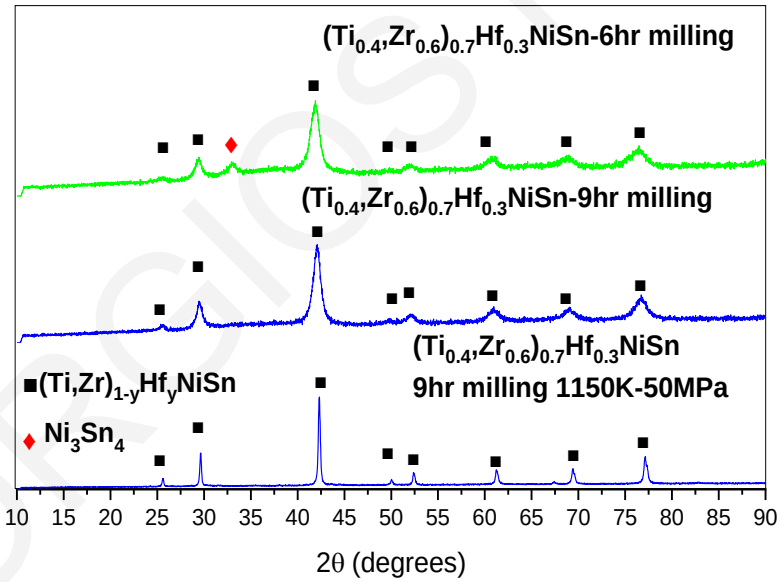

Figure 53: (a) PXRD pattern for the synthesis of $Ti_{0.4}Hf_{0.6}NiSn$. (b) PXRD pattern of the synthesis of $(Ti_{0.4},Zr_{0.6})_{0.7}Hf_{0.3}NiSn$.

Hot press (HP) sintering was carried out at 1150K under 50MPa to develop high quality pressed pellets. PXRD showed that only sharp peaks of $Ti_{1-x}Hf_xNiSn$ and $(Ti_{0.4}Zr_{0.6})_{1-y}Hf_yNiSn$ phases existed, except for the $Ti_{0.8}Hf_{0.2}NiSn$ sample where metallic full Heusler phase was also observed (Figure 54). All remaining patterns were identical without any significant change in terms of existing peaks and relative intensities; however, the peaks were shifted due to the Ti/Hf and Hf/Zr substitution, as expected, (see figure 54). Figure 55 shows the increase in the unit cell with Hf concentration for both compositions following Vegard's law with the lattice parameters being in good agreement with the literature [108]. The PXRD patterns of the Sb-doped members showed also single phase materials without any creation of binary phase Ni_3Sn_4 that is common impurity elsewhere [101]. The main peak is also displayed as inset to better clarify the presence (or not) of secondary phases in figure 54 a,b.

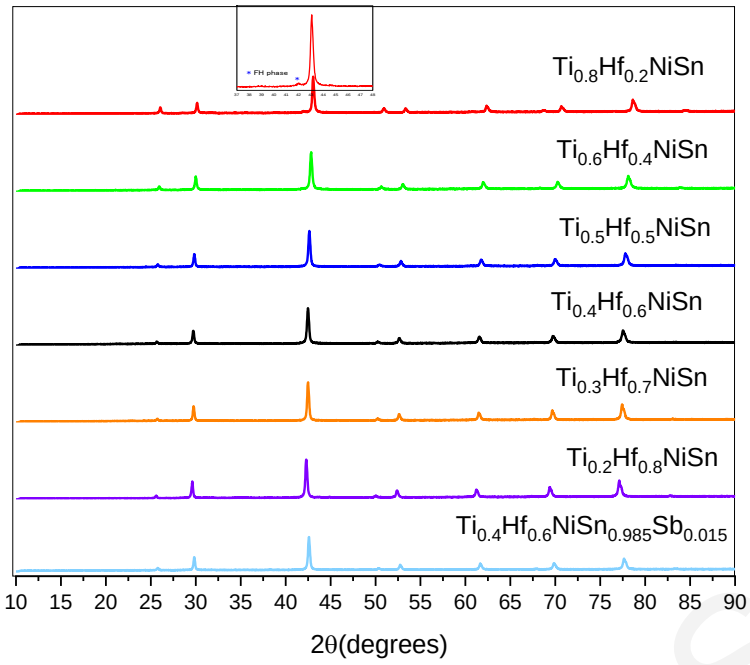

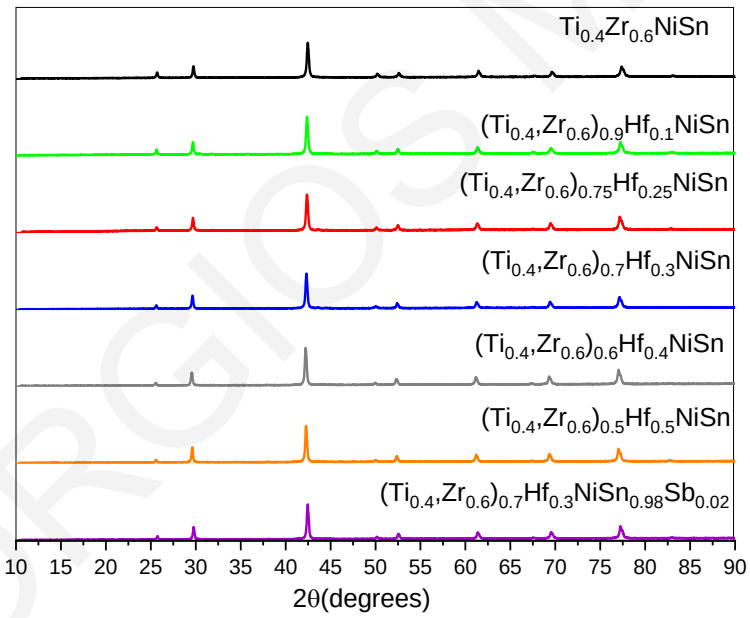

Figure 54: (a) PXRD patterns for the sintered pellets $Ti_{1-x}Hf_xNiSn$. (b)PXRD patterns for the sintered pellets of $(Ti_{0.4}, Zr_{0.6})_{1-y}Hf_yNiSn$.

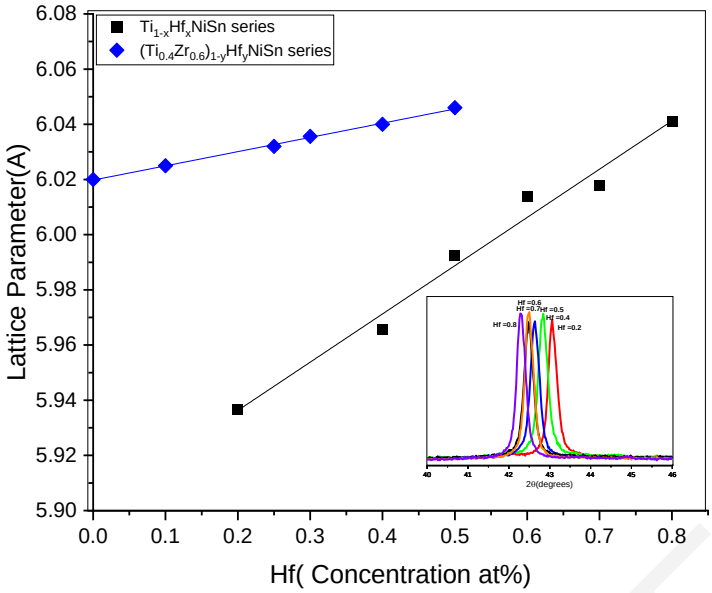

Figure 55: Increase of unit cell for the $Ti_{1-x}Hf_xNiSn$ samples and the (Ti0.4,Zr0.6)1-yHfyNiSn samples.

5.2.2 Electron microscopy and elemental analysis

Backscattered SEM images and EDS results confirmed that the pellets were single phase and according to the nominal composition, see figure 56 and Table IX and X. These results are in contrast with arc melting synthesis of similar compositions, where impurity phases like Ti_6Sn_5, $ZrSn_2$ and Ni_3Sn_4 are included in the final pellets[108]. *A. Page et al*, calculated the (Hf, Zr,Ti)NiSn thermodynamic phase diagram and suggested the coexistence of Ti-rich and Ti-poor grains for arc melted samples as non-equilibrium states created during solidification and kinetically trapped at lower temperatures[116].The solid solubility limit of these diverse systems depends on the synthesis technique; thus, the mechanism of solid solutions in MA is different compared to arc melting. Along with that, the solid solutions are formed in full composition range in the Cu-Fe, AlSb-InSb and Cu-Co systems via MA, but this is not in case for arc melting, which is rapid solidification process (RSP)[69].

Table 9: EDS analysis of the Sb doped $Ti_{0.4}Hf_{0.6}NiSn$ samples.

Samples	Ti	Hf	Ni	Sn+Sb
Nominal composition				
$Ti_{0.4}Hf_{0.6}NiSn$	0.39	0.52	1.12	0.97
$Ti_{0.4}Hf_{0.6}NiSn_{0.99}Sb_{0.01}$	0.39	0.51	1.13	0.97
$Ti_{0.4}Hf_{0.6}NiSn_{0.985}Sb_{0.015}$	0.40	0.52	1.13	0.95
$Ti_{0.4}Hf_{0.6}NiSn_{0.98}Sb_{0.02}$	0.41	0.53	1.13	0.93

Table 10: EDS analysis of the Sb doped $(Ti_{0.4},Zr_{0.6})_{0.7}Hf_{0.3}NiSn$ samples.

Samples	Ti	Zr	Hf	Ni	Sn+Sb
Nominal composition					
$(Ti_{0.4}, Zr_{0.6})_{0.7}Hf_{0.3}NiSn$	0.31	0.46	0.29	0.99	0.96
$(Ti_{0.4}, Zr_{0.6})_{0.7}Hf_{0.3}NiSn_{0.99}Sb_{0.01}$	0.29	0.44	0.29	0.99	0.99
$(Ti_{0.4}, Zr_{0.6})_{0.7}Hf_{0.3}NiSn_{0.985}Sb_{0.015}$	0.29	0.45	0.29	0.99	0.92
$(Ti_{0.4}, Zr_{0.6})_{0.7}Hf_{0.3}NiSn_{0.98}Sb_{0.02}$	0.28	0.45	0.30	0.98	0.93
$(Ti_{0.4}, Zr_{0.6})_{0.7}Hf_{0.3}NiSn_{0.975}Sb_{0.025}$	0.30	0.45	0.29	0.98	0.99

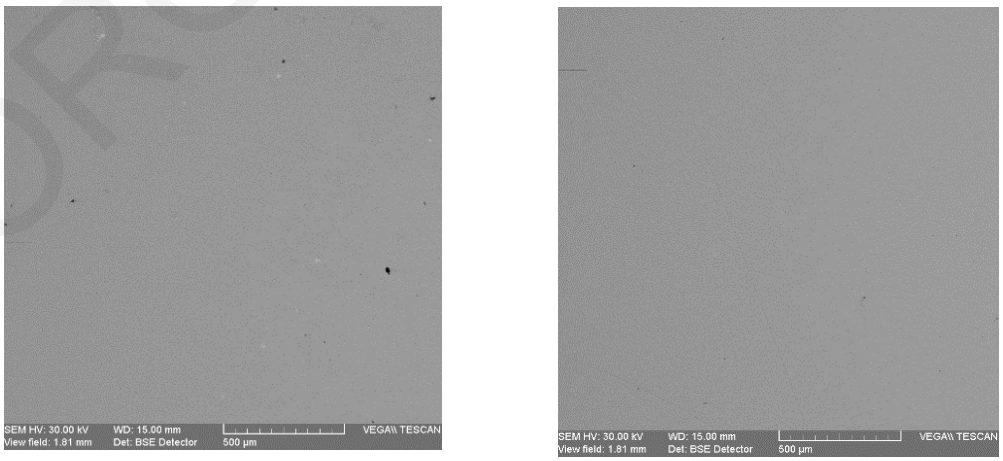

Figure 56: SEM images of $Ti_{0.4}Hf_{0.6}NiSn$(left) and $(Ti_{0.4},Zr_{0.6})_{0.7}Hf_{0.3}NiSn$ samples .

5.3 TE Properties of Ti-Hf and Ti-Zr-Hf

5.3.1 TE properties of $Ti_{1-x}Hf_xNiSn$ series

The Seebeck coefficient and the electrical and thermal conductivity for the $Ti_{1-x}Hf_xNiSn$ samples as a function of temperature from 300 to 800K are shown in figure 57a-c. The Seebeck coefficient exhibited negative values, confirming the n-type character of the materials, and increased, with Hf concentration reaching the highest room temperature value of 176 μV/K for the sample $Ti_{0.4}Hf_{0.6}NiSn$. For Hf concentrations x>0.7, the Seebeck coefficient decreased indicating the increase of carriers concentration. This variation can be attributed to combined mechanisms of the band gap reduction with increasing Hf as well as the contribution of defects(i.e, Ni interstitials, (Ti,Hf)/Sn antisites)[117,118]. The electrical conductivity values are between 167-268 S/cm. The sample $Ti_{0.8}Hf_{0.2}NiSn$ exhibited the maximum value of 268 S/cm due to the existence of full Heusler phase. The power factor ($S^2\sigma$) can reach a peak of 22 μW/cmK^2 for the composition $Ti_{0.4}Zr_{0.6}NiSn$, 18 μW/cmK^2 for the $Ti_{0.8}Hf_{0.2}NiSn$ and 17 μW/cmK^2 for the $Ti_{0.4}Hf_{0.6}NiSn$.

The thermal conductivity is lower when Hf is incorporated in the lattice with the lowest value at x=0.6-0.7 (κ=2 W/m·K). Interestingly, these values are considerably lower than those of the Ti-Zr series [101]. In order to gain a better understanding of the substitution of Ti/Hf to the phonon scattering, the lattice thermal conductivity (κ_{lat}) was evaluated by subtracting the electronic part from the total thermal conductivity ($\kappa_{lat}= \kappa- \kappa_{ele}$). The Wiedeman-Frantz law was used to estimate the electronic thermal conductivity ($\kappa_{ele}=L\sigma T$ where L=Lorenz factor, σ=electrical conductivity and T=Temperature). The measurements of Seebeck coefficient assuming scattering from acoustic phonons were used in order to evaluate the Lorenz factor [8].Clearly, the Ti/Hf solid solutions display lower lattice thermal conductivity values than end members. The best figure of merit of the series is 0.46 at 762K for $Ti_{0.4}Hf_{0.6}NiSn$ member.

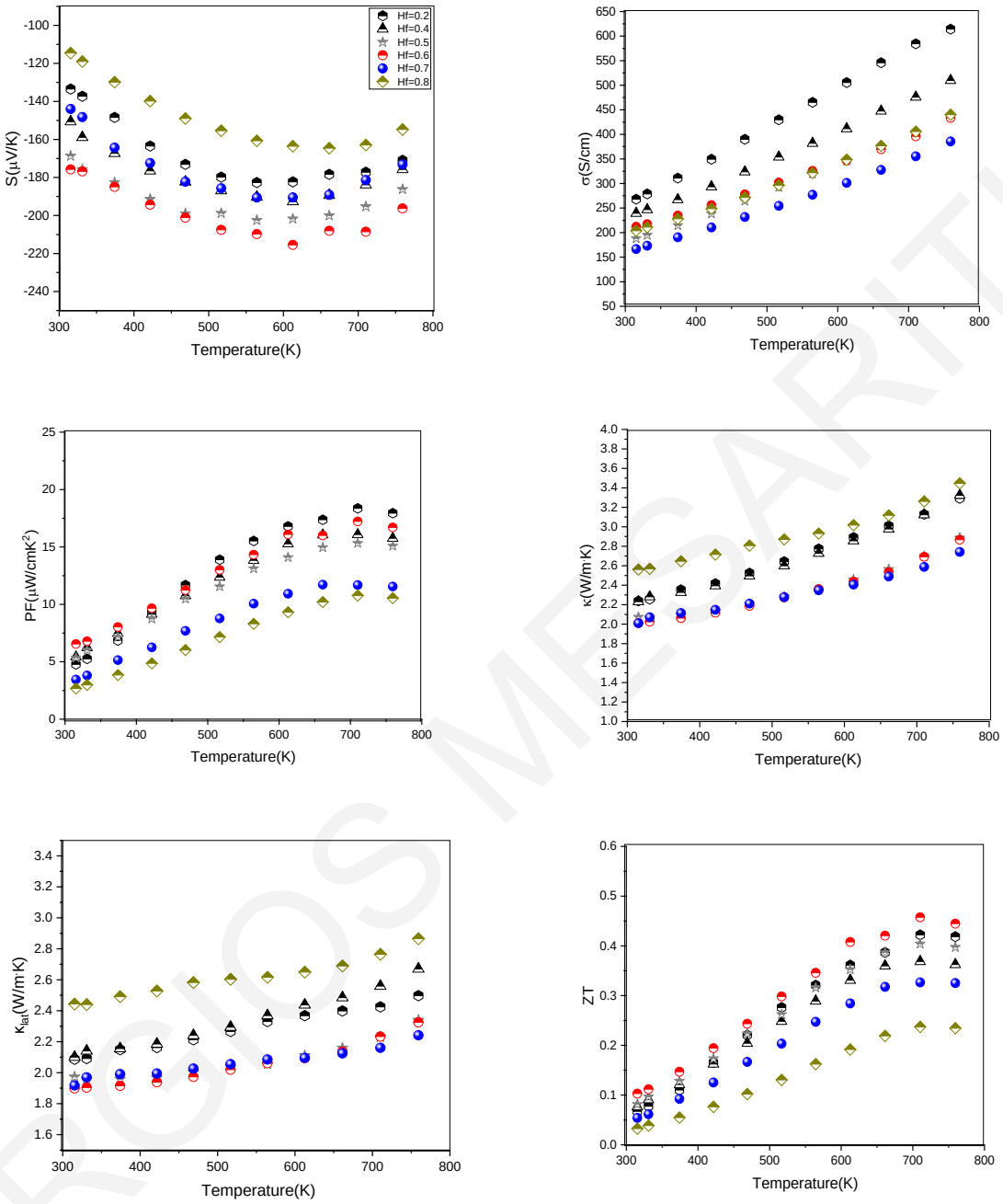

Figure 57: Thermoelectric Properties of $Ti_{1-x}Hf_xNiSn$ system.

5.3.2 TE properties of Sb-doped of $Ti_{0.6}Hf_{0.4}NiSn$

A common approach to enhance the thermoelectric performance of a material is optimization of carrier concentration through intentional doping. The member $Ti_{0.4}Hf_{0.6}NiSn$ was selected for further doping studies since it exhibited the lowest lattice thermal conductivity as well as high PF. Antimony was chosen as efficient dopant[77] and the Sb-doped $Ti_{0.4}Hf_{0.6}NiSn$ (Sb of 1 at%, 1.5 at% and 2 at%) series was synthesized. In figure 58, the experimental data of the Seebeck coefficient and the electrical and thermal conductivity are presented. The Seebeck coefficient is reduced (in absolute values) from -176μV/K for undoped sample to -94μV/K for the doped sample with 2 at% antimony due to the increase of carrier concentration, as expected. Moreover, the incorporation of Sb also results to the increase of electrical conductivity. The power factor was improved from 17 μW/cmK^2 for the undoped sample to 34 μW/cmK^2 for the doped sample (Sb=1.5% at) at 762 K. The total thermal conductivity increases with the incorporation of antimony into the lattice due to the enhancement of electrical conductivity. The figure of merit increases >20% with Sb incorporation reaching the value of 0.72 at 760K.

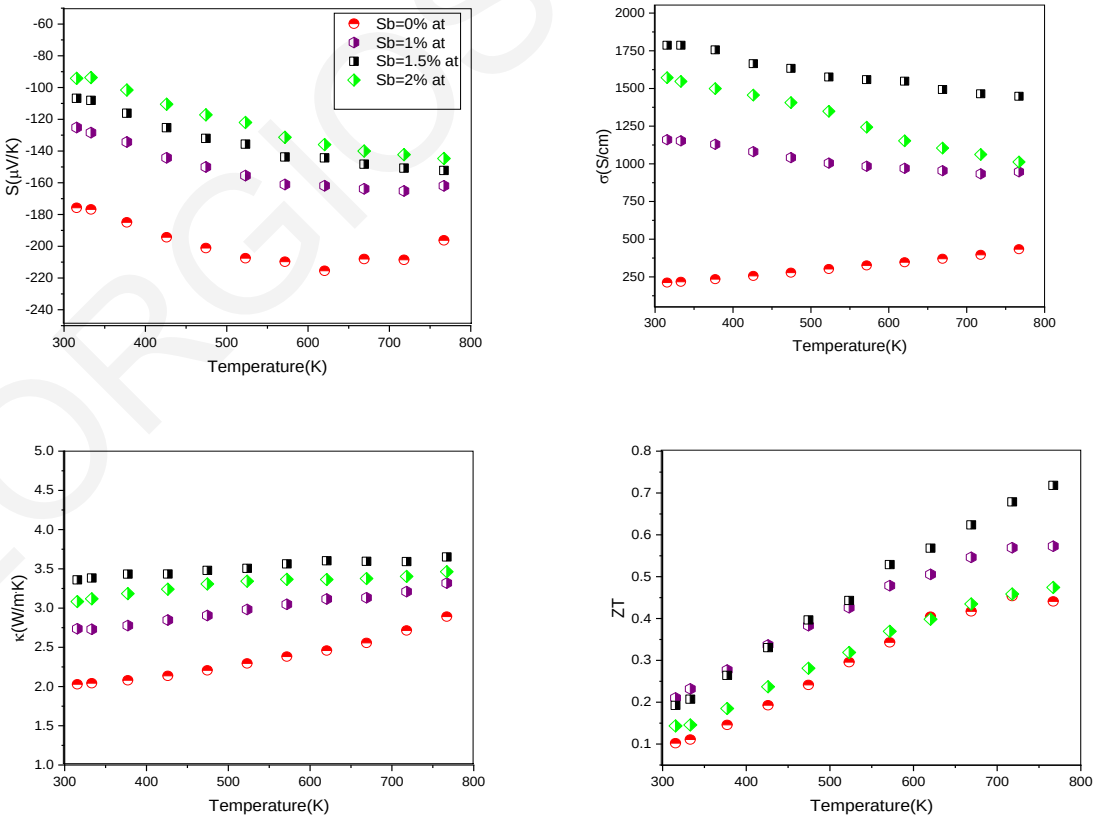

Figure 58: Thermoelectric Properties of Sb-doped $Ti_{0.4}Hf_{0.6}NiSn$ samples**.**

5.3.3 TE Properties of $(Ti_{0.4}Zr_{0.6})_{1-y}Hf_yNiSn$ series

The promising power factor of our previous work on $Ti_{0.4}Zr_{0.6}NiSn$ member [101] in combination with the lower lattice thermal conductivity caused by the Hf incorporation lead to the $(Ti_{0.4}Zr_{0.6})_{1-y}Hf_yNiSn$ series for further electrical and thermal investigations.

The Seebeck coefficient, electrical conductivity and the total thermal conductivity were measured in $(Ti_{0.4}Zr_{0.6})_{1-y}Hf_yNiSn$ samples from 300 to 800K as shown in figure 59a-e. In comparison to our best previous result $Ti_{0.4}Zr_{0.6}NiSn$, it is evident that the $Ti_{0.4}Zr_{0.6}NiSn$, interestingly, the Seebeck coefficient remains at about -200 μV/K; however, it is lower for the members y=0.1 and 0.25. Despite the fact that the Zr/Hf substitution is isoelectronic, the carrier concentration changes in the system in agreement to other works [] probably due to some defects that act as donors. The electrical conductivity, which is affected also by mobility, remained more or less the same and decreases when $y \geq 0.4$. The power factor ($S^2\sigma$) reach a peak of 26 $\mu W/cmK^2$ for the composition of y=0.3.These are very promising values, considering that these are undoped samples.The thermal conductivity for concentrations in the range $0 \leq y \leq 0.25$ is maximum with values (κ=2.63-2.21 W/m·K respectively). On the other hand, the materials with concentrations $0.3 \leq y \leq 0.5$ demonstrated the lowest values (κ=2.1-2.2W/mK respectively). This substitution has a significant impact to the figure of merit which reach a peak of 0.75 at 760K.

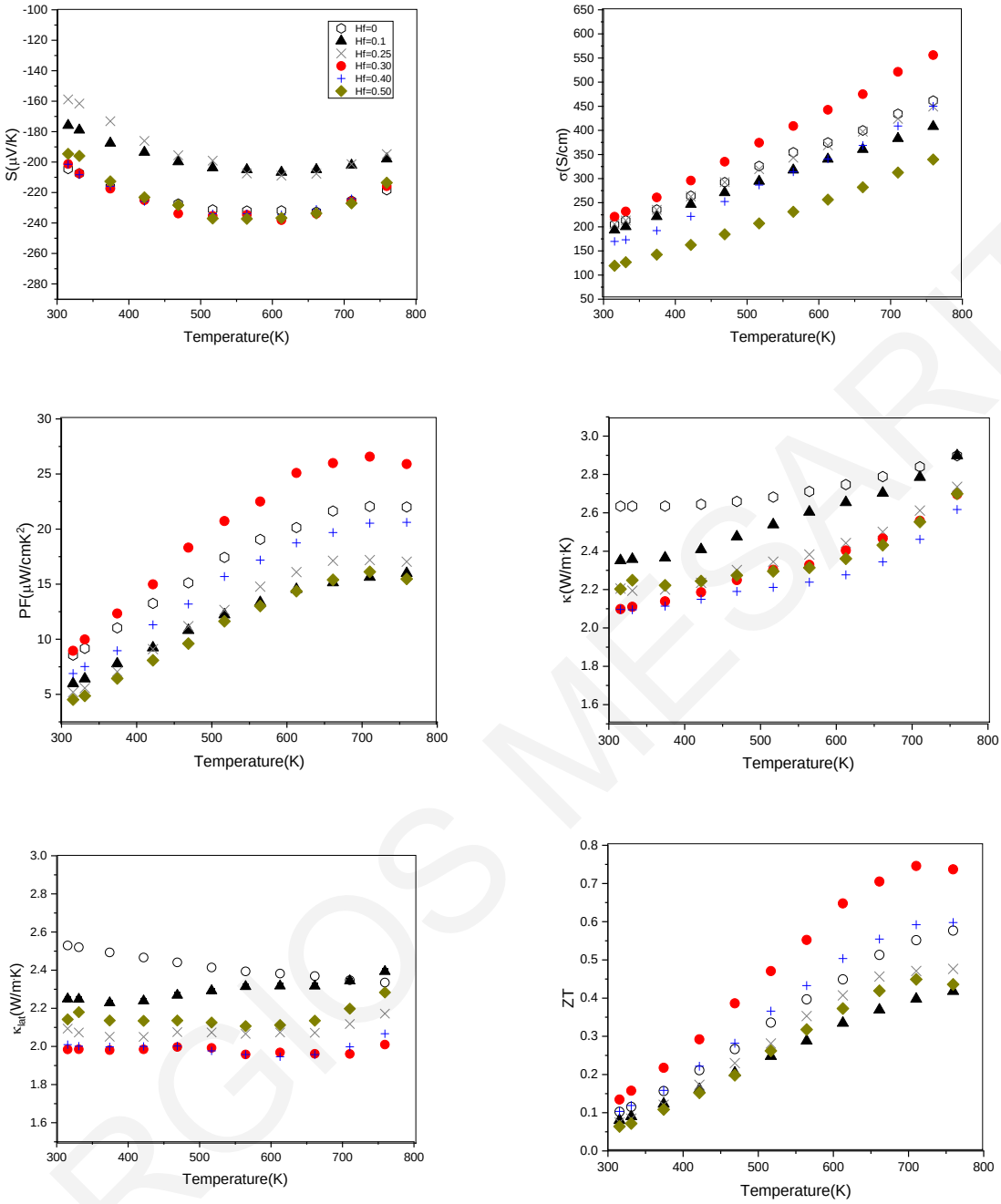

Figure 59: Thermoelectric Properties of $(Ti_{0.4}Zr_{0.6})_{1-y}Hf_yNiSn$ series**.**

5.3.4 TE Properties of Sb-doped $(Ti_{0.4}Zr_{0.6})_{0.7}Hf_{0.3}NiSn$

The member $(Ti_{0.4}Zr_{0.6})_{0.7}Hf_{0.3}NiSn$ was doped with antimony based on the stoichiometric composition by substituting Sn site with 1 at%, 1.5 at%, 2at% and 2.5 at%. In figure 60a-c the trends of the Seebeck coefficient, electrical and thermal conductivity are displayed. The Seebeck coefficient is reduced from -260μV/K for undoped sample to -87μV/K for the doped sample with y=0.025 antimony, as expected, due to the increase of carriers that Sb incorporation caused. Moreover, the electrical conductivity increases in agreement with Seebeck coefficient variation. The power factor increased from 26 $\mu W/cmK^2$ to 38 $\mu W/cmK^2$ for 2 at% Sb incorporation. The power factor for 2.5 at% Sb fell to 33$\mu W/cmK^2$, suggesting that Sb concentration of 2.5% exceeded the optimum carrier concentration for this series. The total thermal conductivity, see Figure 60c, increased with the incorporation of antimony into the lattice as expected due to enhancement of electrical conductivity. The figure of merit reached a maximum of 0.76 at 762K, which is the best reported in this work. Interestingly, the undoped and doped members have similar ZTs that actually originate from opposite ranges of power factors and thermal conductivity.

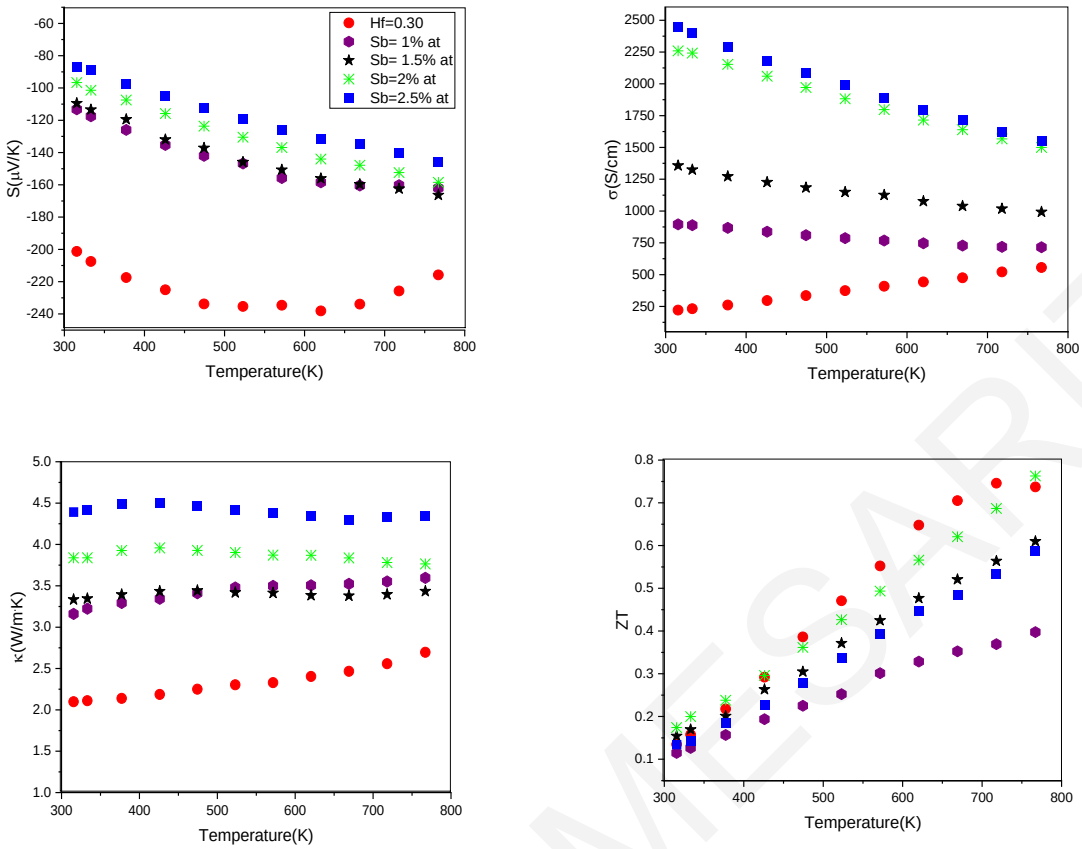

Figure 60: Thermoelectric Properties of Sb-doped $(Ti_{0.4}Zr_{0.6})_{0.7}Hf_{0.3}NiSn$.

5.4 Thermal conductivity of all series

Figure 61a shows the room temperature lattice thermal conductivity of the two series $Ti_{1-x}Hf_xNiSn$ and $(Ti_{0.4}Zr_{0.6})_{1-y}Hf_yNiSn$ as well as $Ti_{1-z}Zr_zNiSn$ from our previous work[101]. According to the literature, these values are lower compared to similar nominal compositions prepared by arc melting[108]. The minimum lattice thermal conductivity for arc melting was achieved for the composition $Ti_{0.6}Hf_{0.4}NiSn$ being κ_{lat}=3.15W/m·K [108], while the MA samples with the same stoichiometry exhibited κ_{lat}=2.1W/m·K. The low lattice thermal conductivities of our solid solutions, prepared via MA, can be attributed on nanostructuring as previously reported[101,119,120] .

All solid solutions exhibit lower lattice thermal conductivity compare to the end members, as expected, due to the scattering of the short wavelength phonons due to Ti/Zr/Hf mass fluctuation. Clearly, the incorporation of Zr in the lattice has a lower effect compared to Hf,which strongly affects and further reduces the lattice thermal conductivity. The introduced mass fluctuation can be evaluated based on the mass scattering parameter Γ_M based on the following equation[14] :

$$\Gamma_M = \frac{\sum_i^n c_i \left(\frac{\overline{M_i}}{\overline{\overline{M}}}\right)^2 {\Gamma^i}_M}{\left(\sum_i^n c_i\right)} \quad (27)$$

where the mass fluctuation parameter Γ^i_M is given:

$${\Gamma^i}_M = \sum_k f_k \left(1 - \frac{{M^k}_i}{\overline{M_i}}\right)^2 (28)$$

M_i^k: mass of the k^{th} atom of the ith sublattice and f_i^k: the fractional occupation.

where the average mass of atoms on the ith sublattice:

$$\overline{M_i} = \sum_k {f^k}_i \, {M^k}_i \, (29)$$

and the average atomic mass of the compound:

$$\bar{\bar{M}} = \frac{\sum_i^n c_i \overline{M_i}}{\sum_i^n c_i} \quad (30)$$

Where c_i: relative degeneracies of the respective site.

Figure 61b shows the calculated Γ_M for the three different series $Ti_{1-x}Hf_xNiSn$, $(Ti_{0.4}Zr_{0.6})_{1-y}Hf_yNiSn$ as well as $Ti_{1-z}Zr_zNiSn$ (previous study [101]), Γ_M clearly confirms that the Hf incorporation in the lattice is the most effective with $Ti_{1-x}Hf_xNiSn$ having the highest values. Moreover, Γ_M of $(Ti_{0.4}Zr_{0.6})_{1-y}Hf_yNiSn$ series starts from 0.2, due to the existing fluctuation of $(Ti_{0.4}Zr_{0.6})$, and increases with Hf. Overall, Ti-Zr substitution has the lowest effect while Hf is preferred to maximize mass fluctuation.

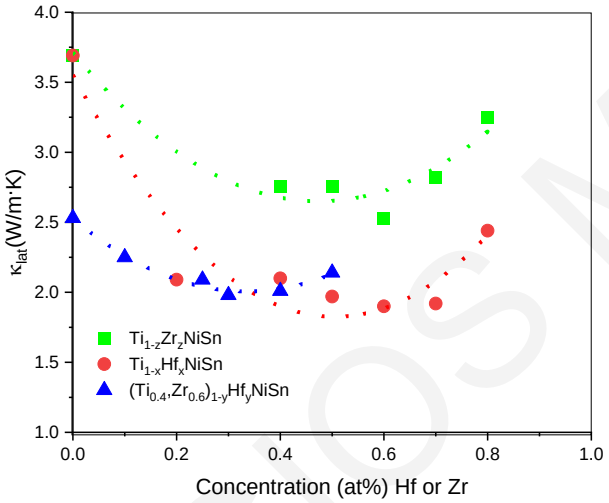

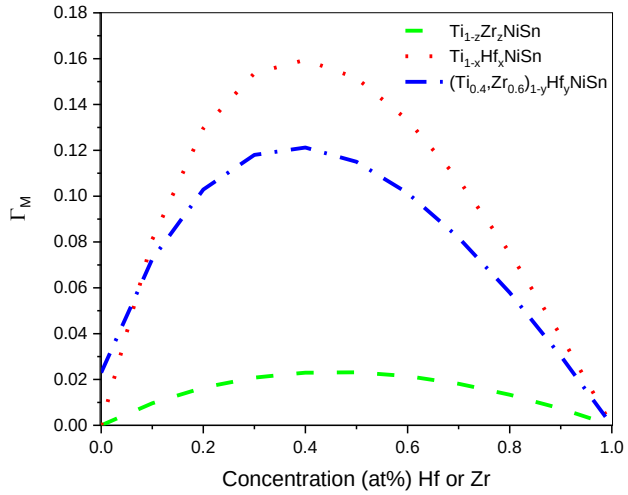

Figure 61: (a) Lattice thermal conductivity of all series and previous work. The doted lines are guide to the eye., (b)mass fluctuation parameter of all series.

5.5 Mechanical Properties

Mechanical characterization becomes more and more essential for promising TE materials as a practical requirement for mechanically stable and durable device. Among efficient TE materials, arc melted Half Heusler materials have been reported as mechanically stable for applications[121–124]. Here, HH prepared by MA are studied for the first time in terms of Vickers hardness. Figure 62 shows the hardness data of our series with Hf concentration, in comparison with the hardness of other members prepared by arc melting.

The hardness of $Ti_{1-x}Hf_xNiSn$ and $(Ti_{0.4}Zr_{0.6})_{1-y}Hf_yNiSn$ samples was in the range of 8 to 9.5 GPa. Overall, the values are in the same range regardless the Hf concentration or the synthesis method [69]. The latter is interesting, since these pellets are prepared by nanostructured powder and still in the same range with arc melted.

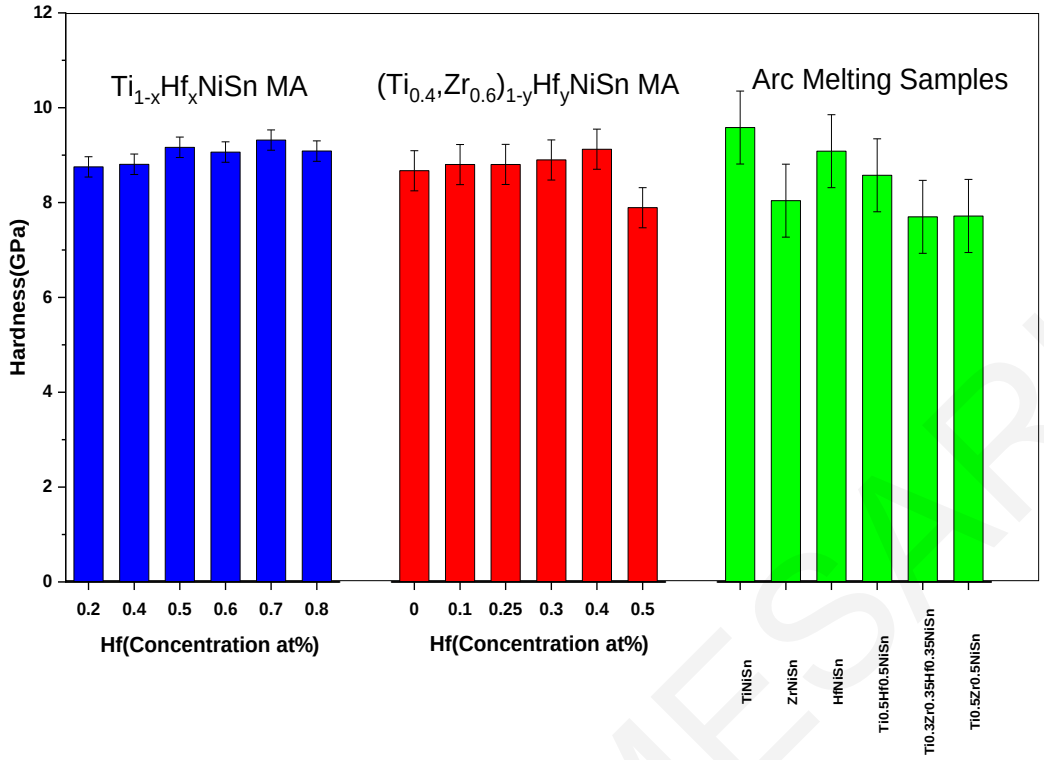

Figure 62: Hardness vs Hf concentration for the Ti1-xHfxNiSn samples and for the (Ti0.4,Zr0.6)1-yHfyNiSn samples and comparison from arc melted in literature.

5.6 Conclusions

In this work, the Hf incorporation in the $Ti_{1-x}Hf_xNiSn$ and $(Ti_{0.4}, Zr_{0.6})_{1-y}Hf_yNiSn$ solid solution series prepared by MA was successfully attempted. Both, undoped and doped samples exhibited single half Heusler phase. The lattice thermal conductivity was strongly affected by the mass fluctuation introduced by (Ti,Zr)/Hf substitution suggesting Hf incorporation as the most effective method. The thermoelectric properties of the solid solutions were optimized via Sb doping and the best ZTs were 0.72 and 0.76 at 773 K for the members $Ti_{0.4}Hf_{0.6}NiSn_{0.985}Sb_{0.015}$ and $(Ti_{0.4}Zr_{0.6})_{0.7}Hf_{0.3}NiSn_{0.98}Sb_{0.02}$ respectively. Moreover, the hardness measurements gave comparable values for the MA and the arc melted samples from the literature. Overall, the thermoelectric materials of these solid solutions prepared via MA are very promising and will be further investigated since such technique is advantageous due to simplicity and scalability for module development.

6.General Conclusions

Among the different types of half Heusler materials, the MNiSn and MCoSb (M=Ti, Zr, Hf) are strong candidates for thermoelectrics. The isoelectronic substitution at the M-site prompts extra mass and stress fluctuations and cause the scattering of short wavelength phonons, resulting in the reduction of the lattice thermal conductivity. The research community stated that a reduction of 17.9% and 36.3% is feasible in thermal conductivity via Zr and Hf doping, respectively, compared to undoped TiNiSn. Regarding the synthesis of HH materials, arc melting is the most commonly used method. Moreover, it is well known that additional treatments are necessary such as long annealing and ball milling to improve the thermoelectric properties via the reduction of the lattice thermal conductivity and the phonon scattering by alloying and nanostructuring. On the other hand, mechanical alloying seems to be good alternative technique to directly synthesize this type of material that exhibits low lattice thermal conductivity combining advantages such as scalability, simplicity, and the direct formation of nanostructuring. Until now, only few studies have been reported to synthesize half Heuslers directly from MA and hot press sintering.

Mechanical alloying method was selected to be applied on the synthesis of half Heusler materials aiming also the in-situ development of hierarchical structural features for the reduction of the thermal conductivity. More specifically, (Ti,Zr,Hf)NiSn solid solutions series were selected and emphasis was given on Hf incorporation that seemed more efficient. Disorder at atomic level via Ti/Zr/Hf substitution, nano-crystalline particles during mechanical alloying process, micro-grains during mechanical alloying and sintering process are the main mechanisms.

(Ti,Zr)NiSn system reached a figure of merit 0.71 for the $Ti_{0.4}Zr_{0.6}NiSn_{0.985}Sb_{0.015}$. The mass fluctuations of Ti/Zr substitution, nanostructuring, grain size reduction and strain caused by mechanical alloying contributed to the phonon scattering and resulted the improvement of the thermoelectric properties. Sb- doping played also a crucial role to the improvement of the thermoelectric power factor, thus, to the overall figure of merit. However, the incorporation of Sb as dopant resulted in small amount of the Ni_3Sn_4 binary phase. Moreover, the addition of extra nickel in the best composition $Ti_{0.4}Zr_{0.6}Ni_{1+x}Sn$ was attempted in order to further increase the TE properties, however, Ni_3Sn_4 metallic phase was created resulting lower figure of merit. Annealing studies at the temperature of operation showed promising results about the stability of the materials prepared by MA. Furthermore, annealing at higher temperature showed that

short heating could be beneficial for the properties of the materials. However, longer heating time resulted in phase separation and should be avoided.

(Ti,Zr,Hf)NiSn was also studied with emphasis on the effect of Hf incorporation in the $Ti_{1-x}Hf_xNiSn$ and $(Ti_{0.4}Zr_{0.6})_{1-y}Hf_yNiSn$ solid solutions prepared by MA. The lattice thermal conductivity was strongly affected by the mass fluctuation introduced by (Ti,Zr)/Hf substitution suggesting Hf incorporation as the most effective method. The thermoelectric properties of the solid solutions were optimized via Sb doping and the best ZTs were 0.72 and 0.76 at 773 K for the members $Ti_{0.4}Hf_{0.6}NiSn_{0.985}Sb_{0.015}$ and $(Ti_{0.4}Zr_{0.6})_{0.7}Hf_{0.3}NiSn_{0.98}Sb_{0.02}$ respectively. Finally, hardness measurements gave comparable values for the MA and the arc melted samples from the literature.

Overall, half Heuslers are promising materials for future practical applications at medium to high temperatures. In our work, the n-type compositions $Ti_{0.4}Hf_{0.6}NiSn_{0.985}Sb_{0.015}$, $Ti_{0.4}Zr_{0.6}NiSn_{0.985}Sb_{0.015}$ and $(Ti_{0.4}Zr_{0.6})_{0.7}Hf_{0.3}NiSn_{0.98}Sb_{0.02}$ prepared by mechanical alloying achieved the highest ZTs. Clearly, mechanical alloying synthesis method can be applicable on future development of thermoelectric modules as scalable and simple method. Besides its potential for further improvement in terms of thermoelectric figure of merit, more work needs to be done on stability of the materials on operation temperatures as well as other aspects on the module development (such as metallization, contacts quality etc). Overall, this half Heusler system seems very promising and mature enough for further studies in the level of module development and generators design.

7.References

1. Zhang, X. & Zhao, L. D. Thermoelectric materials: Energy conversion between heat and electricity. *J. Mater.* **1**, 92–105 (2015).
2. Zoui, M. A., Bentouba, S., Stocholm, J. G. & Bourouis, M. A review on thermoelectric generators: Progress and applications. *Energies* **13**, (2020).
3. Jouhara, H. *et al.* Thermoelectric generator (TEG) technologies and applications. *Int. J. Thermofluids* **9**, (2021).
4. Sootsman, J. R., Chung, D. Y. & Kanatzidis, M. G. New and old concepts in thermoelectric materials. *Angewandte Chemie - International Edition* (2009) doi:10.1002/anie.200900598.
5. Minnich, A. J., Dresselhaus, M. S., Ren, Z. F. & Chen, G. Bulk nanostructured thermoelectric materials: Current research and future prospects. *Energy Environ. Sci.* **2**, 466–479 (2009).
6. Beretta, D. *et al.* Thermoelectrics: From history, a window to the future. *Mater. Sci. Eng. R Reports* **138**, 210–255 (2019).
7. T.M.Tritt. *Thermal Conductivity,Theory, Properties, and Applications*. (Springer, 2004). doi:https://doi.org/10.1007/b136496.
8. Kim, H. S., Gibbs, Z. M., Tang, Y., Wang, H. & Snyder, G. J. Characterization of Lorenz number with Seebeck coefficient measurement. *APL Mater.* **3**, 1–6 (2015).
9. Zhao, L. D., Dravid, V. P. & Kanatzidis, M. G. The panoscopic approach to high performance thermoelectrics. *Energy Environ. Sci.* **7**, 251–268 (2014).
10. Snyder, G. J. & Toberer, E. S. Complex TE meterials. *Nat. Mater.* **7**, 105–114 (2008).
11. Kanatzidis, M. G. Nanostructured thermoelectrics: The new paradigm? *Chem. Mater.* **22**, 648–659 (2010).
12. Vineis, C. J., Shakouri, A., Majumdar, A. & Kanatzidis, M. G. Nanostructured thermoelectrics: Big efficiency gains from small features. *Advanced Materials* (2010) doi:10.1002/adma.201000839.
13. Zhou, M., Chen, L., Zhang, W. & Feng, C. Disorder scattering effect on the high-temperature lattice thermal conductivity of TiCoSb-based half-Heusler compounds. *J. Appl. Phys.* **98**, (2005).
14. Yang, J., Meisner, G. P. & Chen, L. Strain field fluctuation effects on lattice thermal conductivity of ZrNiSn-based thermoelectric compounds. *Appl. Phys. Lett.* **85**, 1140–1142 (2004).
15. Geng, H. & Zhang, H. Effects of phase separation on the thermoelectric properties of (Ti, Zr, Hf)NiSn half-Heusler alloys. *J. Appl. Phys.* **116**, (2014).
16. Shen, Q. *et al.* Effects of partial substitution of Ni by Pd on the thermoelectric properties of ZrNiSn-based half-Heusler compounds. *Appl. Phys. Lett.* **79**, 4165–4167 (2001).
17. Zhang, Q. *et al.* Enhanced thermoelectric performance of Hafnium free n-type ZrNiSn half-Heusler alloys by isoelectronic Si substitution. *Mater. Today Phys.* **24**, 1–7 (2022).
18. Johnsen, S. *et al.* Nanostructures boost the thermoelectric performance of PbS. *J. Am. Chem. Soc.* **133**, 3460–3470 (2011).
19. Pichanusakorn, P. & Bandaru, P. Nanostructured thermoelectrics. *Mater. Sci. Eng. R Reports* **67**, 19–63 (2010).
20. Androulakis, J. *et al.* Spinodal decomposition and nucleation and growth as a means to

bulk nanostructured thermoelectrics: Enhanced performance in Pb1-xSn xTe-PbS. *J. Am. Chem. Soc.* (2007) doi:10.1021/ja071875h.
21. Zhao, L. D. *et al.* High performance thermoelectrics from earth-abundant materials: Enhanced figure of merit in PbS by second phase nanostructures. *J. Am. Chem. Soc.* (2011) doi:10.1021/ja208658w.
22. Kim, W. *et al.* Thermal conductivity reduction and thermoelectric figure of merit increase by embedding nanoparticles in crystalline semiconductors. *Phys. Rev. Lett.* **96**, 1–4 (2006).
23. Girard, S. N. *et al.* In situ nanostructure generation and evolution within a bulk thermoelectric material to reduce lattice thermal conductivity. *Nano Lett.* (2010) doi:10.1021/nl100743q.
24. Papageorgiou, C., Giapintzakis, J. & Kyratsi, T. Low-temperature synthesis and thermoelectric properties of n-type PbTe. *J. Electron. Mater.* **42**, 1911–1917 (2013).
25. Sharief, P. *et al.* Reduction of thermal conductivity through complex microstructure by dispersion of carbon nanofiber in p-type Bi0.5Sb1.5Te3 alloys. *Arch. Metall. Mater.* **66**, 803–808 (2021).
26. Palaporn, D. *et al.* Synthesis of Silicon and Higher Manganese Silicide Bulk Nano-composites and Their Thermoelectric Properties. *J. Electron. Mater.* **49**, 2920–2927 (2020).
27. Alinejad, B. & Ikeda, T. Low temperature rapid fabrication of magnesium silicide for thermoelectric application. *Funct. Mater. Lett.* **12**, (2019).
28. Ioannou, M. *et al.* Fabrication of nanocrystalline Mg 2Si via ball milling process: Structural studies. *Powder Technol.* **217**, 523–532 (2012).
29. Ioannou, M., Delimitis, A., Symeou, E., Giapintzakis, J. & Kyratsi, T. Effect of silicon nitride/oxide on the structure and the thermal conductivity of CoSi nanocomposites. *J. Nanosci. Nanotechnol.* **17**, 1555–1563 (2017).
30. Rogl, G. *et al.* Attempts to further enhance ZT in skutterudites via nano-composites. *J. Alloys Compd.* **695**, 682–696 (2017).
31. Hsu, K. F. *et al.* Cubic AgPbmSbTe2+m: Bulk Thermoelectric Materials with High Figure of Merit. *Science (80-.).* (2004) doi:10.1126/science.1092963.
32. Androulakis, J. *et al.* Nanostructuring and high thermoelectric efficiency in p-type Ag(Pb 1-ySny)mSbTe2+m. *Adv. Mater.* **18**, 1170–1173 (2006).
33. Poudeu, P. F. P. *et al.* High thermoelectric figure of merit and nanostructuring in bulk p-type Na1-xPbmSbyTem+2. *Angew. Chemie - Int. Ed.* (2006) doi:10.1002/anie.200600865.
34. Biswas, K. *et al.* Strained endotaxial nanostructures with high thermoelectric figure of merit. *Nat. Chem.* (2011) doi:10.1038/nchem.955.
35. Ahn, K. *et al.* Exploring resonance levels and nanostructuring in the PbTe-CdTe system and enhancement of the thermoelectric figure of merit. *J. Am. Chem. Soc.* (2010) doi:10.1021/ja910762q.
36. Biswas, K. *et al.* High thermoelectric figure of merit in nanostructured p-type PbTe-MTe (M = Ca, Ba). *Energy Environ. Sci.* (2011) doi:10.1039/c1ee02297k.
37. Zhao, L. D. *et al.* High thermoelectric performance via hierarchical compositionally alloyed nanostructures. *J. Am. Chem. Soc.* (2013) doi:10.1021/ja403134b.
38. Lee, Y. *et al.* High-performance tellurium-free thermoelectrics: All-scale hierarchical structuring of p-type PbSe-MSe systems (M = Ca, Sr, Ba). *J. Am. Chem. Soc.* (2013) doi:10.1021/ja400069s.
39. Zhao, L. D. *et al.* Raising the thermoelectric performance of p-type Pbs with endotaxial nanostructuring and valence-band offset engineering using CdS and ZnS. *J. Am. Chem. Soc.* (2012) doi:10.1021/ja306527n.

40. Girard, S. N. *et al.* High performance Na-doped PbTe-PbS thermoelectric materials: Electronic density of states modification and shape-controlled nanostructures. *J. Am. Chem. Soc.* (2011) doi:10.1021/ja206380h.
41. Androulakis, J. *et al.* Thermoelectrics from abundant chemical elements: High-performance nanostructured PbSe-PbS. *J. Am. Chem. Soc.* (2011) doi:10.1021/ja203022c.
42. Liu, W., Yan, X., Chen, G. & Ren, Z. Recent advances in thermoelectric nanocomposites. *Nano Energy* (2012) doi:10.1016/j.nanoen.2011.10.001.
43. Lan, Y., Minnich, A. J., Chen, G. & Ren, Z. Enhancement of thermoelectric figure-of-merit by a bulk nanostructuring approach. *Adv. Funct. Mater.* (2010) doi:10.1002/adfm.200901512.
44. Rowe, D. M., Shukla, V. S. & Savvides, N. Phonon scattering at grain boundaries in heavily doped fine-grained silicon-germanium alloys. *Nature* (1981) doi:10.1038/290765a0.
45. Hamilton, R. A. H. & Parrott, J. E. Calculation of room temperature lattice thermal conductivity of several materials using a continuum model. *Phys. Lett. A* (1969) doi:10.1016/0375-9601(69)90436-8.
46. Savvides, N. & Goldsmid, H. J. Boundary scattering of phonons in silicon crystals at room temperature. *Phys. Lett. A* (1972) doi:10.1016/0375-9601(72)90255-1.
47. Zhao, L. D. *et al.* All-scale hierarchical thermoelectrics: MgTe in PbTe facilitates valence band convergence and suppresses bipolar thermal transport for high performance. *Energy Environ. Sci.* (2013) doi:10.1039/c3ee42187b.
48. Biswas, K. *et al.* High-performance bulk thermoelectrics with all-scale hierarchical architectures. *Nature* **489**, 414–418 (2012).
49. Chauhan, N. S. *et al.* Compositional Tailoring for Realizing High Thermoelectric Performance in Hafnium-Free n-Type ZrNiSn Half-Heusler Alloys. *ACS Appl. Mater. Interfaces* **11**, 47830–47836 (2019).
50. Bhardwaj, A. *et al.* Panoscopically optimized thermoelectric performance of a half-Heusler/full-Heusler based in situ bulk composite Zr0.7Hf0.3Ni1+xSn: An energy and time efficient way. *Phys. Chem. Chem. Phys.* **17**, 30090–30101 (2015).
51. Tarkhanyan, R. H. & Niarchos, D. G. Effect of hierarchically distributed nano-to microscale skutterudite inclusions on the lattice thermal conductivity of TiNiSn-based half-Heusler alloys. *J. Alloys Compd.* **732**, 928–934 (2018).
52. Gao, Z. *et al.* Enhanced thermoelectric performance of higher manganese silicides by shock-induced high-density dislocations. *J. Mater. Chem. A* **7**, 3384–3390 (2019).
53. Yu, B. *et al.* Enhancement of thermoelectric properties by modulation-doping in silicon germanium alloy nanocomposites. *Nano Lett.* (2012) doi:10.1021/nl3003045.
54. Berry, T. *et al.* Enhancing Thermoelectric Performance of TiNiSn Half-Heusler Compounds via Modulation Doping. *Chem. Mater.* (2017) doi:10.1021/acs.chemmater.7b02685.
55. Fecher, G. H., Rausch, E., Balke, B., Weidenkaff, A. & Felser, C. Half-Heusler materials as model systems for phase-separated thermoelectrics. *Phys. Status Solidi Appl. Mater. Sci.* **213**, 716–731 (2016).
56. Chen, S. & Ren, Z. Recent progress of half-Heusler for moderate temperature thermoelectric applications. *Mater. Today* **16**, 387–395 (2013).
57. Joshi, G. *et al.* Enhancement in thermoelectric figure-of-merit of an N-type half-Heusler compound by the nanocomposite approach. *Adv. Energy Mater.* **1**, 643–647 (2011).
58. Poon, S. J. *et al.* Half-Heusler phases and nanocomposites as emerging high-ZT thermoelectric materials. *J. Mater. Res.* **26**, 2795–2802 (2011).

59. Joshi, G. *et al.* Enhancement of thermoelectric figure-of-merit at low temperatures by titanium substitution for hafnium in n-type half-Heuslers Hf0.75-xTixZr0.25NiSn0.99Sb0.01. *Nano Energy* **2**, 82–87 (2013).
60. Sakurada, S. & Shutoh, N. Effect of Ti substitution on the thermoelectric properties of (Zr,Hf)NiSn half-Heusler compounds. *Appl. Phys. Lett.* **86**, 1–3 (2005).
61. Culp, S. R., Poon, S. J., Hickman, N., Tritt, T. M. & Blumm, J. Effect of substitutions on the thermoelectric figure of merit of half-Heusler phases at 800°C. *Appl. Phys. Lett.* **88**, 1–3 (2006).
62. Xie, W., Jin, Q. & Tang, X. The preparation and thermoelectric properties of Ti0.5 Zr0.25 Hf0.25 Co1-x Nix Sb half-Heusler compounds. *J. Appl. Phys.* (2008) doi:10.1063/1.2885113.
63. Yu, C. *et al.* High-performance half-Heusler thermoelectric materials Hf1-x ZrxNiSn1-ySby prepared by levitation melting and spark plasma sintering. *Acta Mater.* (2009) doi:10.1016/j.actamat.2009.02.026.
64. Yu, C., Zhu, T., Xiao, K., Shen, J. & Zhao, X. Microstructure and thermoelectric properties of (Zr,Hf)NiSn-based half-Heusler alloys by melt spinning and spark plasma sintering. *Funct. Mater. Lett.* **3**, 227–231 (2010).
65. Kimura, Y., Ueno, H. & Mishima, Y. Thermoelectric properties of directionally solidified half-heusler (M 0.5a,M 0.5b)NiSn (M a, M b = Hf, Zr, Ti) alloys. *J. Electron. Mater.* **38**, 934–939 (2009).
66. Ouardi, S. *et al.* Transport and thermal properties of single- and polycrystalline NiZr 0.5Hf0.5Sn. *Appl. Phys. Lett.* **99**, 1–4 (2011).
67. Makongo, J. P. A. *et al.* Thermal and electronic charge transport in bulk nanostructured Zr 0.25Hf0.75NiSn composites with full-Heusler inclusions. *J. Solid State Chem.* **184**, 2948–2960 (2011).
68. Chen, L. D., Huang, X. Y., Zhou, M., Shi, X. & Zhang, W. B. The high temperature thermoelectric performances of Zr0.5Hf 0.5Ni0.8Pd0.2Sn0.99Sb 0.01 alloy with nanophase inclusions. *J. Appl. Phys.* **99**, (2006).
69. Suryanarayana, C. Mechanical alloying and milling. *Mech. Alloy. Milling* 1–472 (2004) doi:10.4150/kpmi.2006.13.5.371.
70. Tillard, M., Berche, A. & Jund, P. Synthesis of pure NiTiSn by mechanical alloying: An investigation of the optimal experimental conditions supported by first principles calculations. *Metals (Basel).* **8**, (2018).
71. Zou, M., Li, J. F., Du, B., Liu, D. & Kita, T. Fabrication and thermoelectric properties of fine-grained TiNiSn compounds. *J. Solid State Chem.* **182**, 3138–3142 (2009).
72. Aliev, F. G., Kozyrkov, V. V., Moshchalkov, V. V., Scolozdra, R. V. & Durczewski, K. Narrow band in the intermetallic compounds MNiSn (M=Ti, Zr, Hf). *Zeitschrift für Phys. B Condens. Matter* (1990) doi:10.1007/BF01323516.
73. Aliev, F. G. *et al.* Gap at the Fermi level in the intermetallic vacancy system RBiSn(R=Ti,Zr,Hf). *Zeitschrift für Phys. B Condens. Matter* (1989) doi:10.1007/BF01307996.
74. Hohl, H. *et al.* New class of materials with promising thermoelectric properties: M NiSn (M = Ti, Zr, Hf). *Mater. Res. Soc. Symp. - Proc.* **478**, 109–114 (1997).
75. Morelli, D. T. & Meisner, G. P. Transport properties of pure and doped mnisn (m=zr, hf). *Phys. Rev. B - Condens. Matter Mater. Phys.* (1999) doi:10.1103/PhysRevB.59.8615.
76. Appel, O. & Gelbstein, Y. A comparison between the effects of Sb and Bi doping on the thermoelectric properties of the Ti0.3Zr0.35Hf0.35NiSn half-heusler alloy. *J. Electron. Mater.* **43**, 1976–1982 (2014).
77. Bhattacharya, S. *et al.* Effect of Sb doping on the thermoelectric properties of Ti-based

half-Heusler compounds, TiNiSn1-xSbx. *Appl. Phys. Lett.* **77**, 2476–2478 (2000).
78. Hohl, H. *et al.* Efficient dopants for ZrNiSn-based thermoelectric materials. *J. Phys. Condens. Matter* **11**, 1697–1709 (1999).
79. Lee, M. S. & Mahanti, S. D. Validity of the rigid band approximation in the study of the thermopower of narrow band gap semiconductors. *Phys. Rev. B - Condens. Matter Mater. Phys.* **85**, 1–8 (2012).
80. Chaput, L., Tobola, J., Pécheur, P. & Scherrer, H. Electronic structure and thermopower of Ni (Ti0.5 Hf0.5) Sn and related half-Heusler phases. *Phys. Rev. B - Condens. Matter Mater. Phys.* (2006) doi:10.1103/PhysRevB.73.045121.
81. Chen, S. *et al.* Effect of Hf concentration on thermoelectric properties of nanostructured n-type half-heusler materials HfxZr1-xNiSn 0.99Sb0.01. *Adv. Energy Mater.* (2013) doi:10.1002/aenm.201300336.
82. Katsuyama, S., Matsushima, H. & Ito, M. Effect of substitution for Ni by Co and/or Cu on the thermoelectric properties of half-Heusler ZrNiSn. *J. Alloys Compd.* (2004) doi:10.1016/j.jallcom.2004.02.061.
83. Kim, S. W., Kimura, Y. & Mishima, Y. High temperature thermoelectric properties of TiNiSn-based half-Heusler compounds. *Intermetallics* (2007) doi:10.1016/j.intermet.2006.08.008.
84. Muta, H., Kanemitsu, T., Kurosaki, K. & Yamanaka, S. Substitution effect on thermoelectric properties of ZrNiSn based half-heusler compounds. *Mater. Trans.* (2006) doi:10.2320/matertrans.47.1453.
85. Bhattacharya, S. *et al.* Grain structure effects on the lattice thermal conductivity of Ti-based half-Heusler alloys. *Appl. Phys. Lett.* **81**, 43–45 (2002).
86. Katayama, T., Kim, S. W., Kimura, Y. & Mishima, Y. The effects of quaternary additions on thermoelectric properties of TiNiSn-based half-Heusler alloys. *J. Electron. Mater.* **32**, 1160–1165 (2003).
87. Makongo, J. P. A., Paudel, P., Misra, D. K. & Poudeu, P. F. P. Thermoelectric Properties of Zr0.5Hf0.5Ni0.8Pd0.2Sn0.99Sb0.01 half-Heusler Alloy with WO3 Inclusions. *MRS Online Proc. Libr.* **1267**, 710 (2010).
88. Zhang, X. *et al.* Significant enhancement in thermoelectric properties of half-Heusler compound TiNiSn by grain boundary engineering. *J. Alloys Compd.* **901**, 163686 (2022).
89. Poon, G. J. Chapter 2 Electronic and thermoelectric properties of Half-Heusler alloys. *Semicond. Semimetals* (2001) doi:10.1016/S0080-8784(01)80136-8.
90. Qiu, P., Yang, J., Huang, X., Chen, X. & Chen, L. Effect of antisite defects on band structure and thermoelectric performance of ZrNiSn half-Heusler alloys. *Appl. Phys. Lett.* (2010) doi:10.1063/1.3396981.
91. Gelbstein, Y. *et al.* Thermoelectric properties of spark plasma sintered composites based on TiNiSn half-Heusler alloys. *J. Mater. Res.* **26**, 1919–1924 (2011).
92. Appel, O. *et al.* Effects of microstructural evolution on the thermoelectric properties of spark-plasma-sintered Ti0.3Zr0.35Hf0.35NiSn half-heusler compound. *J. Electron. Mater.* **42**, 1340–1345 (2013).
93. Chen, L., Liu, Y., He, J., Tritt, T. M. & Poon, S. J. High thermoelectric figure of merit by resonant dopant in half-Heusler alloys. *AIP Adv.* (2017) doi:10.1063/1.4986760.
94. Rausch, E., Balke, B., Ouardi, S. & Felser, C. Long-Term Stability of (Ti/Zr/Hf)CoSb1-xSnx Thermoelectric p-Type Half-Heusler Compounds Upon Thermal Cycling. *Energy Technol.* (2015) doi:10.1002/ente.201500183.
95. Populoh, S. *et al.* High figure of merit in (Ti,Zr,Hf)NiSn half-Heusler alloys. *Scr. Mater.* **66**, 1073–1076 (2012).
96. Van Du, N. *et al.* Thermoelectric properties of n-type half-heusler compounds

synthesized by the induction melting method. *Trans. Electr. Electron. Mater.* (2015) doi:10.4313/TEEM.2015.16.6.342.
97. Downie, R. A., MacLaren, D. A., Smith, R. I. & Bos, J. W. G. Enhanced thermoelectric performance in tinisn-based half-Heuslers. *Chem. Commun.* (2013) doi:10.1039/c2cc37121a.
98. Lei, Y. *et al.* Microwave synthesis, microstructure, and thermoelectric properties of Zr substituted ZrxTi1−xNiSn half-Heusler bulks. *Mater. Lett.* (2017) doi:10.1016/j.matlet.2017.05.023.
99. Zhu, H. *et al.* Discovery of ZrCoBi based half Heuslers with high thermoelectric conversion efficiency. *Nat. Commun.* **9**, 1–9 (2018).
100. Fu, C. *et al.* Realizing high figure of merit in heavy-band p-type half-Heusler thermoelectric materials. *Nat. Commun.* **6**, 4–10 (2015).
101. Mesaritis, G. *et al.* n-type (Zr,Ti)NiSn half Heusler materials via mechanical alloying: Structure, Sb-doping and thermoelectric properties. *J. Phys. Chem. Solids* **167**, 110735 (2022).
102. Team, T. T. Hot Press system HP20 manual. https://www.thermaltechnology.com/products/hot-press/ (2017).
103. Team, R. Powder x-ray diffraction basic course. *Rigaku J.* **38**, (2022).
104. Henning, S. & Adhikari, R. *Scanning Electron Microscopy, ESEM, and X-ray Microanalysis*. *Microscopy Methods in Nanomaterials Characterization* (2017). doi:10.1016/B978-0-323-46141-2.00001-8.
105. Young, J. S. & Reddy, R. G. Processing and Thermoelectric Properties of TiNiSn Materials: A Review. *J. Mater. Eng. Perform.* **28**, 5917–5930 (2019).
106. Team, N. Laser Flash Analysis. https://www.netzsch.com/n47875 (2022).
107. Team, U. Ulvac-ZEM 3 manual. https://www.ulvac.com/ (2022).
108. Schwall, M. & Balke, B. On the phase separation in n-type thermoelectric half-Heusler materials. *Materials (Basel).* **11**, 1–17 (2018).
109. May, A. F. & Snyder, G. J. Materials, Preparation, and Characterization in Thermoelectrics. in *Thermoelectrics and its Energy Harvesting* (ed. Rowe, D. M.) 11-1-11–18 (CRC Press, 2017). doi:10.1201/b11891.
110. Tritt, T. M. *et al.* Effects of various grain structure and sizes on the thermal conductivity of Ti-based half-Heusler alloys. *Int. Conf. Thermoelectr. ICT, Proc.* 7–12 (2001) doi:10.1109/ict.2001.979603.
111. Bahrami, A. *et al.* Reduced Lattice Thermal Conductivity for Half-Heusler ZrNiSn through Cryogenic Mechanical Alloying. *ACS Appl. Mater. Interfaces* **13**, 38561–38568 (2021).
112. Jeffrey D. Germond , Paul J. Schilling, Nathan J. Takas, P. F. P. P. Thermoelectric Performance of Nanostructured ZrNiSn Compounds Synthesized by Mechanical Alloying. *Mater. Res. Soc. Symp. Proc. Vol. 1267 © 2010 Mater. Res. Soc.* **1242**, 1–6 (2010).
113. Gurunathan, R., Hanus, R. & Snyder, G. J. Alloy scattering of phonons. *Mater. Horizons* **7**, 1452–1456 (2020).
114. Bae, K. W. *et al.* Thermoelectric transport properties of n-Type Sb-doped (Hf, Zr, Ti)NiSn half-heusler alloys prepared by temperature-regulated melt spinning and spark plasma sintering. *Appl. Sci.* **10**, (2020).
115. Krez, J., Balke, B., Felser, C., Hermes, W. & Schwind, M. Long-term stability of phase-separated Half-Heusler compounds. 1–10.
116. Page, A., Van Der Ven, A., Poudeu, P. F. P. & Uher, C. Origins of phase separation in thermoelectric (Ti, Zr, Hf)NiSn half-Heusler alloys from first principles. *J. Mater. Chem. A* **4**, 13949–13956 (2016).

117. Bhattacharya, S. *et al.* Effect of boundary scattering on the thermal conductivity of TiNiSn-based half-Heusler alloys. *Phys. Rev. B - Condens. Matter Mater. Phys.* **77**, 1–8 (2008).
118. Gong, B. *et al.* Effects of Sc, Ti, Hf, V, Nb and Ta doping on the properties of ZrNiSn alloys. *J. Mater. Sci.* **54**, 10325–10334 (2019).
119. Ioannou, I. *et al.* High thermoelectric performance of p-type half-Heusler (Hf,Ti)Co(Sb,Sn) solid solutions fabricated by mechanical alloying. *J. Alloys Compd.* **858**, (2021).
120. Ioannou, I., Delimitis, A., Gelbstein, Y. & Kyratsi, T. Reduction of Hf via Hf/Zr Substitution in Mechanically Alloyed (Hf,Ti)CoSb Half-Heusler Solid Solutions. *Inorganics* **10**, (2022).
121. He, R. *et al.* Studies on mechanical properties of thermoelectric materials by nanoindentation. *Phys. Status Solidi Appl. Mater. Sci.* **212**, 2191–2195 (2015).
122. Rogl, G. *et al.* Mechanical properties of half-Heusler alloys. *Acta Mater.* **107**, 178–195 (2016).
123. Kawaharada, Y., Kurosaki, K., Muta, H., Uno, M. & Yamanaka, S. Thermophysical properties of NiZrSn1-xSbx half-Heusler compounds. *J. Alloys Compd.* **381**, 9–11 (2004).
124. Hermet, P. *et al.* Thermal expansion of Ni-Ti-Sn heusler and half-heusler materials from first-principles calculations and experiments. *J. Phys. Chem. C* **118**, 22405–22411 (2014).